12-2017

Damage, Tension/Compression Asymmetry and Inferred Crack Growth in Fatigue title of Aluminum Alloys

Colin Young
Purdue University

DAMAGE, TENSION/COMPRESSION ASYMMETRY AND INFERRED CRACK GROWTH IN FATIGUE OF ALUMINUM ALLOYS

by

Colin Young

A Dissertation

Submitted to the Faculty of Purdue University

In Partial Fulfillment of the Requirements for the degree of

Doctor of Philosophy

School of Mechanical Engineering

West Lafayette, Indiana

December 2017

THE PURDUE UNIVERSITY GRADUATE SCHOOL
STATEMENT OF COMMITTEE APPROVAL

Dr. Ganesh Subbarayan, Co-Chair
Department of Mechanical Engineering
Dr. Anil Bajaj, Co-Chair
Department of Mechanical Engineering
Dr. Stuart Bolton
Department of Mechanical Engineering
Dr. Patricia Davies
Department of Mechanical Engineering
Dr. Xiao Wang
Department of Statistics

Approved by:
Dr. Jay P. Gore
Head of the Graduate Program

This manuscript is dedicated to my wife Sharon, who has patiently supported me though the process of working toward this degree, and my children Jacob and Madison

ACKNOWLEDGMENTS

I would like to acknowledge the guidance, support and advice of my Major Professors Prof. Subbarayan and Prof. Bajaj. I would also like to thank my Graduate Committee members, Prof. Bolton, Prof. Davies, and Prof. Wang for the time and advice

TABLE OF CONTENTS

LIST OF TABLES

LIST OF FIGURES

ABSTRACT

Author: Young, Colin J. PhD
Institution: Purdue University
Degree Received: December 2017
Title: Damage, Tension/Compression Asymmetry and Inferred Crack Growth in Fatigue of Aluminum Alloys
Committee Chair: Ganesh Subbarayan, School of Mechanical Engineering

The idea of a quantity *D*, which tracks the damage state of a material from 0 (virgin) to 1 (failed) is a well-established concept. In fatigue tests, where a given load cycle is repeated until failure, it is common to define damage *D* per cycle as the fraction of total life consumed per cycle, or $1/N_f$. We begin by using Maximum Entropy method to develop a curve to model the life vs. load cycle relationship for a wrought aluminum alloy 2024-T351 in the low cycle fatigue range. The approach is novel in that the loading is described in terms in inelastic dissipation, rather than stress or strain. It is argued that inelastic dissipation provides a closer connection to the underlying physical damage processes. The resulting model is shown to fit the data set better than the Coffin-Manson equation, the Weibull distribution function, and other alternative functions. In wrought defect-free alloys such as 2024-T351, *low cycle fatigue life* is mainly determined by the number of cycles required for a persistent slip band (PSB) to form a propagating crack. Literature suggests that the process of crack formation in PSBs can be modeled as a Poisson process, for a constant amplitude test. This implies that once PSBs are established, typically in the first 10% of life, crack formation is equally likely on any cycle. Once the crack forms, the final 10% of life is occupied with crack growth. The premise that formation of cracks is a Poisson process provides a starting point for building a statistical model of the fatigue process. If the loading cycles are more severe, then the probability of crack initiation on each cycle is higher. It can be shown that the Coffin-Manson relationship and the Palmgren-Miner linear damage law can both be deduced from this model. Finally, it is shown that the scatter in lives at a given loading condition should follow the Erlang distribution, with a given positive shift. This is significant because the Erlang distribution has substantially the same left skewed shape as the Weibull and Log-normal distributions which are frequently used to model the scatter in fatigue lives.

The second half of this work is concerned with the fatigue process of cast aluminum alloy AS7GU, which has many intrinsic defects from which fatigue cracks tend to initiate. *Intermediate and high cycle* fatigue life is dominated by crack growth rather than time for crack initiation. A different measure of *D* is developed, based on a non-linear stress-strain relationship and applicable to the elastic-dominated high cycle fatigue regime. It is based on a general constitutive law of an elastic material, which is shown to reduce to a quadratic stress strain relationship for a uniaxial test. Like the measure proposed in previous literature, this measure associates damage with the difference between the apparent stiffness of the specimen in tension vs. compression. However, unlike previously described measures, it connects the tension/compression asymmetry to a general nonlinear material model. The measure is applied to a sequence of axial fatigue tests and a rapid increase in the measured damage late in the life of the specimens is observed. Finally, the damage curves from the axial tests previously mentioned are interpreted in terms of a small crack growth law. The sizes of the cracks growing within the specimens during the tests are inferred from the measured *D*. A finite element model of the specimen was created to determine the relation between damage (as indicated by increase in compliance) and the size of a modeled crack. The finite element-determined relation is used to infer the size of the cracks in the specimens previously mentioned. A small crack growth law is fit to these inferred crack growth traces with good success.

CHAPTER 1. INTRODUCTION

1.1 Motivation

Aluminum alloys are important engineering materials in weight-critical applications. Broadly, they are produced in both wrought forms (which are substantially worked during production) and cast forms (which are typically cast in their final shape). Wrought alloys include commonly known aerospace grades such as 2024, 6061, and 7075. Their finished shapes are limited to tubes and sheets and shapes that could be produced by machining massive sections, often at significant cost, or welding sheet and tube stock together, such as is done in the bicycle industry. Cast aluminum alloys such as 319, A356 and AS7GU can be cast into extremely complex shapes, such as automotive cylinder heads, or machine casings, that would not be feasible to manufacture with wrought alloys. By virtue of their cast structure, alloys such as AS7GU contain tiny voids and inclusions of various types that tend to act as fatigue crack initiation points if the component is subjected to severe loading [1]. This contrasts with the behavior of wrought alloys. If the specimen is finely finished and free from internal flaw, fatigue cracks tend to initiate at persistent slip bands [2]. In the case of low-cycle fatigue, where the metal is yielding during each cycle, the majority of the life is consumed with crack initiation. The fatigue behavior of both classes of material will be covered in this manuscript.

1.2 Stress-Based Fatigue Model

Fatigue failure can be defined as structural failure after repeated applications of a load [3]. One of the first documents concerning fatigue failure is found in a study of the failure of mine hoist chains by Albert (Germany) in 1828. Poncelet (France) discussed fatigue in his book on mechanics in 1839. One of the most famous early fatigue researchers was Wohler, who was motivated by failures of railway axles. Wohler developed design rules to improve the robustness of iron and steel components to fatigue failure. These early researchers were concerned with the fatigue life of materials when subjected to known alternating stresses. One of the most important expressions in the field of stress-based fatigue analysis is the Basquin equation, Equation (1.1) [4], which expresses the applied uniaxial stress range as a power function of the number of cycles that will, on average, cause failure at that stress level. In the simplest case, the mean

stress is zero. It is also common to define an endurance limit, which is the highest alternating stress level that a material can withstand an essentially infinite number of times (Equation (1.2)). From the point of view of fatigue testing, infinite life is often associated with ten million load cycles [3] [4]. Steels are known to have fairly well defined endurance limits. Other metals, such as aluminum, have less well defined ones [3].

$$\sigma_{alt} = A\,{N_f}^{b} \quad -0.12 < b < -.05 \tag{1.1}$$

$$\sigma_{alt} = \frac{\sigma_{max} - \sigma_{min}}{2}$$

$$\sigma_{alt} < S_e,\ N_f\ > 10^7 \tag{1.2}$$

The constant b, is typically in the range shown. If the alternating stress σ_{alt} is less than the endurance limit S_e, the life is interpreted as infinite or greater than ten million cycles. This relationship is typically plotted on log-log coordinates. An example is shown below (Figure 1.1)

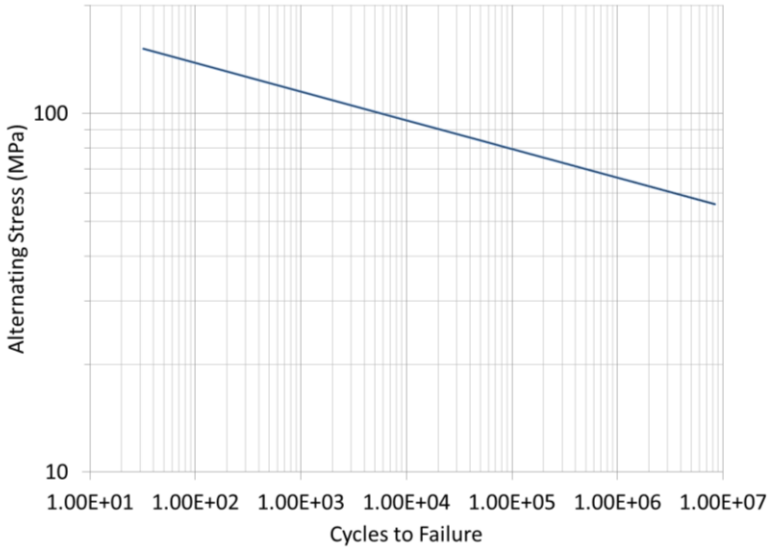

Figure 1.1: Basquin equation A = 200 MPa, b = -0.08.

The constants in this equation are determined by fitting the equation to sets of experimental data points. References exist to efficiently plan test sequences [5] and also to apply a statistical confidence bound to the resulting line [5] [6]. Fatigue data are known to have significant scatter

and multiple tests at similar load levels are needed to establish equations that can be used for design.

1.2.1 Effect of Mean Stresses

If a non-zero mean stress is present in a fatigue specimen, the life of the specimen is generally different than it would have been for zero mean stress [3] [4] [2] [7]. Figure 1.2 shows a few cycles of a load history. Table 1.1 lists the loading parameters of the history and gives definitions of some common variables used in fatigue analysis.

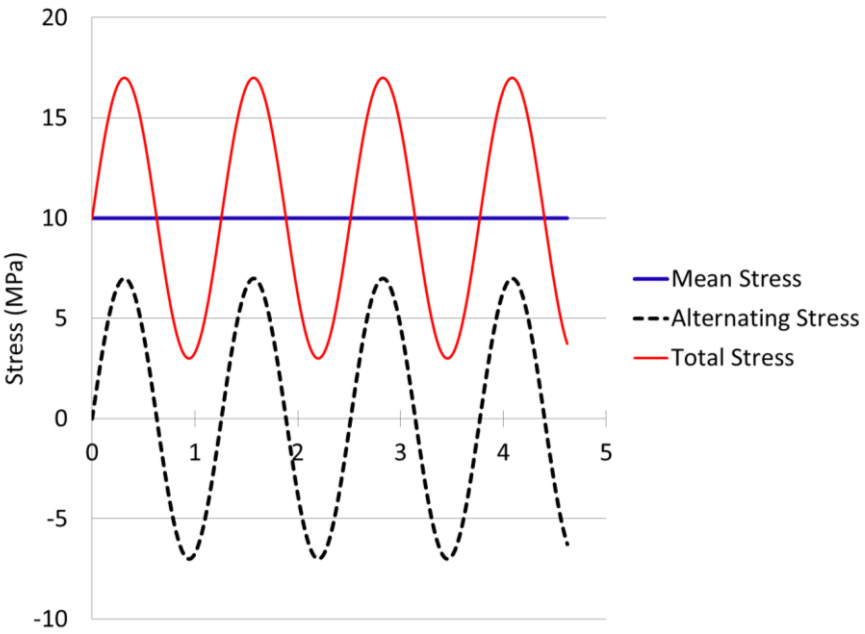

Figure 1.2: Example load history.

Table 1.1: Definitions of common fatigue load parameters.

Parameter	*Expression*	*Example Value (Fig 1.2)*
Alternating Stress	$\sigma_{alt} = \sigma_{max} - \sigma_{mean}$	65.0 MPa
Mean	σ_{mean}	80.0 MPa
Maximum	σ_{max}	145.0 MPa
Minimum	σ_{min}	15.0 MPa
Range	$\Delta\sigma = \sigma_{max} - \sigma_{min}$	130.0 MPa

The Goodman equation (Equation (1.3)) [3] was developed to model the combined effect of a mean and an alternating stress. The Goodman equation is only applicable to positive (tensile) mean stress states. The definitions of the variables in it are given in Table 1, and Table 2.

$$\frac{\sigma_{alt}}{S_e} + \frac{\sigma_{mean}}{S_{ult}} < 1 \quad Infinte\ life\ predicted \tag{1.3}$$

$$\frac{\sigma_{alt}}{S_e} + \frac{\sigma_{mean}}{S_{ult}} \geq 1 \quad Finite\ life\ predicted$$

Table 1.2: Example material properties.

Parameter	*Expression*	*Example Value (Fig 3)*
Endurance Limit	S_e	100 MPa
Ultimate Strength	S_{ult}	250 MPa

It is clear when Equation (1.3) is plotted (Figure 1.3), that $(\sigma_{mean}, \sigma_{alt})$ load histories that plot above the Goodman line are predicted to give finite life and those that plot below the line give infinite life. The left side of Equation (1.3) gives 0.97 for the example values given, which is barely an infinite life stress state.

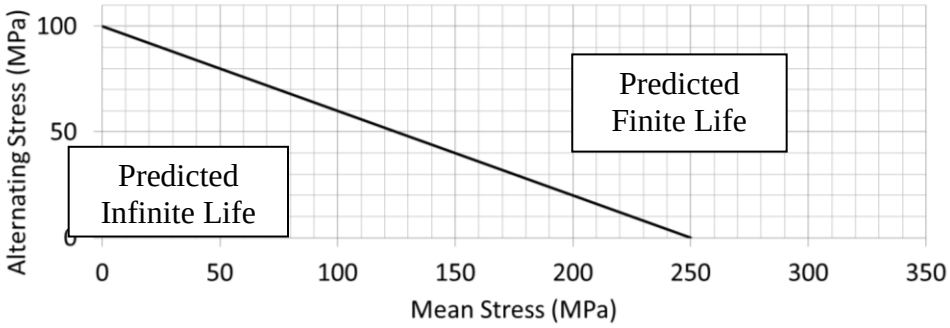

Figure 1.3: Goodman line.

It is known that the Goodman line is more successful for some materials than others and other researchers have made their own attempts to model the effect of mean stress. The Soderberg line uses the yield strength S_y in place of the ultimate strength [3]. The rationale for this modification is that even if the Goodman line is successful in predicting fatigue failure, designers usually do not want their component to yield. The Gerber line is parabolic, and is less conservative than the Goodman line [3]. The Morrow equation uses the true fracture strength (which is corrected for area reduction due to necking) rather than engineering ultimate strength, S_{ult}. For a comparative review of these and other mean stress effect models see [7]. The Haigh diagram extends into the compressive mean stress range and has a more complex shape based on additional test data points. It is also possible to construct a family of curves above the infinite life curves. Each of these curves is intended to represent a particular finite life. Curve families of this type are termed Master Fatigue Diagrams. An example is shown in Figure 1.4. The points at which the curve cross the vertical axis (zero mean stress) would be expected to follow the Basquin model for life vs. alternating stress. Note that this diagram shows an effect that is frequently observed, which is that moderate mean compressive stresses are protective in fatigue.

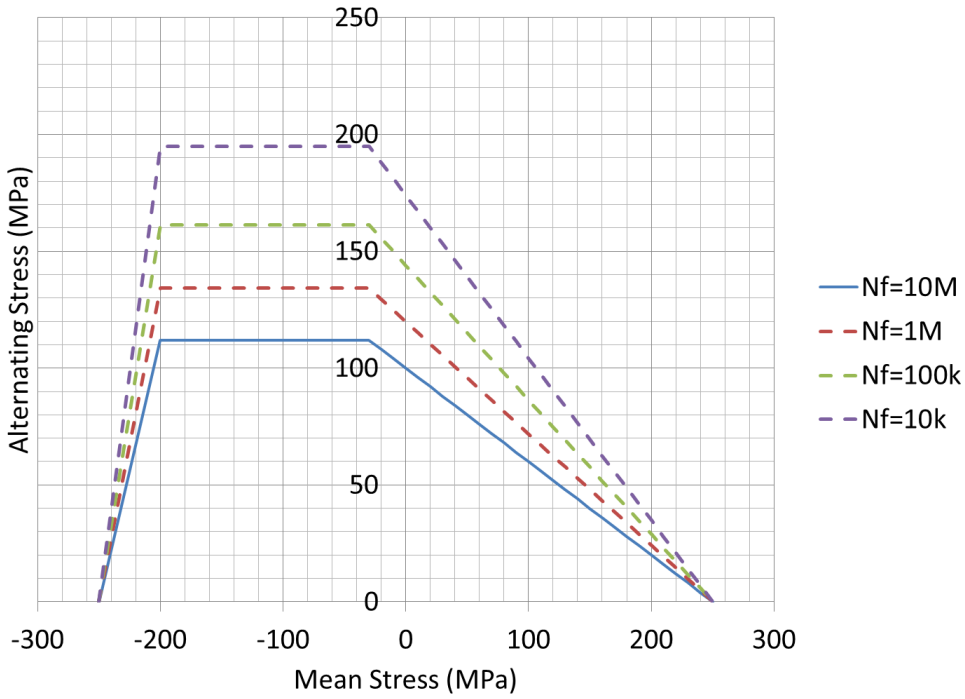

Figure 1.4: Master fatigue diagram example.

1.2.2 Changing Load Histories

All of the results given so far model fatigue as a consequence of a known applied stress (possibly with a known mean stress) applied a known number of times. Of course, actual usage histories include different numbers of cycles of differing stress levels. An example of a sequence of load blocks is given in Table 1.3. For this example, mean stress is zero.

Table 1.3: Example of changing load history.

Load Block	Cycles N	Stress σ_{alt}
	N_j	σ_{altj}
1	1,000	85
2	500,000	65
3	100,000	70

It is implied by the form of Equation (1.1), that the amount of fatigue damage caused is unaffected by the order of the load blocks [2]. Thus, changing load histories, weather they change stochastically or deterministically, can be sorted into blocks, which amounts to constructing a histogram of the load history. The Palmgren-Miner rule [3] (Equation (1.4)) allows a designer to add up the equivalent damage due to a sequence of load blocks such as given by Table 1.3.

$$Total\ Damage\ D = \sum \frac{N_j}{N_{fj}} \tag{1.4}$$

$$D \geq 1.0\ \ implies\ material\ failure$$

The form of Equation (1.4) implies that $D \geq 1.0$ corresponds to material failure. In order to determine the number of cycles a material can survive at a given stress level, an inverse form of Equation (1.1) is needed:

$$N_f = \left(\frac{\sigma_{alt}}{A}\right)^{\frac{1}{b}} \tag{1.5}$$

The procedure to apply Equation (1.4) is summarized in Table 1.4. The parameters used are A = 200 MPa, b = -0.08.

Table 1.4: Palmgren-Miner rule.

Load Block	Cycles N	Stress σ_{alt}	Cycles to failure N_f for stress σ_{alt}	Fraction of life consumed by Load Block j
	N_j	σ_{altj}	$N_{fj} = \left(\frac{\sigma_{altj}}{A}\right)^{\frac{1}{b}}$	$\frac{N_j}{N_{fj}} = N\left(\frac{A}{\sigma_{altj}}\right)^{\frac{1}{b}}$
1	1,000	85	44,200	0.023
2	500,000	65	1,260,000	0.40
3	100,000	70	500,000	0.20
			$Total\ Damage = \sum \frac{N_j}{N_{fj}}$	**0.61**

The total damage is $D = 0.61$ in this example, indicating that the material would be expected to survive the load history. It is also noted that block 2 consumed 0.4 of the specimen life and was the most damaging of the three load blocks. It is known that this rule is not always successful in predicting failure (or survival) [3] [2] [8], due to load history effects that will be discussed in a later section. Other damage summation rules have been proposed that are intended to account for load sequence effects [2] [8]. A survey of various approaches to damage summation can be found in [8].

1.3 Strain-based Fatigue Modeling

Prior to the 1950s fatigue researchers had been concerned with predicting fatigue life based on the stress history applied to the specimen, possibly including the effect of mean stress. The researchers Coffin and Manson independently discovered that the plastic strain history was more effective at predicting fatigue life in cases where plastic strain could be effectively measured.

1.3.1 Modeling Plastic Deformation

Tension loads below a certain threshold produce purely elastic responses while a sufficiently large stress causes permanent plastic yielding. Some very brittle metals fracture with almost no discernable yielding. An example of the stress strain curve showing yielding is given in Figure

1.5 below. The Ramberg-Osgood relation (Equation (1.6)) [3] is widely used to model plastic yielding of metals. The curve plotted in Figure 1.5 is an example of this function. The perfectly plastic curve is also plotted. The entire curve in this case is termed 'elastic-perfectly plastic' or 'EPP'. This is a simple plastic yielding model that is also frequently used for materials with well-defined yield points. Models that predict a rising stress after yielding (such as Equation (1.6)) are referred to as 'hardening' models even though the stress drops off from the linear response.

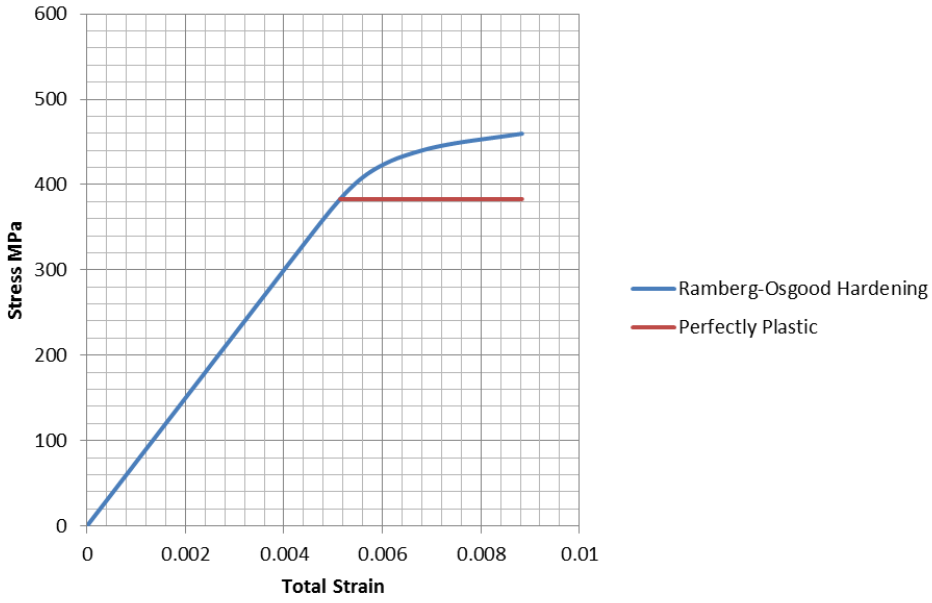

Figure 1.5: Stress-strain Curve (For a High-Strength Aluminum Alloy).

$$\epsilon_{total} = \epsilon_{elastic} + \epsilon_{plastic} \tag{1.6}$$

$$\epsilon_{total} = \frac{\sigma}{E} + \left(\frac{\sigma}{H}\right)^{\frac{1}{n}}$$

One important feature of Equation (1.6) is lack of a specific yield point. Finite yielding is predicted even for small stresses, although the actual magnitude predicted is very small. At 300 MPa, the plastic strain predicted by Equation (1.6) is on the order of 10^{-7}. This behavior is consistent with many real materials [3]. If a material is loaded until some plastic deformation is observed and then unloaded, in most cases the stress-strain response is linear back to the zero

stress line, but shifted over by the amount of plastic strain that occurred (Figure 1.6). The '0.2% Offset' method represents one common approach to define a clear yield point. The 0.2% Offset Yield Strength is the load sufficient to cause 0.2% permanent axial strain in the specimen after unloading. This value is commonly reported in material property data tables. When using this value for design it is important to note that yielding actually began at a lower value than the 0.2% offset value.

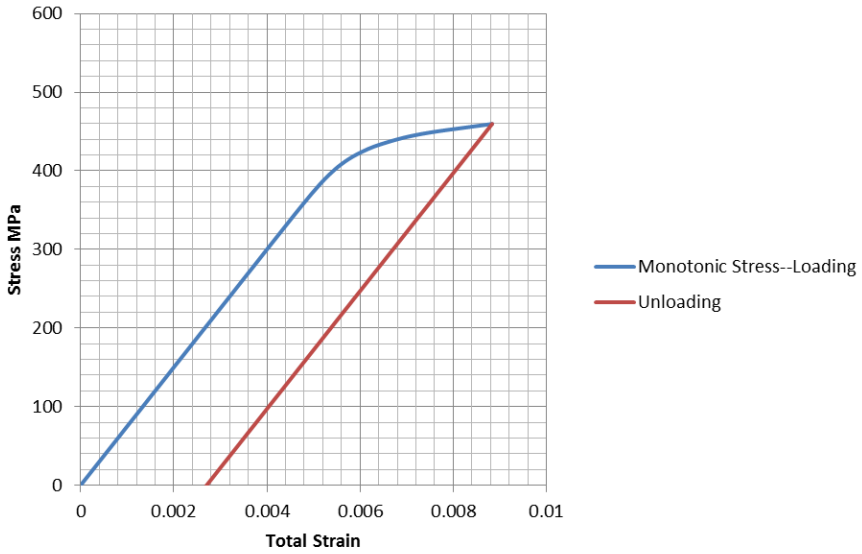

Figure 1.6: Linear unloading response.

1.3.2 Cyclic Plastic Deformation and Fatigue Damage

Plastic yielding causes fatigue damage if it is repeated. If fatigue failure occurs in about 20,000 cycles or fewer, it is considered to be in the area of *low cycle fatigue.* Alternatively, failures occurring in the range of 20,000 cycles or more are classified as *high cycle fatigue* [3]. Low cycle fatigue typically corresponds to loads that cause obvious yielding that can be measured with an extensometer. In high cycle fatigue the lower loads often appear to be purely elastic, but yielding in local, possibly microscopic, areas is known to be occurring [3] [2]. If a specimen is subjected to fully-revered tensile stress cycles sufficient to cause yielding, the stress-strain response of the material usually stabilizes to a loop as shown in Figure 1.7. The width of the loop (measured where the horizontal axis crosses the loop) corresponds to the amount of plastic

strain and the area of the loop corresponds to the plastic work (also called inelastic dissipation) per load cycle [2].

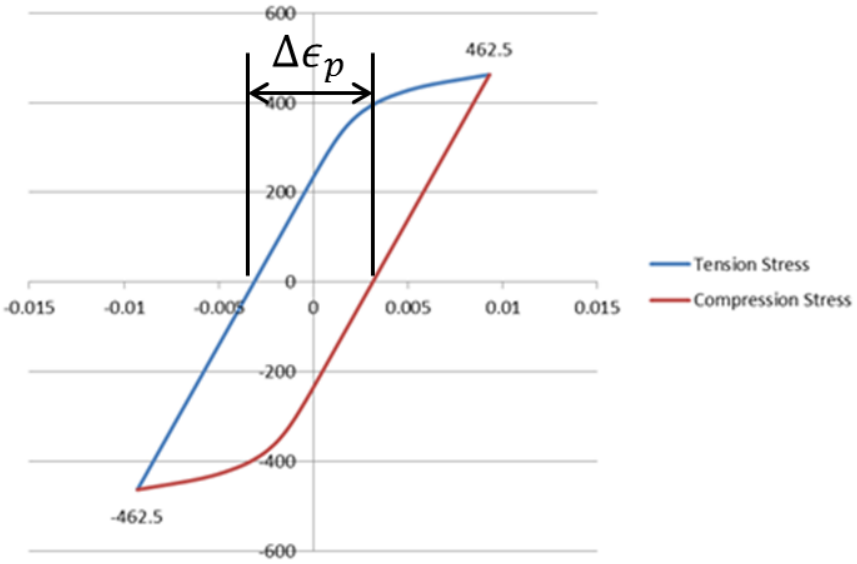

Figure 1.7: Stress-strain loop.

Figure 1.8 shows a wider loop corresponding to larger load and strain amplitude. Figure 1.9 shows the loop collapsed to a line for a purely elastic load cycle.

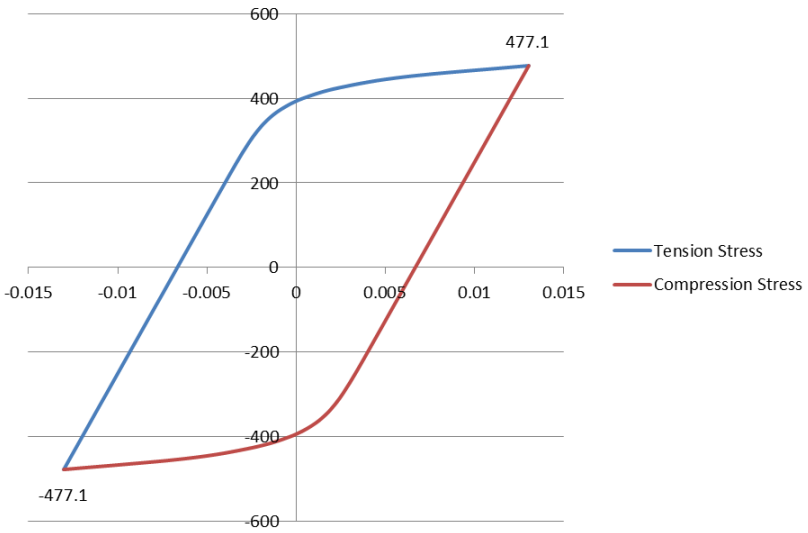

Figure 1.8: Loop for larger plastic strain.

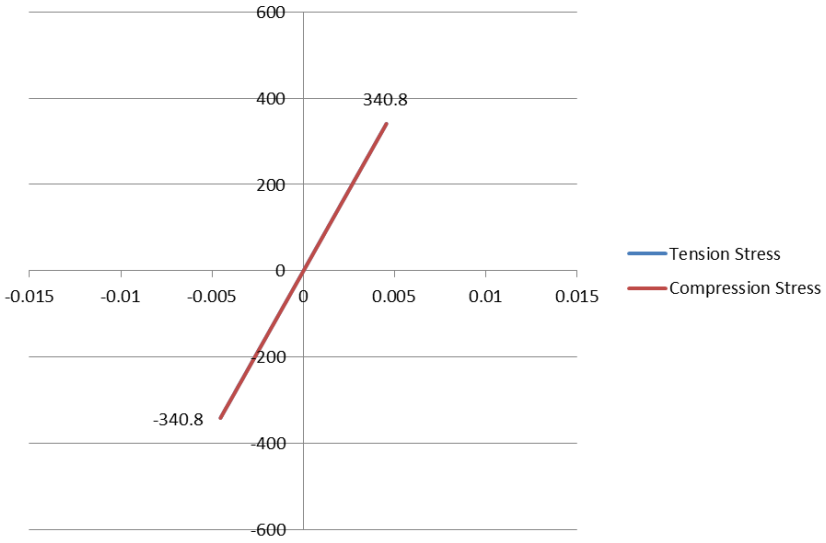

Figure 1.9: Stress-strain loop for elastic response.

The loop plots (Figures 1.7-1.9) are examples of the cyclic form of the Ramberg-Osgood relation Equation (1.7). Note that the loop curves are plotted using a coordinate system fixed at the end of the loop as shown in Figure 1.10. The blue line is referenced to the coordinate system shown. The red line is referenced to a reversed coordinate system at the upper right end of the loop. The constants in Equation (1.7) may differ from the values in Equation (1.6) for the same material [3]. The primes indicate that these are cyclic values, not monotonic values.

$$\Delta\epsilon = \frac{\Delta\sigma}{E} + 2\left(\frac{\Delta\sigma}{2H'}\right)^{\frac{1}{n'}} \tag{1.7}$$

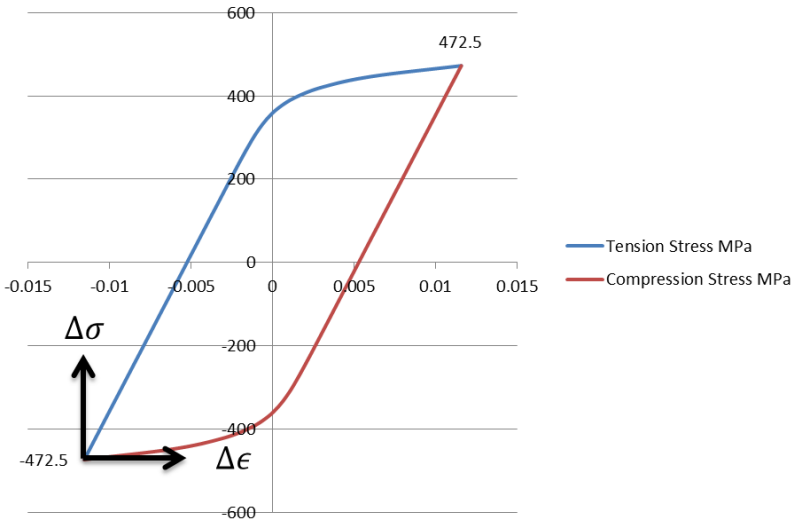

Figure 1.10: Coordinate system for cyclic Ramberg-Osgood relation.

1.3.3 Fatigue Damage due to Cyclic Plastic Strain

The researchers Coffin and Manson discovered that the plastic strain range applied to a specimen was related to specimen's fatigue life by a negative power law of similar mathematical form to Equation (1.1) [3] [4]. This expression is called the Coffin-Manson relation and is given below in Equation (1.8). It has been found to be superior to Equation (1.1) for modeling fatigue life in the low cycle regime provided that plastic strain data is available.

$$\Delta\epsilon_p = B\,{N_f}^c \quad -0.9 < c < -0.6 \tag{1.8}$$

Developing strain-based fatigue life prediction methods was greatly helped by the availability of servo-hydraulic test machines. The machines could be operated in either load control (applied stress) or displacement control (applied strain) modes. In contrast to the rotating bending fatigue tests that simply applied a known load, the servo-hydraulic machines could apply a fixed (and adjustable) strain while recording the resulting load. Constructing loop plots such as Figure 1.8 requires equipment such as this.

The mean and alternating stress were defined previously. However, there is another common method to classify the load case. The *load ratio* is frequently used to characterize the range of the loading applied [3] [4]. It is defined in Equation (1.9).

$$R = \frac{\sigma_{min}}{\sigma_{max}} \tag{1.9}$$

It has a simple relationship to mean stress, Equation (1.10):

$$\sigma_{mean} = \frac{\sigma_{max} + \sigma_{min}}{2} = \sigma_{max}\frac{1+R}{2} \tag{1.10}$$

The load ratio is often quoted as shorthand for different common types of tests. Particular, commonly used values of 'R' are summarized in Table 1.5. Note that R =1 is a constant load and R > 1 is not meaningful.

Table 1.5: Examples of commonly used R values.

R Value	Example	Also Called:	Used for:
$R = -1$	-100 to 100 MPa	'Fully Reversed' or 'mean-zero'	Most common choice for stress and strain-based fatigue studies. Cantilevered loads on rotating components. Many vibrational loads due to inertia of loaded components.
$R = 0$	0 to 120 MPa	'Pulsating'	Loads of this type are also common in practice, such as when components come into and out of contact.
$R = 0.1\ to\ 0.2$	12 to 120 MPa	'Positive Minimum'	Fracture mechanics tension tests.

1.4 Fracture Mechanics

The field of fracture mechanics is primarily concerned with the mechanics of cracked elastic or elastic/plastic solid bodies and the conditions that cause the crack(s) to grow. The growth may suddenly cause the body to break completely or could be stable and gradual. In his pioneering work [9], Griffith studied the load needed to cause fracture in a cracked brittle (purely elastic)

body. Griffith showed that the theoretical energy required to create an increment of new (paired) cracked surfaces was equal to the decrease in elastic potential energy of the body due to the growth of the crack. The elastic potential energy stored in the body (under load) provided the energy required to extend the crack. Griffith's original result was obtained for glass, which has essentially no ductility. Thus, no energy was lost in inelastic dissipation.

1.4.1 Stress Intensity

In the 1950's Irwin extended Griffith's concept to ductile metals, provided the zone of plastic yielding was small [10]. He also introduced the material parameter *fracture toughness* and the loading parameter *stress intensity factor*. The stress intensity factor is defined in the neighborhood of the tip of a crack. It is determined by the dimensions of the crack, the geometry of the body and the boundary conditions applied to the body. Figure 1.11 shows an edge-cracked plate. The plate has some thickness t in the out of page dimension, which need not be small. The crack tip is the point where the two crack faces meet. The crack tip extends through the thickness of the plate and thus is a generally linear feature. The corresponding stress intensity is given by Equation (1.11) [10].

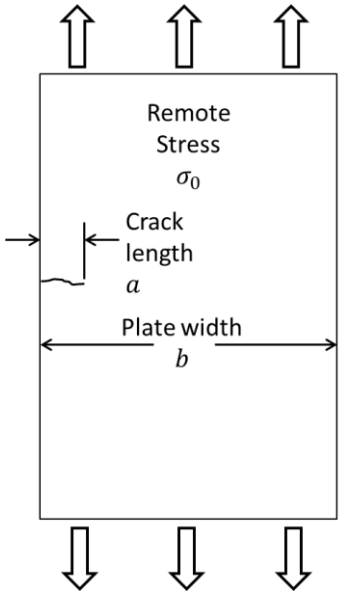

Figure 1.11: Edge cracked plate.

$$K = 1.12\sigma_0\sqrt{\pi a} \qquad (1.11)$$
$$a \leq 0.4\, b$$

According to the model, the crack will extend if the stress intensity exceeds the fracture toughness of the material. This result is mathematically equivalent to the energy criterion of Griffith for the case of brittle materials [10]. Although the stress intensity is derived from assumptions of elastic continuum mechanics, it has been shown to be sufficiently valid under the conditions of small-scale yielding, meaning that the region of plastic yielding at the crack tip is small relative to the dimensions of the crack and the body [10]. Griffith and Irwin's original results didn't predict crack growth resulting from repeated application of a load too small to extend the crack based on the fracture toughness criterion.

For a non-yielding linear elastic cracked body, the distribution of stresses has been derived for various geometries and loadings in addition to the edge-cracked plate in Figure 1.11. These analyses were performed under the assumption of a mathematically perfect crack (tip radius = 0) in an isotropic homogeneous material (Figure 1.12) [10]. They all share one important feature, which is all non-zero stress tensor components become singular at the theoretical crack tip. It is a fundamental result that the magnitude of the stresses is proportional to $1/\sqrt{r}$ as shown in Equation (1.12) [10].

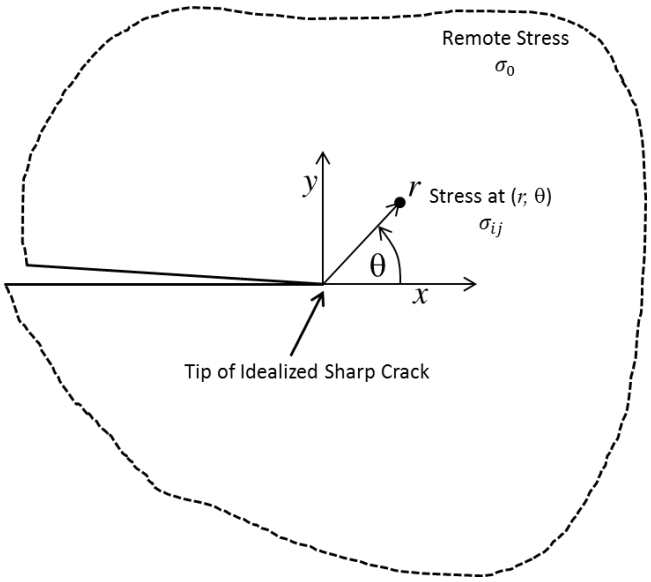

Figure 1.12: r theta system at crack tip.

$$\sigma_{ij} = \frac{\sigma_0 fcn(\theta, dimensions)}{\sqrt{2\pi r}} \tag{1.12}$$

1.4.2 Crack tip plastic zone

A real crack is not perfectly sharp and a real material will eventually fracture or yield as the remote load is gradually increased. As noted above, in ductile materials, a plastic zone is present in the neighborhood of the crack tip (Figure 1.13) [3] [4] [10]. The specific shape of the plastic zone depends on the geometry of the specimen, the properties of the material and the loading. In order for linear elastic fracture mechanics to be valid, the approximate diameter of the plastic zone must be ¼ or less than the length of the crack. This same ratio should apply to the width of the un-cracked ligament of the specimen [3]. Note that there are several ways a crack could potentially violate this criterion. A crack in a very ductile material under sufficient load could create a plastic zone large enough to violate the LEFM assumption. Alternatively, a very short crack could be small enough that even a plastic zone of moderate size is too large in comparison. Additionally, real metals have grains, precipitates, and other small-scale inhomogeneities. Cracks on the scale of these structures cannot be analyzed with LEFM as they violate the continuum assumption inherent in it.

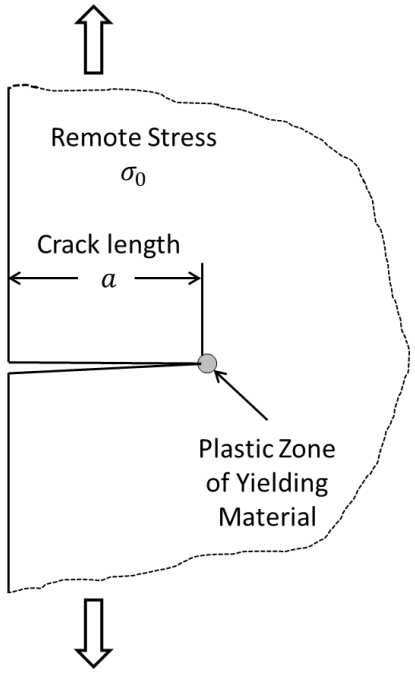

Figure 1.13: Yielded zone at crack tip.

1.4.3 Loading Modes

In fracture mechanics three modes of crack displacement are defined (Figure 1.13). These modes are explained in Table 1.6 [3] [10]. These modes apply to any crack, not just ones at the edges of plates.

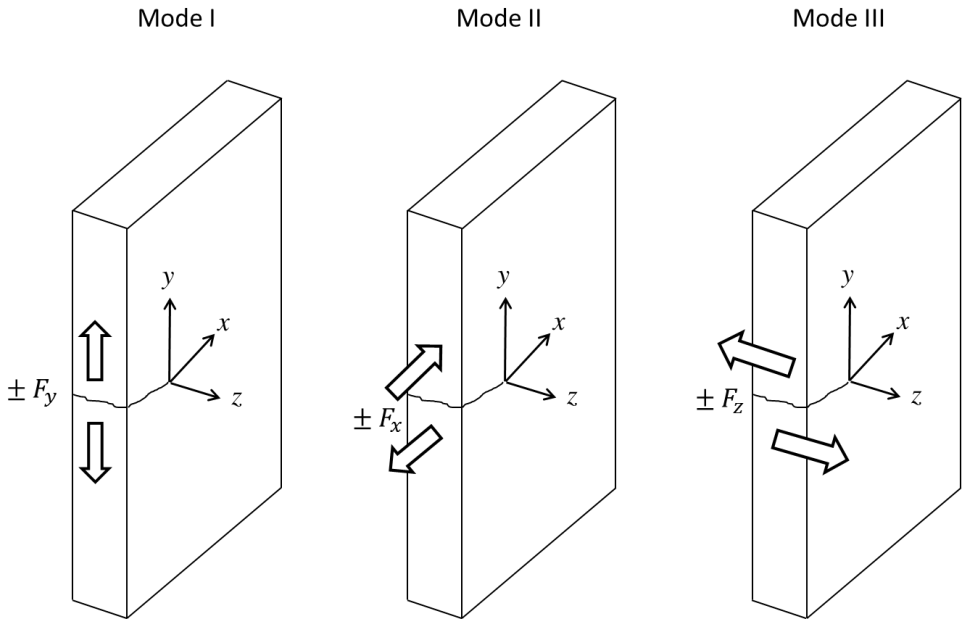

Figure 1.14: Modes of crack opening.

Table 1.6: Modes of crack opening.

Mode	Description—In terms of cracked plate	Examples
I	Perpendicular to crack faces	Cracked plate under tension such as a portion of a pressure vessel Cracked beam under tension or bending for cracks lying in transverse plane
II	Shear in plane of crack acting perpendicular to crack tip	Beam under bending with crack corresponding to neutral plane
III	Shear in plane of crack acting in line with crack tip (tearing)	Cracked beam under *torsion* for cracks lying in transverse plane

Note that a crack under a general load case may be subjected to mixed mode loading. An inclined crack in a bar under tension can be simultaneously under mode I, II, and III. The stress

intensity expressions are different depending on the mode although they all share the $1/\sqrt{r}$ singularity.

1.5 Crack Growth due to Repeated Loading

Irwin's contemporary Paris showed that repeated application of a sub-critical load could cause gradual growth of a crack in metal [3] [10]. He expressed the relationship as a power law, Equation (1.13). The quantity N is the number of completed load cycles. The differential expression is used to represent a small finite growth of the crack (possibly on the order of 10^{-10} meters/cycle or less) per each discrete load cycle.

$$\frac{da}{dN} = C\Delta k^m \tag{1.13}$$

The Paris law is one of many laws of similar form used to represent crack growth as a power function of applied stress intensity range [3] [10]. The exponent m is typically larger than 2, implying super-exponential crack growth rate for a constant amplitude cyclic load. Thus, laws of this type imply that incremental crack growth is governed by the same loading parameter as sudden fracture. The law is plotted in Figure 1.14. Note that three types of response are represented on the curve. For stress intensities below a lower threshold ΔK_{th}, cracks do not grow. This is analogous to the concept of endurance limit in stress-based fatigue. If the peak stress intensity exceeds the fracture toughness, then sudden crack extension, not incremental growth is expected. In between these two limits, power law growth according to Equation (1.13) is predicted.

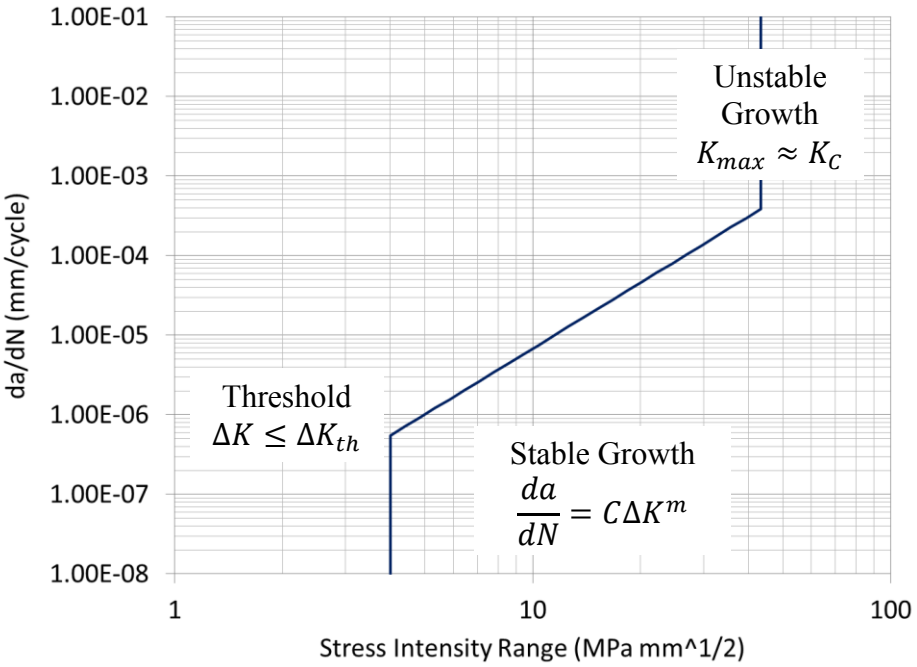

Figure 1.15: Paris law example.

1.5.1 Crack Closure

A crack in a ductile material such as a metal has a zone of plastic yielding near the tip of the crack. As the crack grows, the yielded material is stationary while the crack tip extends further [3] [10]. Thus, there is previously yielded material for some finite thickness on both faces of the crack. This is called the *plastic wake* of the crack (Figure 1.15) [3] [10]. This yielded material, since it separated from the material on the opposite side of the crack while in a tensile condition, will tend to extend from the crack faces and cause the crack faces to be compressively pressed together even when the remote stress is zero. Additionally, the previously fractured faces may not fit together perfectly and thus will be slightly forced apart after fracture on the previous load cycle [10]. As the remote stress is increased, the crack will remain closed until the closure force is overcome by the tensile stress field. The applied remote stress will have no effect on the crack tip until the closure stresses are zero and the crack opens all the way to the tip. This remote load level is termed the *crack opening load* K_{open} [10]. One important result of this phenomenon is that the applied stress amplitude at the crack tip is reduced by the crack opening load as given by Equation (1.14). If the applied stress amplitude does not exceed the crack opening load, then the load cycle would not be expected to cause crack growth. This connects the concept of crack

opening load to the fatigue threshold. Other potential causes of closure include corrosion, debris, and fluids [10].

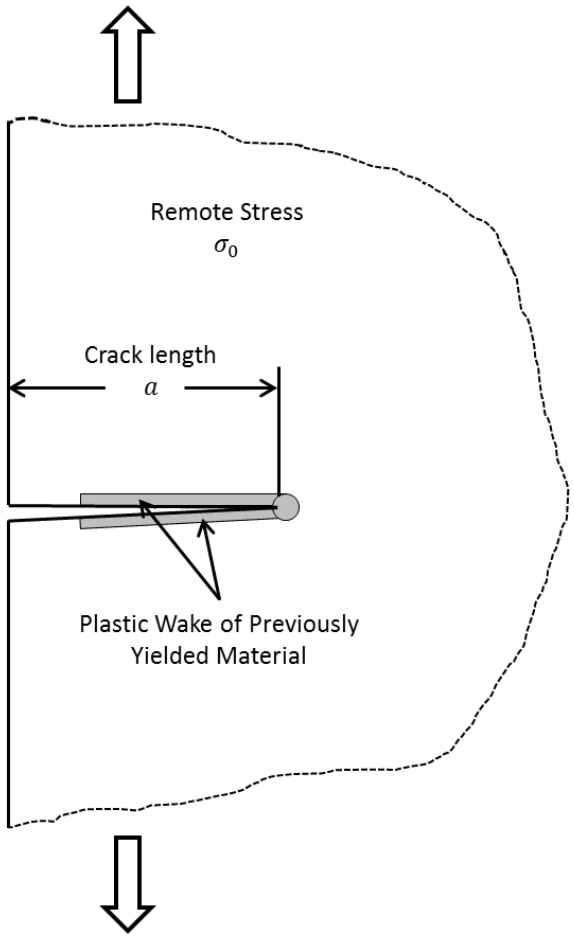

Figure 1.16: Plastic wake around crack.

$$\Delta K = K_{max} - K_{min} \quad K_{min} > K_{open} \tag{1.14}$$
$$\Delta K = K_{max} - K_{open} \quad K_{min} \leq K_{open}$$
$$\Delta K = 0 \quad K_{max} \leq K_{open}$$

1.5.2 Small Cracks

Cracks that are too small to be modeled with LEFM have distinct properties. Depending on the ductility of the material, 'small' cracks range in size from microns to single millimeter. They begin at the exterior surface, or at an internal stress riser [11]. Cracks large enough to be

modeled with LEFM propagate along planes perpendicular to local principal stress [3] [10] [11]. Small cracks that begin on an exterior surface initially propagate on planes of maximum sear stress at 45 degree angle to local principal stress directions (Stage I in Figure 1.16). Over the course of several microns of growth, they turn until they are aligned along planes normal to principal stress (Stage II) [11]. If relatively large defects are present in the material (such as the case with cast aluminum) then the cracks may grow directly from existing flaws (possibly at the surface).

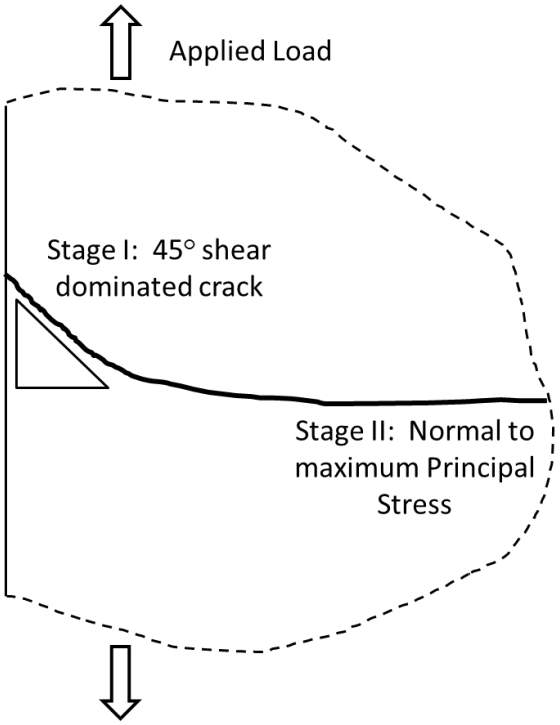

Figure 1.17: Stages of small crack growth.

The stress intensity K is not a valid mechanics parameter at the size scale of very small cracks under the condition of large scale yielding (> 50% Sy), which are surrounded by plastically deformed material. Thus, Nisitani and his colleagues model the growth of these small cracks with equations that depend explicitly on the crack length and the applied stress range. Generally, these equations are linear in crack length (and a power law in stress) and take the following form:

$$\frac{da}{dN} = C\Delta\sigma^m a \tag{1.15}$$

For a constant cyclic load magnitude, Equation (1.15) implies exponential growth of the crack length. Equation (1.15) would be used for cracks where the plastic zone is too large relative to the crack size to use a Paris-type law based on ΔK. Progressing crack growth may eventually enable the crack to satisfy LEFM conditions and a Paris-type law may be used from that point on. The authors note that the range of applicability of this equation is limited to small crack regime. Various authors (such as [10] and [12] [13] [14]) have noted that small (below ΔK applicability size) cracks typically grow much faster than would be predicted by naively applying a 'da/dN delta K' law to them. Under conditions of small scale yielding, authors such as [15] [16] argue that ΔK may still be used in equations such as Equation (1.13), although ΔK_{th} is not a material constant in this case and is observed to decrease with crack length.

1.6 Monitoring Damage in Specimen During a Fatigue Test

Several different viewpoints on modeling and monitoring cracks in specimens under fatigue tests are evident in the literature. The oldest approach is represented by the 'crack initiation' stress-based (and later strain-based) approaches to fatigue where generally the crack is not monitored. In these approaches, a specimen with no deliberately created notches or crack-like flaws is subjected to a cyclic load [3] [4]. Prior to the development of axial test machines, these specimens were typically subjected to rotating bending or sometimes in-pane bending loads. The test was most commonly run until the sample separated or successfully completed a large number of cycles (such as 10M). Some researchers stopped the test when a 'plainly visible' crack was discovered through periodic inspection. If an instrumented servo-hydraulic load frame was used for the test, then the researcher might stop the test when the stiffness of the specimen dropped below some threshold. This measurement indirectly depends on the presence of a crack or cracks but it was used as a stopping criterion, not a changing variable recorded during the test. In any case, there was usually no ongoing attempt to measure the progress of cracks during test that were too small to plainly see. The cycles-to-failure vs. applied load or applied strain data was sufficient to fit Basquin or Coffin-Manson models. Many of the researchers built relations that fit experimental data successfully (cycles to failure as functions of stress or strain), but did not provide a strong connection to physical principles beyond stress or plastic strain [3] [4]. It is important to note that even though the 'stress life' and 'strain life' approaches do not attempt to

model a crack (or cracks), it is recognized that some portion of the life of the component is consumed with the growth of crack(s) prior to final failure [2].

1.6.1 Measurement of Progressing Cracks

Fatigue researchers employing fracture mechanics take a very different approach. These investigators used specimens with a well-defined notch-like feature, intended to encourage the growth of a single crack, such as the compact tension specimen. They were usually concerned with the progress of the crack's length as a function of the number of fatigue cycles applied. In contrast to the global stress and strain used to predict life in the 'stress/strain life' models, fracture mechanics researchers used the macroscopic stress and strain to model the stress state in a small neighborhood close to the crack tip. Thus, this approach digs deeper than was the case before. Additionally, rather than simply predicting the overall life as a function of a stress amplitude, the actual growth of the crack is modeled. Equation (1.13) (and other 'da/dN delta k' laws) give a value of incremental crack growth as a function of current crack length and stress range (captured in stress intensity). During an experiment, the state of damage of a specimen is measurable and can be modeled throughout its life.

Consider a sequence of load cycle blocks, each with different loading parameters. In the fracture mechanics setting, the result of the evolving sequence of loads can be modeled and predicted, since the effect of a sequence of loads can be modeled directly without any assumption of how a sequence of changing loads would add together. It is straightforward to write a computer code to compute crack growth as a function of changing load cycles according to Equation (1.13). In the 'stress/strain life' approach, the damage due to a sequence of changing loads was typically assumed to be a linear combination of the damage of each load group separately (Equation (1.4)). The linear damage rule has been shown to have varying degrees of success [2] [8]. Some forms of 'da/dN delta K' laws satisfy the Palmgren/Miner rule while others do not. However, even in these cases, the fracture mechanics experiment allows the progressing damage to be directly measured and compared to predictions. Several approaches to measuring the length of the crack are used and are described in references such as [17], and include visually monitoring the crack with the aid of magnification, as well as inferring its length from some other measurable change in the specimen. In the case of fracture mechanics specimens, such as the compact tension

specimen or the center-cracked plate specimen, the crack may be viewed and measured from the side with the aid of magnification and a suitably fine scale, possibly marked on the specimen itself. The author of [4] mentions additional 'direct' measurement methods such as ultrasonics, die penetrant, magnetic techniques and x-ray. He also gives an example of a clear (polymer) specimen where the crack may be viewed through the end of the specimen. As an alternative to this 'direct' measurement, there are two 'remote' measurement methods recommended by [17]. The first is the electrical resistance method, where the increase in electrical resistance of the specimen is associated with the growth of a fatigue crack. The second is the compliance method, where the loss in stiffness of the specimen (in the crack opening direction) over the load history is used to infer the size of the crack. There are documented formulas to compute the size of cracks from the measured compliance of the specimens ([17] references Saxena and Hudak, 1978). Many authors (such as [18]) reference the compliance method and demonstrate its use (as well as applications of refinements of the method) to measure cracks in traditional fracture mechanics type specimens, with large notches, holes and existing cracks.

1.6.2 Measurement of Small Cracks

The third approach to monitoring the progress of fatigue cracks is exemplified by Nisitani and his coworkers [12] [13]. In this case, a traditional (not fracture mechanics) tension specimen is used but with one modification. Nisitani and others (such as [19]) make the point that what was regarded as crack initiation cycles in the 'stress/strain life' models actually includes a substantial amount of micro to small crack growth time. In [12], a single, microscopic, stress-concentrating flaw is deliberately created to encourage the formation of a crack at a predictable location. Micrographs of the specimen or a cast replication of its surface can then be used to monitor the progress of even very small cracks. This process requires the interruption of the fatigue test to inspect the crack. Crack length data is only obtained at these inspection intervals, not through the entire test.

1.7 Continuum Damage Mechanics

Stress and strain life approaches model the overall life of a specimen as a function of applied loading parameters without attempting to explain the progress of damage. Fracture mechanics

models the progress of a particular crack of known geometry. A third approach is taken in Continuum Damage Mechanics [20] [2], where many small cracks are hypothesized to exist in the damaged area of the material. The degree of material damage represented by these cracks is inferred from the macroscopic properties of the specimen. In [20], Lemaitre builds a general framework for modeling damage from various mechanical sources, including plastic deformation, creep, and low and high cycle fatigue. In his development, Lemaitre posits a distributed, isotropic, collection of small cracks that reduce the local effective load bearing cross section of the material from S to $\tilde{S}$.

$$\tilde{S} = S(1 - D) \tag{1.16}$$

Here damage is modeled by D, which ranges from 0 (virgin material) to 1 (failed, separated). One relation that follows is:

$$D = 1 - \frac{\tilde{E}}{E} \tag{1.17}$$

Where $\tilde{E}$ is the modulus of the damaged material and E is the modulus of the virgin material. Other relations for strength and strain are also developed. The cracks are assumed to be small enough and sufficiently evenly distributed such that the properties of the material vary smoothly in the neighborhood of the damaged area. Although this approach lacks direct evidence of the existence of a specific crack (or cracks) of known size and position, such as is available in fracture mechanics, it does seek to provide a mathematically detailed model, within the framework of continuum mechanics, that explains the experimentally observed behavior of damaged material. The author's work includes not only the mathematical model of damage, but also a set of experimental and data analysis techniques that attempt to reveal the state of damage of a given specimen at a particular point in an experiment. The author also shows that, in cases where the specimen is taken to the point of separation, a real crack was present and evidence of its growth is visible in striations and beach marks on the fracture surface.

1.8 Applications of Statistics

Statistics has been applied to aspects of modeling fracture and fatigue in many ways. Material strength test data (an input to some fatigue models) is subject to random variation. The cycles to failure corresponding to a given stress level is known to have significant statistical variation. Statistical procedures have been developed to establish lower bounds (at a specified confidence level) on the life values expected at a given load. Crack growth rates also exhibit random scatter. Although metal is frequently treated as a uniform isotropic continuum for many analytical purposes, it is known have a spatially random character when viewed at a fine enough scale [1] [3] [4] [2]. Within each metal grain, the orientation of the crystal planes is random. The shapes of the grain boundaries are random. If non-metallic inclusions are present in the metal, their size and locations are random. Some metals (such as cast aluminums) contain voids (internally) or pores (at the surface) [1]. The size and locations of these features are random. Non-metallic inclusions, oxide films, voids and pores are especially important to modeling fatigue because fatigue cracks frequently originate are such features [1]. Thus, statistical concepts can be applied at many levels of the problem—from the microstructure to the analysis of test data.

The most straightforward application of statistics to fracture mechanics and fatigue is the analysis of experimental results—the reduction of data. This is the same application statistics has found in any field of study that results in the collection of numerical (or even categorical) observables. Data that is used for design purposes must have some statistical confidence associated with it [5]. If the data is being compared to proposed theoretical model, a systematic procedure (probably taken from references) must be used to make the comparison. Many data collection systems have basic statistical and curve fitting capabilities built into them. A more subtle application of probability theory and statistics involves deducing the variability in a higher level quantity (such as cycles to failure) from a more fundamental one (such as the distribution of surface defects). The physical theory may be combined with probability theory to relate the two quantities. For example, if a variable y has a known functional (physical) dependence on another variable x, the probability distribution of y is determined by the distribution of x [21]. The distribution of y will, in general, be different from that of x but it is derivable from it. If the functional dependence is simple, then it may be possible to symbolically derive the relationship. If the function is more complex, a numerical solution would be required. Potentially several

observable effects could all depend, through different physical relationships, on the same underlying variable. Thus some observations subject to random variation may be shown to be the consequence of a single deeper random phenomenon.

When applying parametric statistical procedures, selecting the reference probability distribution is often the most important decision a researcher has to make. Frequently standard practice leans toward a particular parametric family of distributions [6, 35]. But even in this case, a researcher should understand the strengths and weaknesses of the commonly used distributions and be able to defend the one finally chosen. Sometimes a distribution may be defined as a transformation of a different distribution. For example if logarithms of the data are normally distributed, then the data is lognormally distributed [21]. The properties of the lognormal distribution are developed as modifications of the properties of the normal distribution. The useful property of the normal distribution, that sums of normally distributed random variables are also normally distributed becomes an analogous rule involving products in the lognormal case [21]. Another method to obtain a reference probability distribution for some purpose is the method of Maximum Entropy explained below. This method has the advantage of providing the 'most naive' (in the sense of information entropy) probability distribution subject to the mathematical constraints of the problem [22]. It is argued in the references cited below that the Maximum Entropy method involves the fewest unjustified assumptions. It is noteworthy that many of the commonly used distributions can be derived from the maximum entropy principle.

CHAPTER 2. MAXIMUM ENTROPY MODELS FOR FATIGUE OF METALS WITH APPLICATION TO LOW-CYCLE FATIGUE OF ALUMINUM 2024-T351

2.1 Introduction

In the present work, damage functions derived from maximum entropy formalism are demonstrated to fit the low-cycle fatigue data for aluminum 2024-T351 more accurately and consistently than several alternative damage models, including the Weibull distribution function and the Coffin-Manson relation. The formalism is founded on treating the failure process as a consequence of the increase in the entropy of the material due to plastic deformation. This argument leads to using inelastic dissipation as the independent variable for predicting low-cycle fatigue damage, rather than the more commonly used plastic strain. The entropy of the microstructural state of the material is modeled by statistical cumulative distribution functions, following examples in recent literature. We demonstrate the utility of a broader class of maximum entropy statistical distributions, including the truncated exponential and the truncated normal distribution. Not only are these functions demonstrated to have the necessary qualitative features to model damage, but they are also shown to capture the random nature of damage processes with greater fidelity.

2.2 Chapter 2 Nomenclature

Variable	Definition
$\Delta\epsilon_p$	Plastic strain range
$\epsilon_f{}'$	Fatigue ductility coefficient
c	Fatigue ductility exponent
N_f	Total cycles (loops) to failure

$D(t)$	Material damage parameter as a function of time or pseudo-time
$\Delta\sigma$	Stress range—total height of stress/strain loop
$\Delta\epsilon_{total}$	Total elastic plus plastic strain range
σ_f	True fracture stress
ϵ_f	True fracture strain
W_f	Total inelastic dissipation (per unit volume) to failure
A_f	Inelastic dissipation (per unit volume) per stress-strain loop-area of stabilized loop
$2N_f$	Total reversals to failure
H	The entropy of a probability distribution
p_i	Probability mass function value of the i^{th} random state
k_b	Boltzmann's constant
$I(p)$	The information associated with an event with probability p
$g_i(x)$	The i^{th} moment function
λ_i	The Lagrange multiplier corresponding to the i^{th} moment function
$f(x)$	The probability density function (PDF) of the random variable x
$F(x)$	The cumulative distribution function (CDF) of the random variable x
μ	Mean value of a random variable
σ	Standard deviation of a random variable
α	Weibull distribution shape parameter
β	Weibull distribution scale parameter
K	Ramberg-Osgood strength parameter
$\frac{1}{n}$	Ramberg-Osgood exponent

2.3 Background

The wrought aluminum alloy 2024-T351 is an important light structural metal commonly used in aerospace and other weight-critical applications [3]. A common approach to modeling the low cycle fatigue (LCF) life of this material, and many other metals, is the Coffin-Manson relationship [3] [23]:

$$\frac{\Delta\epsilon_p}{2} = \epsilon_f{}'\left(2N_f\right)^c \tag{2.1}$$

This equation is intended to cover the range of life from 1 to about 20,000 reversals, where macroscopic plastic strain is measurable. However, as has been pointed in references such as [23] , Equation (2.1) is less successful in fitting data in the very low reversal count range of 1 to about 200. The inadequacy of Equation (2.1) for modeling a representative LCF data set for 2024-T351 is demonstrated below and motivates an alternative LCF modeling approach.

In Figure 1, the results from a sequence of low cycle fatigue tests, and two monotonic tension tests on tension specimens of 2024-T351 aluminum is shown. The data is also fitted to a Coffin-Manson model in the figure.

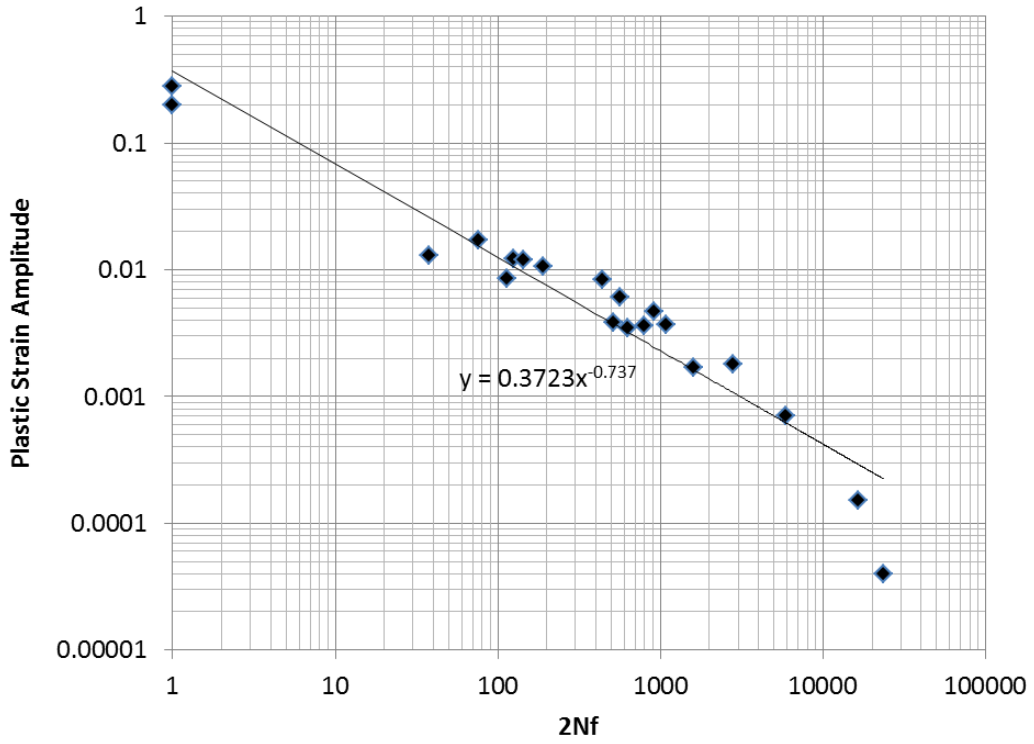

Figure 2.1: Coffin-Manson plot of data from eighteen low cycle fatigue tests and two monotonic tests of aluminum 2024-T351 (R^2=0.92).

It is clear that the data exhibits a curvature that is not captured by the straight-line fit of the Coffin-Manson equation. An ideal model would be one based on a sound physical principle *that assures the "best possible" fit to experimentally obtained fatigue test data, considering the statistical uncertainty inherent in the data*. An ideal procedure would also provide systematic guidance on constructing the model form. Below we argue that the maximum entropy concept may provide such a foundational principle.

The concept of entropy occurs in two different contexts in the literature reviewed below. The first case is represented by applications of a class of statistical methods based on information entropy (reviewed in detail below) that may be applied to fatigue data, or any other experimental data with inherent uncertainty. These applications may not refer to the *physical entropy* of the material. Alternatively, the physical entropy at a material point in a device or structure may be used to model the progress of damage at that point. In the latter instance, the process of damage

and degradation in material behavior is a fundamental consequence of the second law of thermodynamics resulting in the increase in entropy of isolated systems with time [24]. In contrast to the more commonly used parameters of stress and plastic strain, the argument is that specimen entropy has a deeper connection to the physics of the damage process.

Entropy as a purely statistical concept is used in [25] to model the variability of fatigue crack growth. A version of the maximum entropy method is shown to be a viable alternative to Bayesian updating for analyzing an evolving data population. However, the authors do not connect the concept of entropy to material damage. In [26], the maximum entropy method was used to build a statistical model of the strength distribution in brittle rocks. In [27], the authors use a combination of stress, strain and temperature data to measure the entropy generated during a low cycle fatigue test. The rate of entropy generation was shown to increase as sample failure approaches. In general, in references [25] [26], entropic dissipation at a material point was not directly used *to build a predictive fatigue life relationship*. Such a relationship is derived in [28], which is discussed further below. A material damage model dependent on specimen entropy is shown to accurately predict fatigue life.

The authors in their prior work [28] used the Maximum Entropy statistical framework to derive a fatigue life model using material entropy as a predictive variable. This approach is inspired by the work of Jaynes in [22], where he applied the information theory concept of entropy to the energy levels of a thermodynamic system and showed that known results from statistical mechanics could be obtained. Information theory entropy was thus proportional to thermodynamic entropy. The fatigue life model in [28] is expressed as a damage function and is given in Equation (2.2) below. The authors describe this approach as a Maximum Entropy Fracture Model.

$$D(t) = 1 - \exp\left(-\frac{W_t}{\rho T k_\psi}\right) \tag{2.2}$$

In Equation (2.2) the damage parameter $D(t)$ is a non-decreasing function that ranges from zero (virgin state) to one (failed state). The independent variable is the inelastic dissipation in the material, which is proportional to the entropy of the material through J2 plasticity theory and the

Clausius-Duhem inequality. The damage variable $D(t)$ was derived as a statistical cumulative distribution function (CDF) based on the maximum entropy principle. The single material parameter k_ψ in Equation (2.2) was obtained from *isothermal* mechanical cycling tests and then used to model fatigue crack propagation *under thermal cycling conditions* in an electronic assembly. Figure 2 shows a comparison of the estimated/actual number of cycles as well as crack fronts at an intermediate stage with the same area of crack from both the finite element simulation and thermal cycling fatigue test.

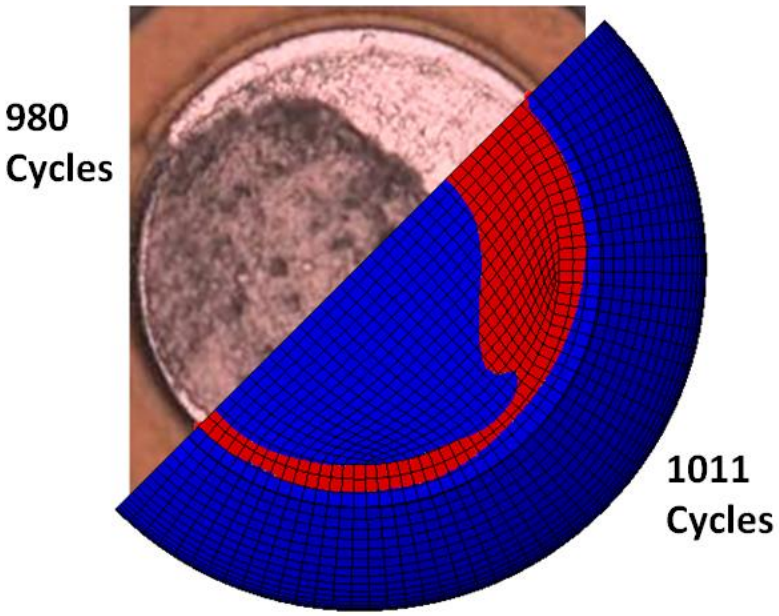

Figure 2.2: Comparison of crack fronts predicted by a single-parameter maximum entropy model against the experimentally observed creep-fatigue crack in a Sn3.8Ag0.7Cu solder joint under thermal fatigue cycling [28]. (permission pending).

Building on the work in [28], in this paper, we propose to develop a systematic procedure for development of maximum entropy models for describing metal fatigue. We demonstrate the approach using low-cycle fatigue experimental data for Aluminum 2024-T351 material and generalize the application of maximum entropy principle using a broader class of statistical distributions, including the truncated exponential and the truncated normal distribution. We begin first with a brief review of the maximum entropy principle.

2.4 A Review of the Maximum Entropy Principle

The concept of entropy as applied to heat engines is due to Clausius, but the connection of entropy to the probability of the states of a thermodynamic system began with Boltzmann. Boltzmann demonstrated that the second law of thermodynamics for an ideal gas is a consequence of the mechanics of the collisions of the molecules [29]. He showed that a sufficiently large number of interrelated deterministic events will result in random states. He derived the following function, given in Equation (2.3), for a uniform distribution and argued that this quantity had the same physical meaning as the entropy of Clausius. This led to the Boltzmann H function:

$$H(p) = \sum_i p_i \ln p_i \quad p_i = p = \frac{1}{n} \tag{2.3}$$

The above expression is closely related to Gibb's entropy formula:

$$S(p) = -k_b \sum_i p_i \ln p_i \tag{2.4}$$

Shannon's research in information theory led to a mathematical expression (discussed later in Equation (2.6)) strikingly similar to the thermodynamic entropy formulas of Boltzmann and Gibbs described above. It is important to note that Shannon's argument was a purely statistical one and no physical significance was claimed. It was not until the work of Jaynes [22] that a connection between the information entropy of Shannon and Thermodynamic entropy was established.

Here, we describe the abstract development of Shannon's formula based on a counting argument [30]. Consider the information content of a whole number that can range in value from 0 to N. If we claim that each digit of the number is a unit of information, then it clearly takes $\log_b N$ digits to represent the number in a base b system. If the base of the logarithm is changed, the

resulting information will change by a constant, but the ratios of information for different N will be preserved, provided the same base is used for all of them. Thus, $\log_b N$ is a reasonable measure of the information contained in a variable that can range from 0 to N. If we consider a random experiment with N possible equally likely, mutually exclusive outcomes, then the information contained in a given outcome is still $\log_b N = -\log_b p$ with p being the probability of the event. We argue that the information in a given event is strictly determined by p regardless of how the remaining $1 - p$ probability is allocated to other events. Thus, even if the events do not have equal probabilities, the information for any given event is still $-\log_b p$ [10]. This function has the expected property that the information contained in the occurrence of two (or more) statistically independent events is the sum of the information in each of the events separately, as shown below in Equation (2.5). This property is fundamentally important (as pointed out in [8]) and further reinforces the argument for the $-\log_b p$ measure of information.

$$I(p) = -\ln p_i \tag{2.5}$$

$$I(p_i p_j) = I(p_i) + I(p_j) \quad : i \neq j$$

If the events correspond to a discrete random variable, then they must be mutually exclusive and the probability of the union of the sequence of the events is equal to one [21]. The entropy of the density function is taken as the expected value of the information in the events [31]. This leads to the Shannon information entropy formula:

$$H(p) = E[I(p)] = -\sum_i p_i \ln p_i \tag{2.6}$$

This function (and only this function) satisfies these three conditions:

1. Continuity: It is a continuous function of the p_i
2. Monotonicity: It is an increasing function of *n*, if all the p_i are equal
3. Composition: If an event can be decomposed into two or more lower level events, the function $H(p)$ will evaluate identically whether the lower of higher level events are used in

the computation, provided that the appropriate conditional probabilities are used to relate the higher and lower level events.

Jaynes [8] noted that there is a symbolic similarity between the expressions for thermodynamic (Gibbs) entropy (Equation (2.3)) and Shannon's information entropy (Equation (2.6)), but commented that the similarity did not necessarily imply a deeper connection. Jaynes then proceeded to show that a connection did exist and that many results of statistical thermodynamics could be interpreted as *applications* of Shannon's information entropy concept to physical systems. The expression for Gibbs entropy is the result of a development involving various physical assumptions, some based on experimental evidence, and some not. Conversely, Shannon's entropy is based on mathematical and logical reasoning, not physical evidence. Shannon's model was developed to model the abstract mathematical properties of digital communication and, prior to Jaynes, was not claimed to be applicable to the physical sciences. Shannon defined the entropy of a discrete probability distribution as Equation (2.6).

The Maximum Entropy method as set forth by Jaynes is as follows [22]: the probability mass function that maximizes Equation (2.6), subject to constraint Equations (2.7) and (2.8), is the best choice if no other information is available to specify the probability distribution.

$$\sum_i p_i = 1 \tag{2.7}$$

$$E[g(x_i)] = \sum_i p_i g(x_i) \quad : x_i \in \{x_1, x_2, \dots x_i \dots x_m\} \tag{2.8}$$

The following probability mass function (Equation (2.9)) can be shown to maximize Equation (2.6):

$$p_i = e^{-\lambda_0 - \lambda_1 g(x_i)} \tag{2.9}$$

The constants λ_0 and λ_1 are Lagrange multipliers associated with the constraints. Jaynes calls this approach the Maximum Entropy Method and probability functions so derived, maximum

entropy distributions (MaxEnt method and MaxEnt distributions). Multiple expected value constraints may be applied (not simply moments as is common in probability analysis), resulting in the following form of the MaxEnt distribution:

$$p_i = e^{-\lambda_0 - \lambda_1 g_1(x_i) - \cdots - \lambda_m g_m(x_i)} \tag{2.10}$$

The entropy of the resulting distribution is [8]:

$$S_{max} = \lambda_0 + \lambda_1 E[g_1(x)] + \cdots + \lambda_m E[g_m(x)] \tag{2.11}$$

Jaynes' argument was for the discrete case. The entropy of a continuous probability density function is also known and is defined as [21]:

$$H\big(f(x)\big) = -\int_{-\infty}^{\infty} f(x) \ln f(x) dx \tag{2.12}$$

The corresponding continuous version of Equation (2.10) is given below [21]:

$$f(x) = e^{-\lambda_0 - \lambda_1 g_1(x) - \cdots - \lambda_m g_m(x)} \tag{2.13}$$

One important point regarding Equation (2.13) is that it is only a probability density function for specific values of the parameters λ_k. This situation differs from the usual approach to representing probability density functions or distribution functions where the functions are admissible for ranges of parameter values. Additionally, the method Jaynes sets forth assumes that the values used for moment function constraints are not estimates subject to sampling variation. They are taken as essentially exact values of the distribution moment functions. This assumption differs from traditional inferential statistics where moments or quantiles are estimated from data and sampling errors are estimated.

Jaynes showed that if we choose the probability distribution for the system microstates based on maximizing Shannon entropy, known results from statistical mechanics can be obtained, without new physical assumptions, and in particular, the thermodynamic entropy of the system is found to be the Gibbs entropy of Equation (2.4). The Shannon entropy of the distribution is proportional to the physical entropy of the system if (and only if) the probability distribution is applied to the thermodynamic states of the system. Jaynes [22] argues that this shows that

thermodynamic entropy is an application of a more general principle. Further to this point, Jaynes argues that if a probability model is required for some application, where certain expected values are known, but not other details, the maximum entropy approach should be used to find the probability distribution. Jaynes uses the term 'maximally non-committal' to describe probability distributions obtained by this process. What is known about the random variable in question is captured in mathematical constraints, while the principle of maximum entropy accounts for what is not known. While information entropy is only proportional to thermodynamic entropy in certain circumstances, Jaynes argues that choosing the probability density function that maximizes the Shannon entropy subject to various constraints is appropriate to any situation where a reference probability distribution is needed. The application could be physical or not, and need not necessarily have a relationship to thermodynamic states.

2.5 Maximum Entropy Distributions

We argue that if a given parametric family of distributions is selected for some reason (as is common practice), then within that family of distributions, we should prefer the parameter values that maximize entropy (subject to any constraints) over those that do not. For example, if the Weibull distribution has already been chosen for some application, and the characteristic life is known, then the Weibull exponent should be chosen to maximize entropy. It is noteworthy that the Exponential distribution and the Normal distribution are the MaxEnt distributions corresponding to a prescribed mean value, and prescribed mean and variance values respectively [32]. Given the fundamental importance of these distributions in statistical theory, it is informative that they can be directly derived from the principles of maximum entropy. Just as Jaynes showed that statistical thermodynamic results derivable by other means could be obtained from maximum entropy methods, it has also been shown that the well-known and fundamental Normal distribution, traditionally derived by other means, can also be based on a maximum entropy argument. Even the Weibull distribution can be derived from a maximum entropy approach if appropriate moment functions are chosen [32].

Table 2.1: MaxEnt distributions corresponding to moment functions $g_r(x)$.

Support	*Type*	$g_r(x)$	*Distribution Function*	*Reference*
[a, b]	Discrete	N.A.	*Uniform*	[22]
[0, ∞)	Discrete	x	*Exponential*	[22]
[0, ∞)	Continuous	x	*Exponential*	[32]
[0, a]	Continuous	x	*Truncated Exponential*	[33]
[0, ∞)	Continuous	x^2	*Half Normal*	[34]
(-∞, ∞)	Continuous	x, x^2	*Normal*	[32]
[0, ∞)	Continuous	x, x^2	*Left Truncated Normal*	[34]
[0, a]	Continuous	x, x^2	*Left and Right Truncated Normal*	[34]
[0, ∞)	Continuous	*ln(x)*, x^β	*Weibull*	[32]

Note the references to truncated distributions in Table 2.1. A distribution is described as *truncated* if the value of its density or mass function is forced to zero (when otherwise it would be non-zero) outside of specific range. Thus, the truncated Normal distribution functions can be thought of as ordinary normal probability density functions (PDFs) that are clipped to zero probability outside of their non-zero range. As described later, they are multiplied by a normalizing constant to correct for the missing density. Truncation at $x = 0$ is necessary for applications to non-negative variables. The CDF of a truncated Normal random variable has a finite slope at $x = 0$. If a second truncation at $x = a$ is specified, then the CDF is forced to be exactly equal to 1 for all $x \geq a$. We begin the discussion of MaxEnt distributions with the truncated exponential distribution.

2.6 MaxEnt Form of Truncated Exponential Distribution

The truncated Exponential distribution can be constructed in an analogous fashion for positive values of λ (parent PDF is a decreasing function). An example is plotted in Figure 2.3. However, it is possible for a truncated exponential distribution to be an increasing function within its non-zero range (Figure 2.4). Clipping the positive exponent at some specified value enables its use as a PDF. This corresponds to a negative-valued lambda, which is not admissible in the non-truncated case. If the specified mean was to the right of the midpoint of the non-zero range, then lambda would be negative.

It should also be noted that changing the location of a distribution function without changing its shape has no effect on the entropy value. Thus, a left endpoint other than zero could be used for any of the distributions that have zero value for negative x. Naturally, this shift would change the moment function values. Note that specifying a right truncation value changes the shape of the remaining distribution function and should be thought of as adding an extra parameter. Thus, a truncated exponential distribution is a two-parameter distribution.

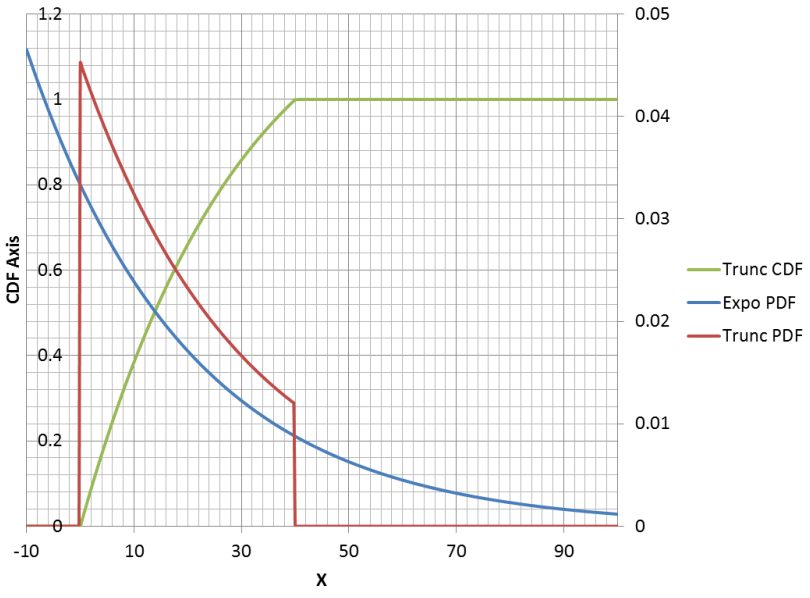

Figure 2.3: Truncated Exponential distribution with λ= 0.03; a = 40.

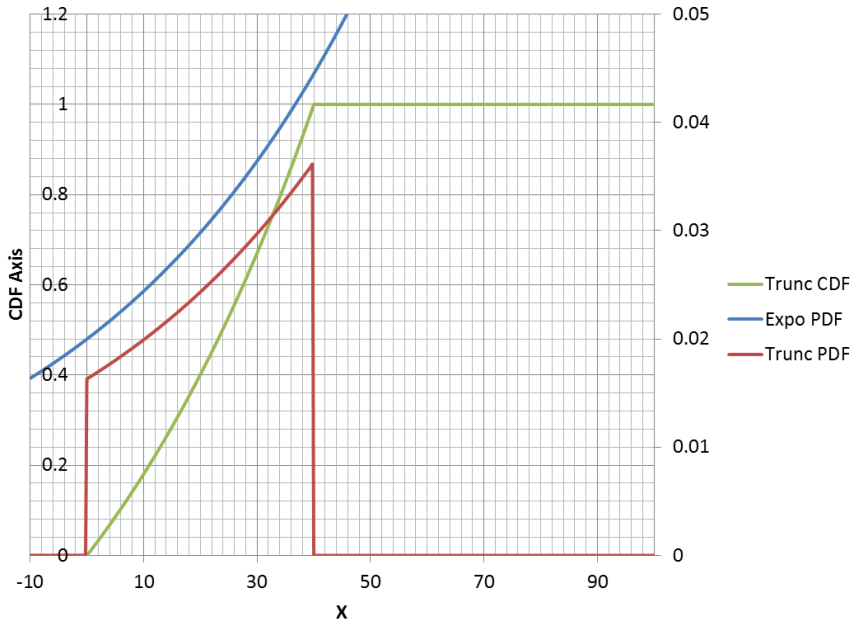

Figure 2.4: Rising truncated Exponential distribution with λ= -0.02; a = 40.

Truncated Exponential Distribution: PDF and CDF

$$f_{trunc}(x,\lambda,a) = \frac{\lambda\, Exp(-\lambda x)}{1 - Exp(-\lambda a)} \quad for\ \ 0 \le x \le a \tag{2.14}$$

$$F_{trunc}(x,\lambda,a) = \frac{1 - Exp(-\lambda x)}{1 - Exp(-\lambda a)} \quad for\ \ 0 \le x \le a$$

Expected Value of a Truncated Exponential random variable

$$E(x) = \frac{1}{\lambda}\left(\frac{1 - (\lambda a + 1)Exp(-\lambda a)}{1 - Exp(-\lambda a)}\right) \tag{2.15}$$

Note that the uniform distribution is a limiting case of the truncated exponential distribution and corresponds to lambda approaching zero. An example is shown in Figure 2.5.

$$\lim_{\lambda \to 0} f_{trunc}(x, \lambda, a) = \frac{1}{a} \quad for \;\; 0 \leq x \leq a \tag{2.16}$$

$$\lim_{\lambda \to 0} E(x) = \frac{a}{2}$$

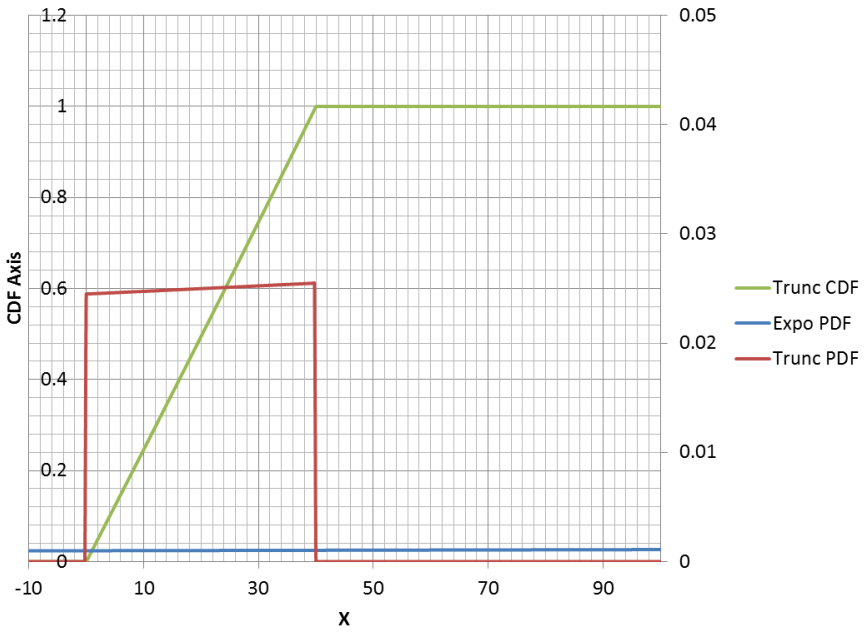

Figure 2.5: Rising truncated Exponential distribution with λ = -0.001; a = 40.

2.7 MaxEnt Form of Truncated Normal Distribution

The truncated Normal distribution can be explained in terms of the Normal PDF. For $x \geq 0$, the PDF has the same shape as a non-truncated Normal PDF, but scaled to make up the density lost for $x < 0$ (Figure 2.6). The truncation of the portion of the density less than zero changes the mean and standard deviation from the parameters that the truncated distribution inherits from the Normal distribution. Adding a second truncation point at $x = a$ forces the function be equal to 1

for all $x \geq a$ and adds a corner to the CDF at $x = a$ (Figure 2.7). Additionally, the correction factor must be larger to correct for missing density $x < 0$ and also $x \geq a$.

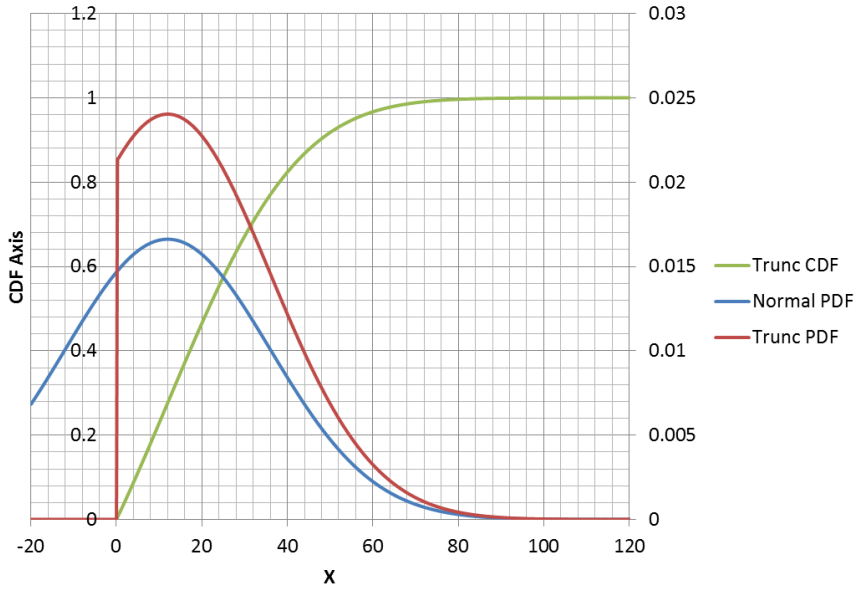

Figure 2.6: Truncated Normal distribution plotted with the parent (non-truncated) Normal distribution density correction for $x \geq 0$ equal to 1.23.

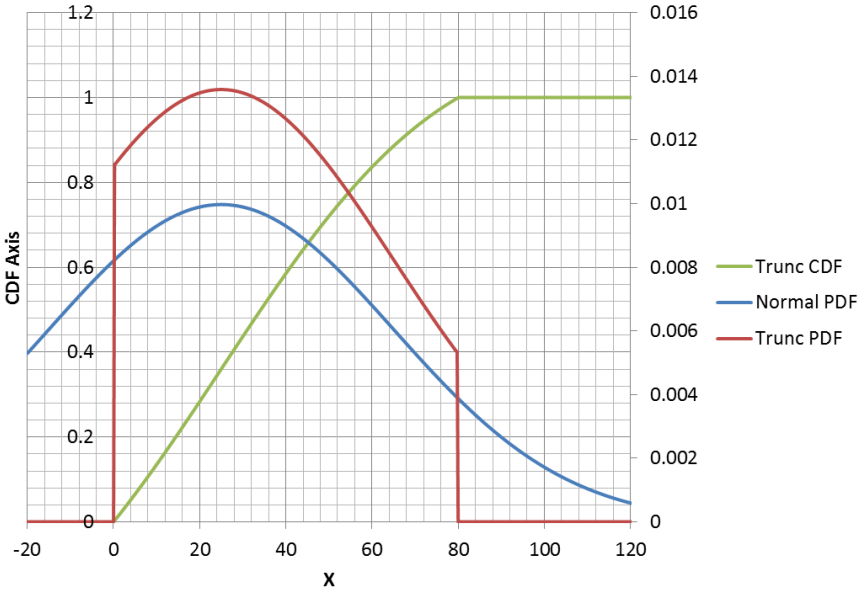

Figure 2.7: Left and right truncated normal distribution.

The PDF and the CDF for the left truncated Normal distribution can be shown to be:

$$Normal\ CDF\ in\ terms\ of\ Standard\ Normal\ CDF \tag{2.17}$$

$$F_{norm}(x,\mu,\sigma) = \Phi\left(\frac{x-\mu}{\sigma}\right)$$

$$F_{trunc}(x,\mu,\sigma) = \frac{F_{norm}(x,\mu,\sigma) - F_{norm}(0,\mu,\sigma)}{1 - F_{norm}(0,\mu,\sigma)} \quad for\ x \geq 0$$

$$f_{trunc}(x,\mu,\sigma) = \left(\frac{1}{1 - F_{norm}(0,\mu,\sigma)}\right)\frac{1}{\sigma\sqrt{2\pi}}Exp\left(-\frac{(x-\mu)^2}{2\sigma^2}\right) \quad for\ x \geq 0$$

The factor in the denominator of the CDF definition in Equation (2.17) is the area correction factor C.

$$C = \frac{1}{1 - F_{norm}(0,\mu,\sigma)} \tag{2.18}$$

Truncated Normal Distribution in two-parameter MaxEnt form is:

$$f_{trunc}(x,\mu,\sigma) = Exp(-\lambda_0 - \lambda_1 x + \lambda_2 x^2) \tag{2.19}$$

$$\lambda_0 = -\frac{\mu^2}{2\sigma^2} - \ln\left(\frac{C}{\sigma\sqrt{2\pi}}\right) \quad \lambda_1 = -\frac{\mu}{\sigma^2} \quad \lambda_2 = \frac{1}{2\sigma^2}$$

Thus, just as the Normal distribution is MaxEnt for moment functions x, x^2 where x ranges over $(-\infty, \infty)$, the truncated Normal distribution is MaxEnt for the same moment functions over the range $[0, \infty)$. Note that the μ and σ are the mean and standard deviation of the parent (un-truncated) normal distribution, not the truncated normal distribution.

2.8 MaxEnt Form of the Weibull Distribution

Since the Weibull distribution is widely used, it is useful to know what parameter value choices maximize the entropy of the function. It is often the case that only one of the two parameters is known and we seek a rational approach to assigning a value to the second parameter. In this case, we suggest that choosing the parameter value that maximizes the entropy of the distribution is the correct approach.

The entropy of the Weibull distribution is (Figure 2.8, derived from Equation (2.80c) in [35]):

$$H = \gamma\left(1 - \frac{1}{\alpha}\right) + \ln\left(\frac{\beta}{\alpha}\right) + 1 \tag{2.20}$$

$$\gamma = 0.577216 \ldots \ Euler's\ constant$$

Mean of a Weibull distribution is [35]:

$$\mu = \beta\Gamma\left(1 + \frac{1}{\alpha}\right) \tag{2.21}$$

Thus, the entropy for a Weibull distribution with a fixed mean (moment constraint on *x*) is:

$$H_\mu = \gamma\left(1 - \frac{1}{\alpha}\right) + \ln(\mu) - \ln\left(\Gamma\left(1 + \frac{1}{\alpha}\right)\right) - \ln(\alpha) + 1 \tag{2.22}$$

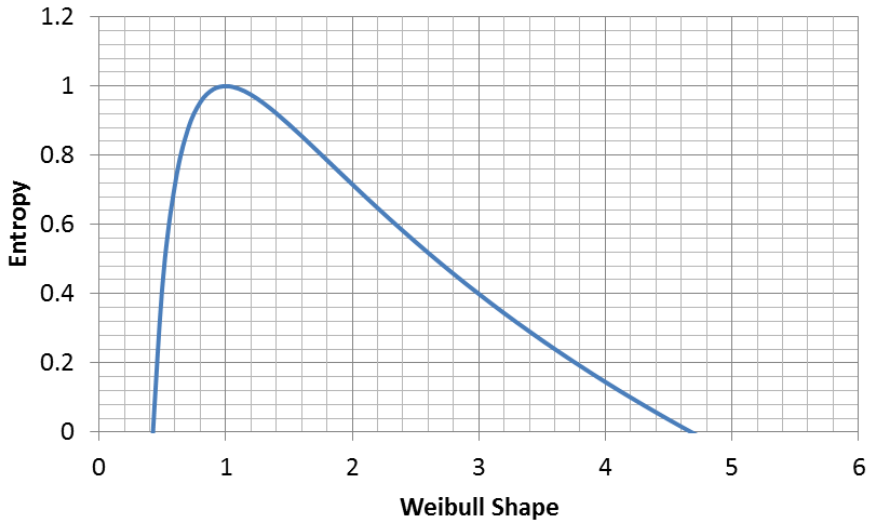

Figure 2.8: Entropy of a Weibull distribution with a fixed mean.

Maximizing the entropy function:

$$\frac{dH_\mu}{d\alpha} = 0 \tag{2.23}$$

Recalling the properties of the digamma function:

$$\psi(x) = \frac{d}{dx}\left[\ln\left(\Gamma(x)\right)\right] \tag{2.24}$$

$$\psi(1+x) = \psi(x) + \frac{1}{x}$$

Therefore:

$$\frac{dH_\mu}{d\alpha} = \frac{\gamma}{\alpha^2} + \frac{\psi\left(1+\frac{1}{\alpha}\right)}{\alpha^2} - \frac{1}{\alpha} = 0 \tag{2.25}$$

$$\psi\left(\frac{1}{\alpha}\right) = -\gamma$$

This is only true for $\alpha = 1$. Thus, within the Weibull family of distributions, for a given fixed mean, the exponential distribution has the highest entropy, in agreement with Jaynes' result.

Maximum Entropy for Fixed Characteristic Life is (Figure 2.9):

$$H = \gamma\left(1 - \frac{1}{\alpha}\right) + \ln\left(\frac{\beta}{\alpha}\right) + 1 \;\; for\; \beta = const. \tag{2.26}$$

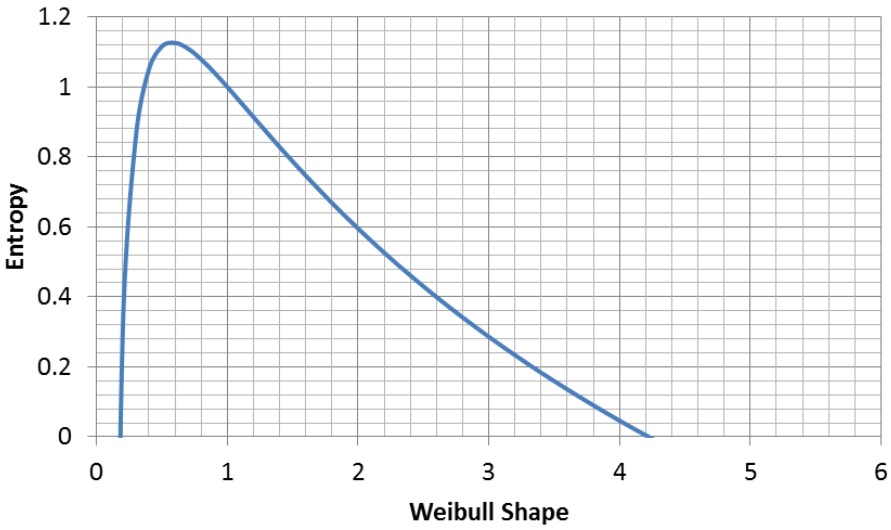

Figure 2.9: Plot of Equation (2.26) for $\beta = 1$.

Proceeding as above:

$$\frac{dH}{d\alpha} = \frac{\gamma}{\alpha^2} - \frac{1}{\alpha} = 0 \tag{2.27}$$

$$\gamma = \alpha$$

Thus, for the fixed characteristic life case, $\alpha = \gamma$, the Euler's constant.

2.9 Application of Maximum Entropy to Low Cycle Fatigue of 2024-T351 Aluminum

When a specimen is subjected to axial load cycles of a magnitude sufficient to cause plastic deformation, the stress/strain history for the specimen can frequently be described as a loop, such as shown in Figure 2.10. To determine the fatigue life of the specimen, the load cycles are applied until the specimen fails, or until its compliance exceeds some proportion of its initial compliance. The Coffin-Manson relationship (Equation (2.1)) is commonly used to model the relationship between plastic strain range and reversals to failure. The parameter $\epsilon_f{}'$ is determined by fitting the curve to fatigue data. It is frequently close in value to ϵ_f.

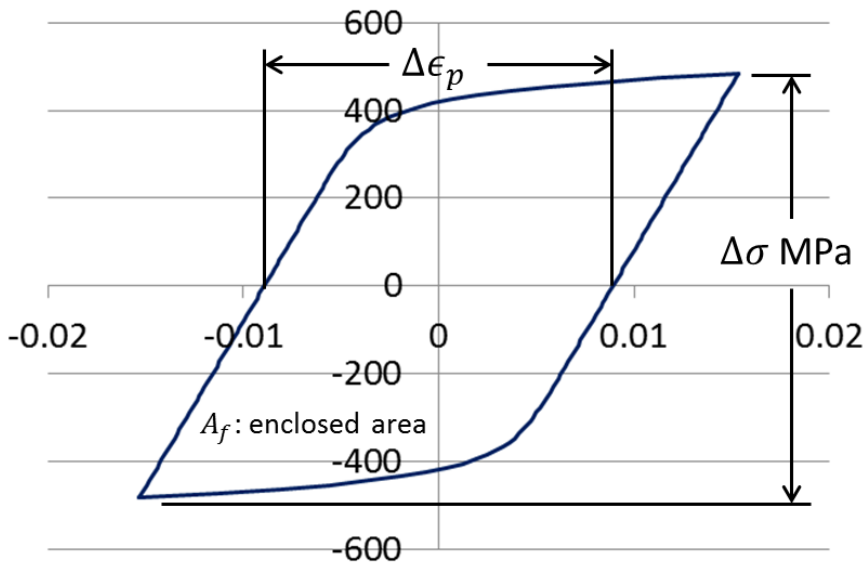

Figure 2.10: Stress/Strain loop showing plastic strain,
variables are defined in Table 2.2.

As mentioned earlier, a sequence of low cycle fatigue tests, and two monotonic tension tests, was performed on tension specimens of 2024-T351 aluminum. Eighteen specimens were tested under constant amplitude, fully-reversed fatigue conditions. In five cases, representative stress/strain loops were collected at various cycle intervals. Two specimens were tested to failure monotonically. The data collected is summarized in Table 2.2. The data is fitted to a Coffin-Manson model as shown in Figure 2.1.

Table 2.2: Low cycle fatigue data summary.

k	$2N_f$	*Stress Amplitude MPa*	*Plastic Strain Amplitude*	*Data*
1	1	537.810	0.2	Values
2	1	558.495	0.28	Values
3	76	503.335	0.01725	Values
4	38	495.061	0.0129	S-20 Loop fitted
5	124	492.993	0.0123	Values
6	144	482.650	0.012	Values
7	190	475.755	0.01067	Values [36]
8	114	477.824	0.0085	S-17 loop fitted
9	440	466.792	0.0083	Values [36]
10	560	448.175	0.00606	Values [36]
11	920	437.143	0.00472	Values [36]
12	516	453.691	0.0038	S-12 loop fitted
13	1080	441.280	0.0037	Values
14	800	441.280	0.0036	Values
15	624	454.381	0.0035	S-11 loop fitted
16	2800	398.531	0.00178	Values [36]
17	1608	430.938	0.0017	S-18 loop fitted
18	5860	403.358	0.0007	Values
19	16336	351.645	0.00015	Values
20	23400	358.540	0.00004	Values

As mentioned earlier, the data exhibits a curvature that is not captured by the straight line fit of the Coffin-Manson power law. An alternative approach to modeling data such as this, using concepts developed from Maximum Entropy, is developed below. The authors of [28] showed that material entropy is proportional to inelastic dissipation in experiments such as this where the temperature of the specimens is essentially constant. Thus, inelastic dissipation is exploited as a surrogate for entropy in the development that follows.

The variable D representing the ability of the material at a point to bear load is fundamental in the literature of damage mechanics [2]. The value of $D = 0$ (undamaged) represents virgin material, while $D = 1$ is taken to correspond to failed material. The variable D is a non-

decreasing quantity since damage is inherently irreversible. The Coffin-Manson equation can be rewritten in terms of damage and doing so will be shown to provide a departure point for further development. We begin by rearranging Equation (2.1) into the following form:

$$\frac{1}{2N_f} = \left(\frac{\Delta\epsilon_p}{2\epsilon_f'}\right)^{-\frac{1}{c}} \tag{2.28}$$

Depending on the application, the damage variable D may be expressed as a function of various independent variables. In fatigue applications, it is common to use the following (applicable to constant damage per load cycle) Palmgren-Miner definition of damage. It is understood that N_f may depend on other variable such as temperature or plastic strain amplitude.

$$D(N) = \frac{N}{N_f} \tag{2.29}$$

We can write the damage accumulation per reversal:

$$D_{rev} = \frac{1}{2N_f} \tag{2.30}$$

Finally, Equation (2.28) can be recast as a damage equation as follows:

$$D_{rev} = \left(\frac{\Delta\epsilon_p}{2\epsilon_f'}\right)^{-\frac{1}{c}} = fcn(\Delta\epsilon_p) \tag{2.31}$$

Following [28], we propose to develop a function of form of Equation (2.31) in terms of energy per reversal, rather than plastic strain range. This relationship will have the form:

$$D_{rev} = fcn\left(\frac{W_f}{2N_f}\right) \tag{2.32}$$

In the development that follows, a general approach to deriving functions of the form of the above equation will be proposed. In order to apply an equation of the above form to the data in Table 2.3, we first need to determine the inelastic dissipation per reversal corresponding to each of the test conditions of the form shown in Figure 2.10. The energy expended in inelastic dissipation, for a cyclic test under constant conditions is given by the area enclosed by the loop. Note that in Table 2.3, actual loop data was only available for five of the 20 tests. In all cases the plastic strain range and stress range (and reversals to failure) were collected. Fortunately, the shapes of the loops follow known trends and thus it was possible to deduce the inelastic dissipation for the tests where loops were not available to measure. The inelastic dissipation for the two monotonic tests were also deduced from the available loop data, although a different analytical approach was used.

Plotted loops for the five loop-data samples are given below in Figures 2.11-2.15. In each case, several loops were provided.

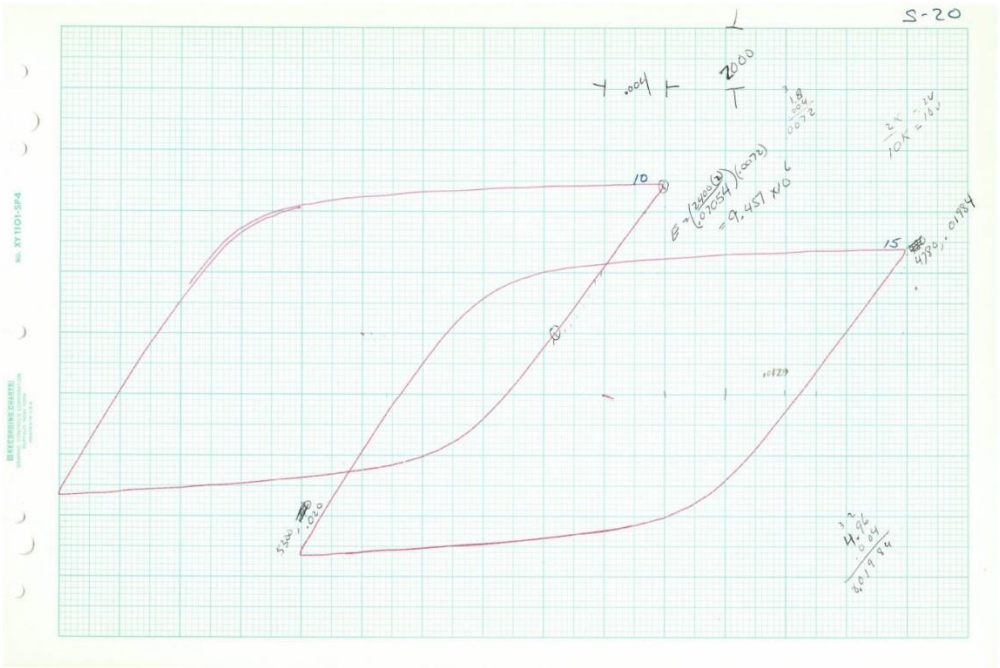

Figure 2.11: Test 4, 2Nf = 38.

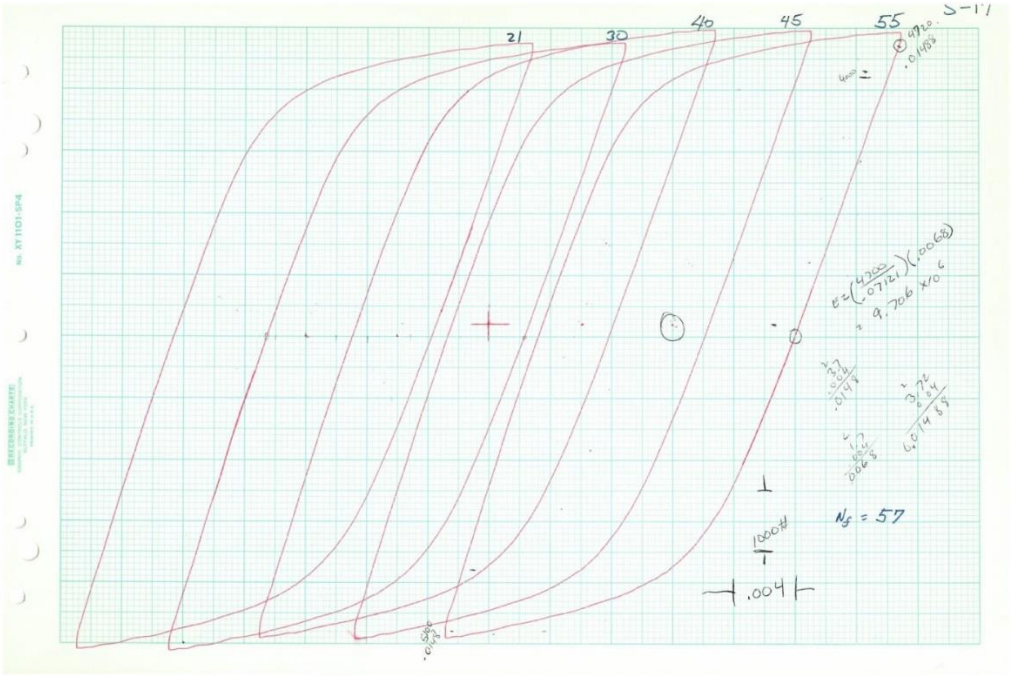

Figure 2.12: Test 8, 2Nf = 114.

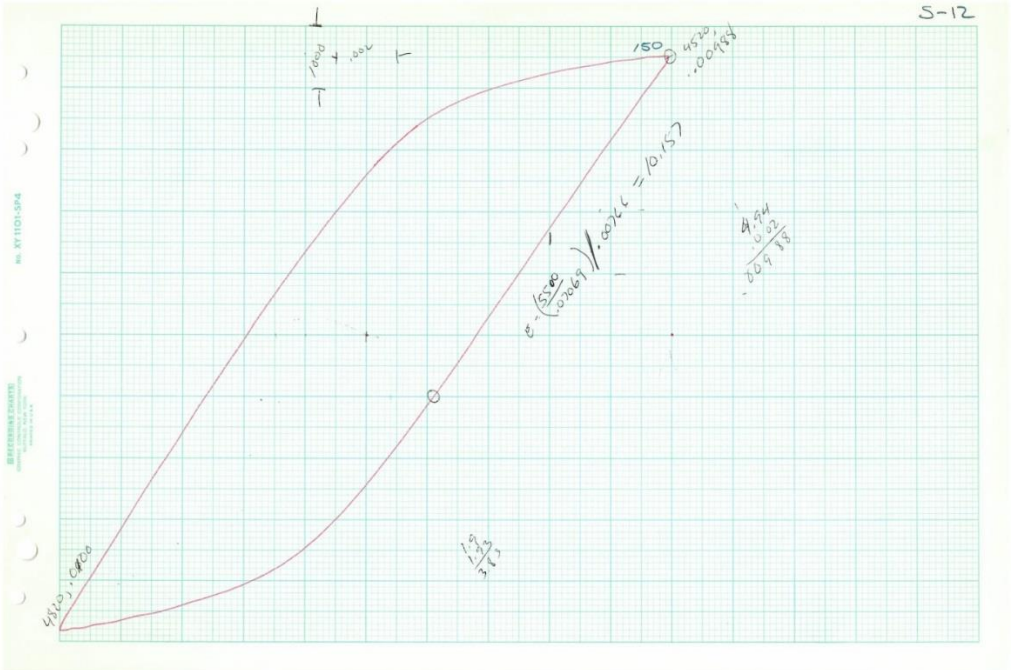

Figure 2.13: Test 12, 2Nf = 516.

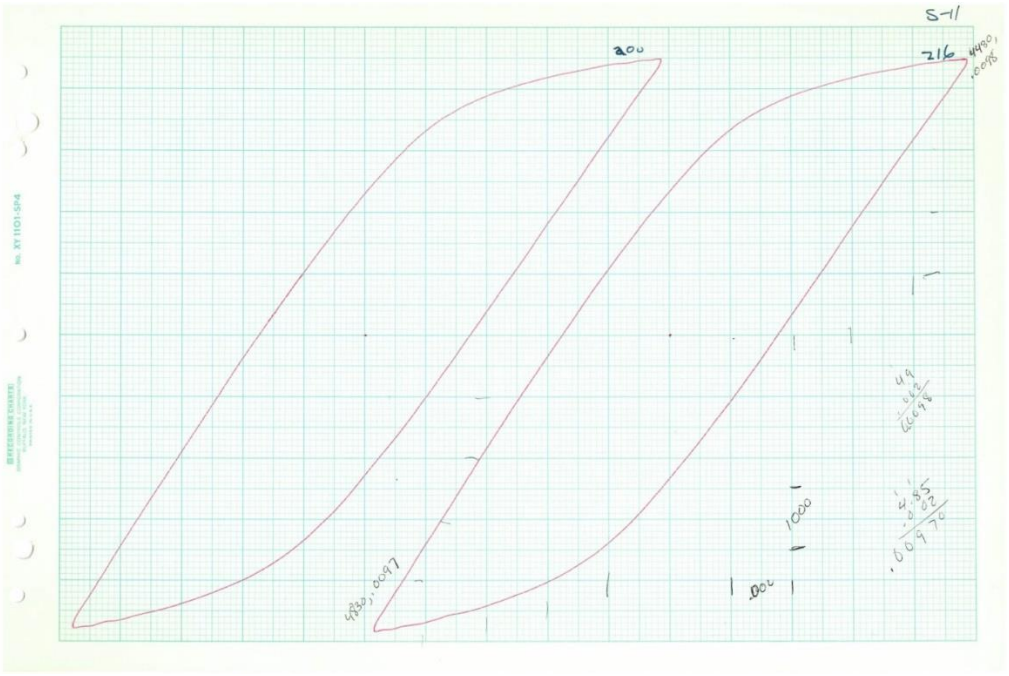

Figure 2.14: Test 15, 2Nf = 624.

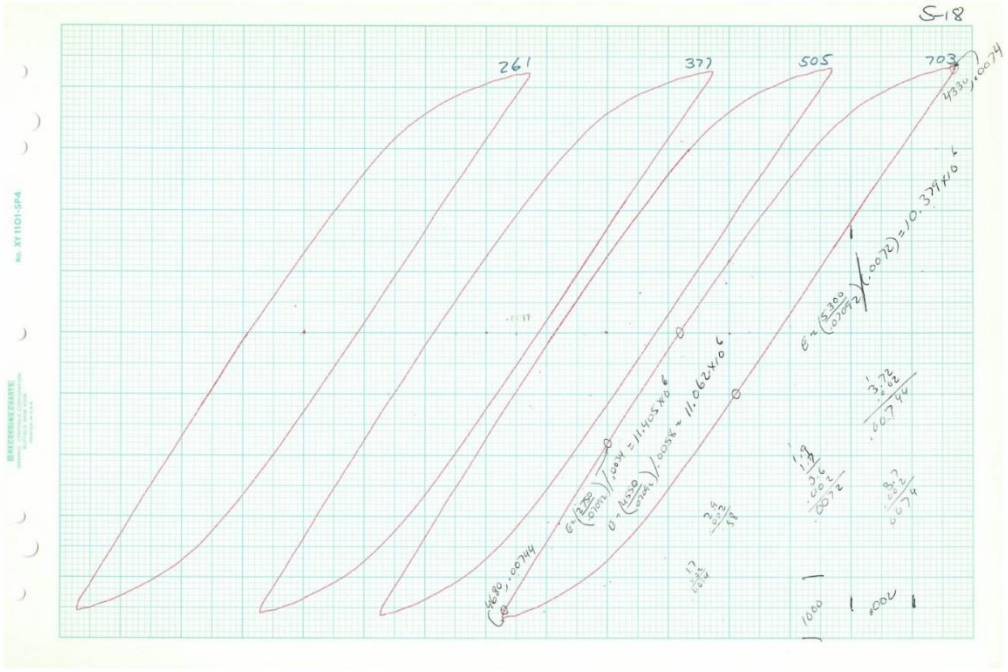

Figure 2.15: Test 17, 2Nf = 1608.

The Ramberg-Osgood relationship (Equation (2.33)) is frequently successful for modeling data such as this. This model assumes that the plastic portion of the strain range is a power law of the stress range. There is no explicit yield point with this model. The total strain range is given by Equation (2.34) and is used to model the shapes of the loops. For the purposes of fitting Equation (2.34), the origin of the stress and strain range variables is placed at the lower left corner of the loop.

Ramberg-Osgood Plasticity Model for Stress-Strain Loops is [2]:

$$\Delta\epsilon_p = \left(\frac{\Delta\sigma}{K}\right)^{\frac{1}{n}} \tag{2.33}$$

$$\Delta\epsilon_{total} = \frac{\Delta\sigma}{E} + \left(\frac{\Delta\sigma}{K}\right)^{\frac{1}{n}} \tag{2.34}$$

The fits of Equation (2.34) to loop data was performed using the least squares approach and is shown in Figure (2.16). The fits to the data were of high accuracy as demonstrated by the R^2 value of 0.997. This confirms that Equation (2.34) provides a reasonable model of the shape of the loops in Figures 2.11-2.15. The points are samples measured from the loops while the line is the fit of Equation (2.34). A separate fit was performed for the parameters in Equation (2.34) for each of the five loops. A common value of Young's Modulus was fit simultaneously to the five sets of data. Specific values of *n* and *K* were obtained for each loop.

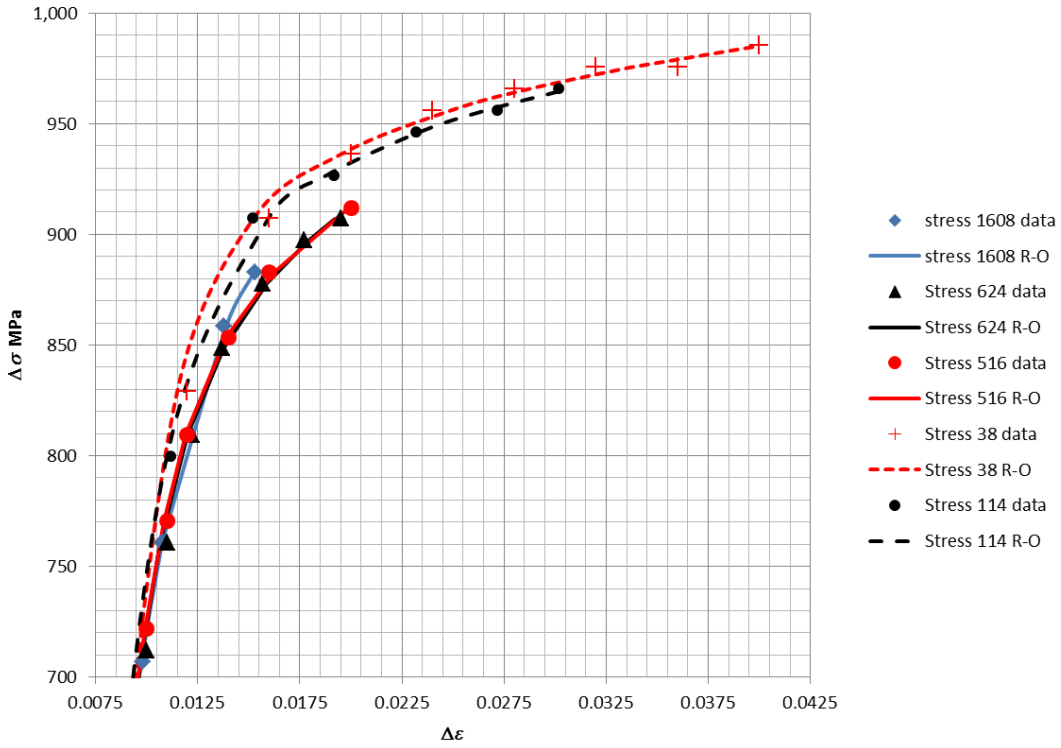

Figure 2.16: Fit of Equation (2.34) to 5 data sets (E = 7.38E4 MPa for all fits) (R^2=0.997).

The five sets of parameters obtained from the fitted loops were used to estimate the parameter *1/n* for the remaining 15 tests. The fitted *1/n* value was found to be a strictly increasing function of plastic strain range and is plotted in Figure 2.17. The 'interpolation' line markers show the values of *1/n* used for the remaining 15 tests. The values were linearly interpolated between the maximum and minimum values. For plastic strain ranges outside the range of the measured data, the value of the nearest measured data value was used. As will be shown below, the predicted inelastic dissipation is mainly determined by the plastic strain range and the stress range and is only weakly dependent on the value of *1/n* used.

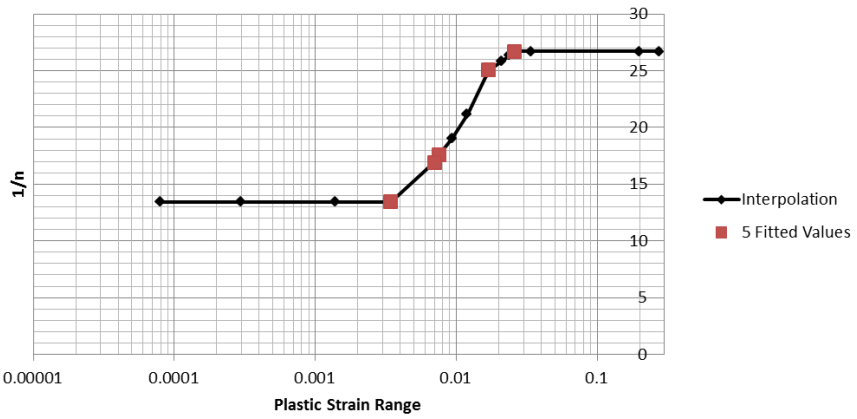

Figure 2.17: 5 Fitted values of $1/n$ with interpolation function.

The five loops (represented by Equation (2.34)) are plotted in Figure 2.18 below using the parameters fit to the corresponding loop data. The inelastic dissipation per cycle is the area enclosed by the loop.

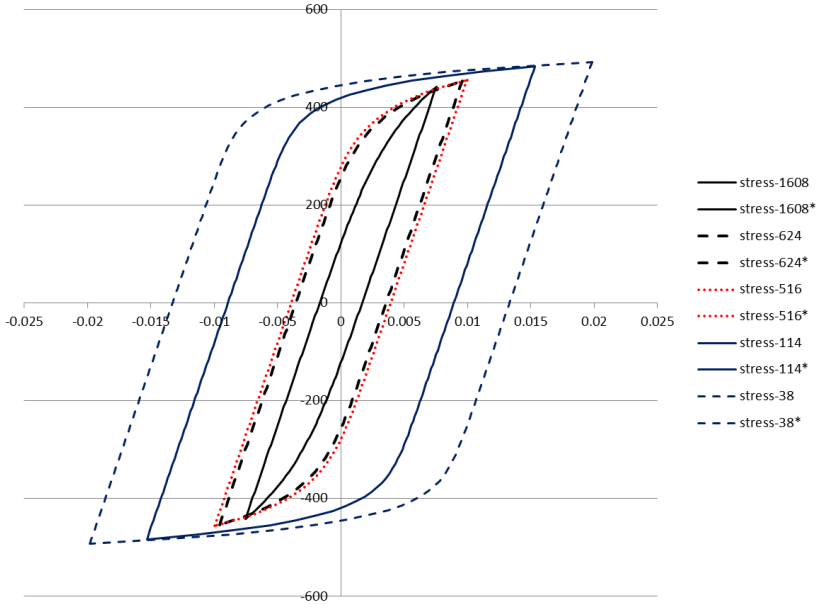

Figure 2.18: Ramberg-Osgood curves based on loop fits.

The area of the loop in terms of the parameters in Equation (2.34) and the loading parameters is given in Equation (2.35). The form of this equation has the advantage that it is relatively robust

to errors in fitting the parameter *n*, since both of the actual measured values of the stress range and strain range are used.

Loop Area (dissipation per cycle) in terms of *n* is [2]:

$$A_f = \frac{1-n}{1+n}\Delta\sigma\Delta\epsilon_p \tag{2.35}$$

In the present case, we wish to describe the evolution of damage in terms of reversals, rather than cycles. It is apparent from Equation (2.36) that the inelastic dissipation per reversal is half the area of the loop given by Equation (2.35), and is given in Equation (2.37).

Total Inelastic Dissipation in terms of cycles and reversals:

$$W_f = N_f A_f = \left(2N_f\right)\left(\frac{1}{2}A_f\right) \tag{2.36}$$

Inelastic dissipation per reversal:

$$\frac{W_f}{2N_f} = \frac{1-n}{2(1+n)}\Delta\sigma\Delta\epsilon_p \tag{2.37}$$

For specimens subjected to a monotonic test, the inelastic dissipation is the area under the plastic portion of the stress strain curve. If the plastic portion of the curve is modeled by an equation of the form of Equation (2.34), the area under the plastic portion is given by Equation (2.38). A monotonic test to fracture can be interpreted as a fatigue test with failure occurring after a single reversal. Thus, the inelastic dissipation per reversal is given by Equation (2.39):

Monotonic Area (Dissipation per reversal) in terms of n:

$$A_f = \frac{1}{1+n}\sigma_f \epsilon_f \tag{2.38}$$

Inelastic Dissipation for a Monotonic Test:

$$\frac{W_f}{2N_f} = A_f = \frac{1}{1+n}\sigma_f \epsilon_f \quad 2N_f = 1 \tag{2.39}$$

Note that in Equations (2.37) and (2.39), the area is computed from plastic strain range multiplied by stress range times a factor dependent on *n*. The functions are given in Equation (2.40) and the values of ρ are summarized in Table 2.4 and plotted in Figure 2.19.

$$\rho_{mono} = \frac{1}{1+n} \tag{2.40}$$

$$\rho_{loop} = \frac{1-n}{1+n}$$

Note that the value of ρ does not change greatly as *n* is varied. This observation indicates that the computation of areas for the monotonic and cyclic tests is robust to errors in fitting the Ramberg-Osgood parameter *n*. Thus, the inference of inelastic dissipation for the 2.15 tests for which loop data was not available is justified.

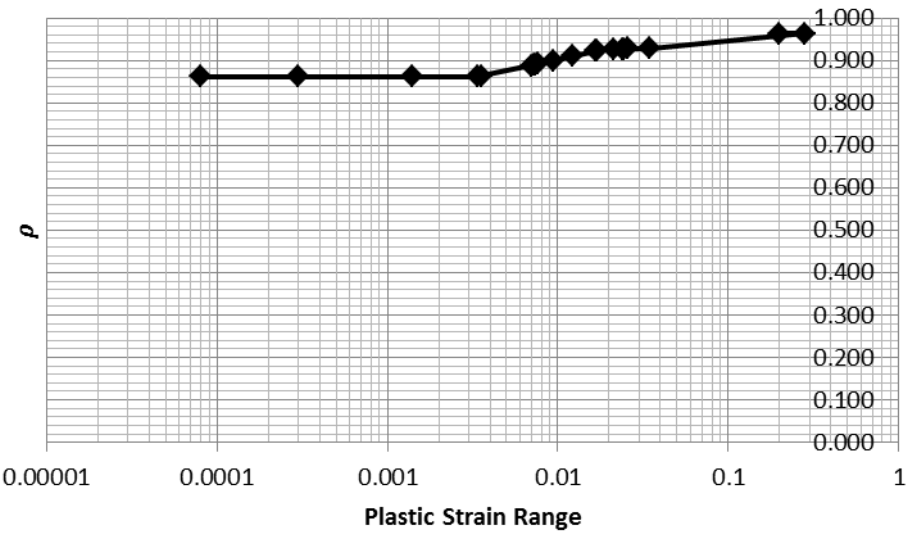

Figure 2.19: ρ as a function of plastic strain range.

Table 3 below includes values computed from Equations (2.37) and (2.39) for inelastic dissipation per reversal as well as damage per reversal, according to Equation (2.30). These data are plotted in Figure 2.20. These points represent data corresponding to a relationship of the form of Equation (2.32). The lack of fit provided by the power law indicates that a different modeling equation is required for data of this type. In the development that follows, various expressions, including some based on MaxEnt principals will be proposed to model the data plotted in Figure 2.20.

Table 2.3: Inelastic dissipation and damage.

k	2Nf	Range Mpa	Range Ep	1/n	rho	Wf/2Nf	D/2Nf
1	1	538	2.00E-01	26.7	0.964	1.04E+02	1.00E+00
2	1	558	2.80E-01	26.7	0.964	1.51E+02	1.00E+00
3	76	1007	3.45E-02	26.7	0.928	1.61E+01	1.32E-02
4	38	990	2.58E-02	26.7	0.928	1.19E+01	2.63E-02
5	124	986	2.46E-02	26.5	0.927	1.12E+01	8.06E-03
6	144	965	2.40E-02	26.4	0.927	1.07E+01	6.94E-03
7	190	952	2.13E-02	25.9	0.926	9.40E+00	5.26E-03
8	114	956	1.70E-02	25.1	0.923	7.50E+00	8.77E-03
9	440	934	1.66E-02	24.7	0.922	7.15E+00	2.27E-03
10	560	896	1.21E-02	21.2	0.910	4.94E+00	1.79E-03
11	920	874	9.44E-03	19.1	0.900	3.72E+00	1.09E-03
12	516	907	7.60E-03	17.6	0.893	3.08E+00	1.94E-03
13	1080	883	7.40E-03	17.4	0.891	2.91E+00	9.26E-04
14	800	883	7.20E-03	17.1	0.890	2.83E+00	1.25E-03
15	624	909	7.00E-03	16.9	0.888	2.83E+00	1.60E-03
16	2800	797	3.56E-03	13.6	0.863	1.22E+00	3.57E-04
17	1608	862	3.40E-03	13.4	0.862	1.26E+00	6.22E-04
18	5860	807	1.40E-03	13.4	0.862	4.87E-01	1.71E-04
19	16336	703	3.00E-04	13.4	0.862	9.09E-02	6.12E-05
20	23400	717	8.00E-05	13.4	0.862	2.47E-02	4.27E-05

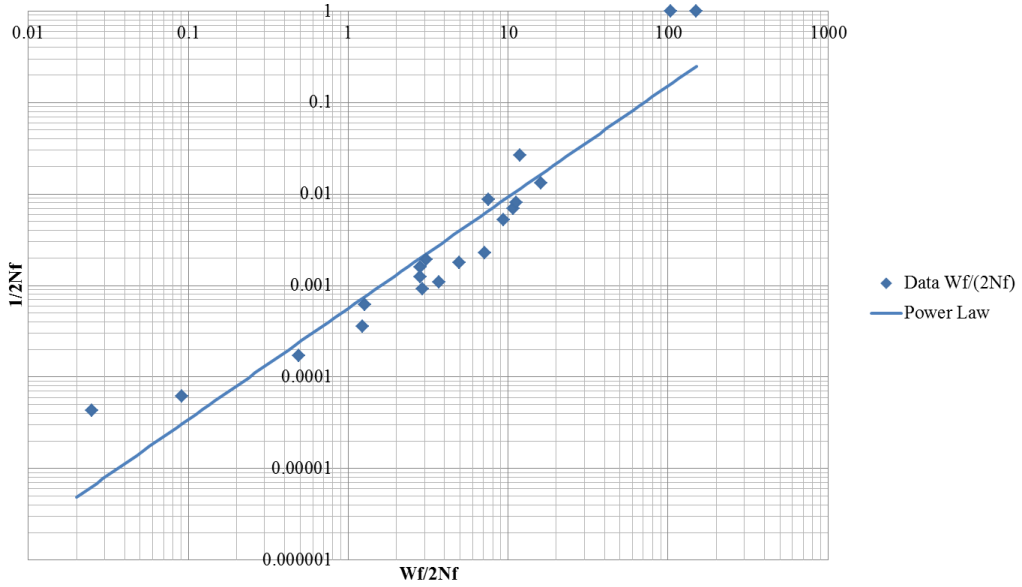

Figure 2.20: Damage per reversal as a function of inelastic dissipation per reversal with power law fit (R^2=0.89).

2.9.1 Discussion of Candidate Distribution Functions

Inelastic dissipation is a non-negative valued function so only distribution functions equal to zero for $x \geq 0$ are admissible candidates. Table 2.5 contains a summary of the fitted functions as well as the sum of squares of error remaining after the fitting. The natural logs of the data were fitted to the natural logs of the predicted values. Plots of the fitted curves and the data are in Figure 2.21. Only the truncated forms of the Normal distribution are considered. Distributions that are truncated on the right, such as the truncated exponential distribution have the additional advantage that they are strictly equal one for $x \geq a$.

The data set being fit has some noteworthy features. Even though the data is of low cycle fatigue, most of the samples still represent very small values of D_{rev}. Additionally, the data points show a concave-up trend that limits the quality of the fit achievable by a power law relationship. The fit was notably better for the right truncated exponential distribution with a negative λ. The fitting procedure converged to a negative λ, which corresponds to a rising exponential curve that becomes constant at $D_{cycle} = 1$. The best fits were achieved by the truncated Normal distribution and the truncated Exponential distribution. The Smith-Ferrante function (popular in Cohesive Zone Models of fracture) is typically used to represent the traction vs. separation and is founded on relationship binding material together at the microscopic scale [37]. Its integral is used here, which has the qualitative features of a damage function. The Weibull distribution function was also tried. Additionally, a power law expression having the form of the Coffin-Manson relation was tried. This function would be truncated at $D_{rev} = 1$.

Table 2.4: Candidate function forms fit to data in Table 2.4.

Function	*Form (for $0 \leq a$)*	*Sum of Sqr Error*
Left Truncated Normal	$D_{rev} = \frac{F_{norm}(W_c, \mu, \sigma) - F_{norm}(0, \mu, \sigma)}{1 - F_{norm}(0, \mu, \sigma)}$	5.17
Truncated Exponential	$D_{rev} = \frac{1 - \exp(-\lambda W_c)}{1 - \exp(-\lambda a)}$	6.66
Power law (Coffin-Manson form)	$D_{rev} = k(W_c)^{-\frac{1}{c}} \; for \; W_c \leq W_{c\,crit}$	14.8
Weibull	$D_{rev} = 1 - \exp(-k{W_c}^{\alpha})$	15.4
Smith-Ferrante form	$D_{rev} = 1 - (1 + kW_c)\exp(-kW_c)$	57.3

Note that the Coffin Manson expression typically relates plastic strain range to cycles to failure. In Table 2.4, it is shown in an inverted form and expressed in terms of $W_c = W_f/2N_f$. It is clear from the sum of squared error column in Table 2.4, and from Figure 2.21 below that the truncated Normal distribution provided the best fit to the data, followed by the truncated Exponential distribution. The (inverted) Coffin Manson expression and the Weibull distribution function provided the next best fit.

Parameters fit by numerical solver to the fatigue data for the truncated Normal distribution (Equation (2.41)) and the truncated Exponential distribution (Equation (2.42)) are given below:

$$D_{rev} = \frac{F_{norm}(x, 72.1, 27.3) - F_{norm}(0, 72.1, 27.3)}{1 - F_{norm}(0, 72.1, 27.3)} \quad for \; x \geq 0 \tag{2.41}$$

$$D_{rev} = \frac{1 - Exp(0.0325x)}{1 - Exp((-0.0325)(127.2))} \quad for \;\; 0 \leq x \leq 127.2 \tag{2.42}$$

The 95% confidence intervals on the parameters are as follows as computed by Matlab non-linear regression. For the truncated Normal distribution, $25.8 \leq \mu \leq 118.6$ and $5.75 \leq \sigma \leq 48$. For the truncated Exponential distribution, *a* was fixed at the mean of the two monotonic test values (127.2) and $-0.0354 \leq \lambda \leq -0.0293$. Although the trunated Normal distribution has the best fit, the truncated Exponential distribution has some desireable properties. If monotonic tension data points are available, they can be used to directly constrain the point where the curve

is strictly equal to 1.0. The parameter λ controls the shape of the curve between $x = 0$ and $x = a$. For λ close to zero, the curve is nearly a ramp function. For negative λ values, it has varying degrees of concave-up curvature. Examples of a family of such curves are plotted in Figure 22. In the present case, $\lambda = -0.0323$ giving a strongly rising curve. A damage function of the mathematical form of Equation (2.42) exists in the literature [23]. The authors of [23] present Equation (2.43) as an improvement to the Coffin-Manson relationship (Equation (2.2)) for modeling LCF in the sub 100 cycle range (ϵ_{pa} is the plastic strain amplitude). The relationship is presented as an empirical improvement and is not derived from physical principles. The authors don't describe it as a truncated Exponential distribution function. It is clear that Equation (2.43) can be rearranged to a form similar to Equation (2.42).

$$D_{cycle} = \frac{Exp\left(\frac{\lambda \epsilon_{pa}}{\epsilon_f}\right) - 1}{Exp(\lambda) - 1} \tag{2.43}$$

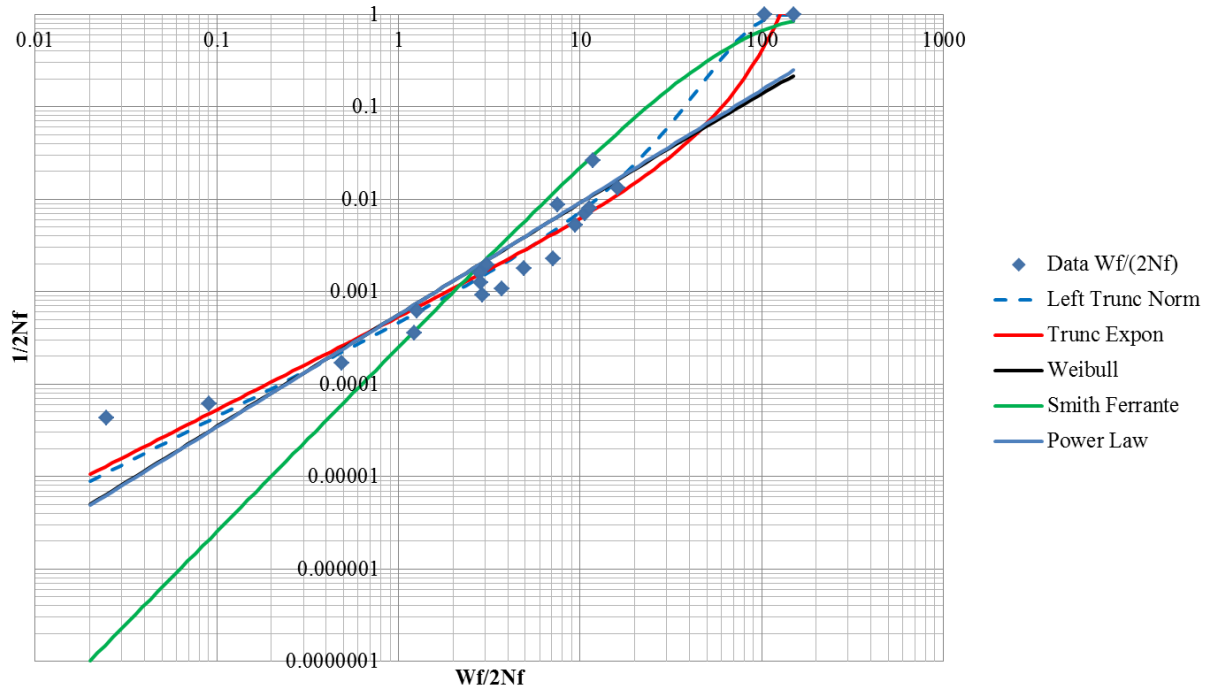

Figure 2.21: Plots of functions in Table 2.5.

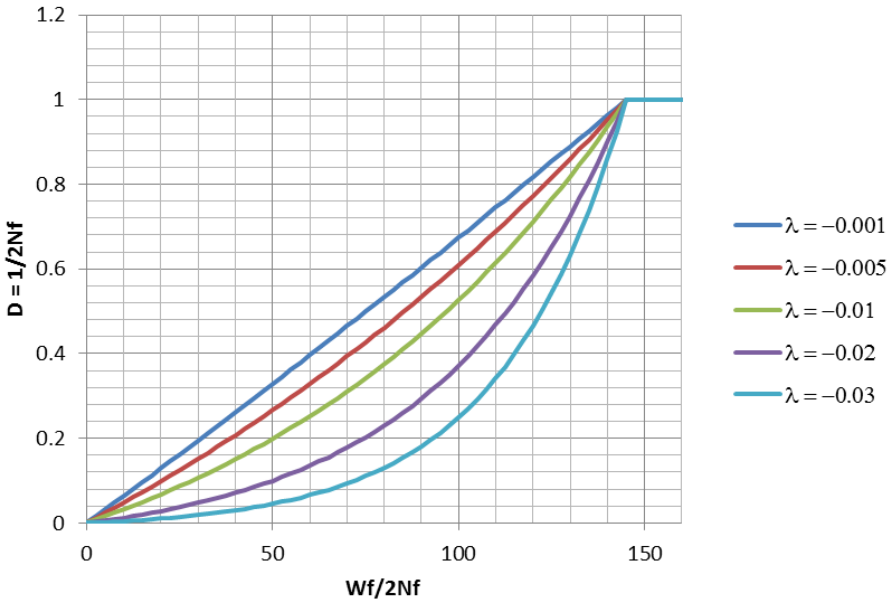

Figure 2.22: Plots of truncated Exponential distribution with different shapes.

2.10 Conclusions

In this study, the Maximum Entropy principle was shown to provide a systematic theoretical and philosophical basis for selecting a CDF to model damage. The method was demonstrated on a LCF data set for Aluminum 2024-T351. In general, the proposed approach is applicable to broader class of materials undergoing fatigue damage. We showed that several maximum entropy distributions, including the truncated exponential and the truncated normal distribution are good choices for material damage modeling. Compared to the exponential distribution, the truncated exponential distribution has additional flexibility and can model concave-up data. In the limit, it can approximate a uniform distribution. For the Aluminum 2024-T351 alloy, the truncated normal distribution was shown to provide the best fit to the data relative to the more common alternatives of Coffin-Manson equation or the Weibull distribution. Left-truncation of the normal distribution extends its applicability to the many applications where data is non-negative. Finally, a Coffin Manson function in terms of plastic strain (the standard form) was compared to the truncated Normal distribution and shown to provide an inferior fit.

CHAPTER 3. LOW CYCLE FATIGUE AS A STOCHASTIC PROCESS

3.1 Introduction

Consider a fixed amplitude axial fatigue test of a defect-free crystalline metal where plastic strain is occurring during each cycle. Certain features of this type of test are well known. The number of cycles to failure at a given strain level exhibits considerable scatter ([3], [38], [39]) while the trend in life vs. applied plastic strain amplitude frequently follows the Coffin-Manson power law (Equation (3.1)) where the constant c is typically between -0.8 and -0.5 [3]. As is the case with any data that exhibit scatter, the cycles to failure can thus be interpreted as a random variable, in this case whose distribution is dependent on the applied strain amplitude as a parameter. Additionally, the location the failure crack initiates is a spatial random variable over the gauge region of the specimen. Note that this is not the case with alloys, such as cast aluminum, that contain defects where fatigue cracks tend to initiate. In the case of these materials, the position of pre-existing flaws is random, but they represent a relatively small number of locations where a crack might begin. Thus, crack ignition location is not spatially Poisson. The following argument is limited, as stated above, to defect free materials, which will tend to exclude most ordinary cast metals.

Specimen designs provide uniform (as much as possible) stress states in the gauge region, while the random orientation of the individual grains in the metal result in grain-scale inhomogeneities that make some grains more likely to initiate cracks than others. Although the general sequence of processes leading to failure has been studied (and is reviewed below), there is no generally agreed upon explanation for the form of Equation (3.1) and it is usually referred to as an empirical law [3].

$$\epsilon_p = kN^c \tag{3.1}$$

Most predictive equations used in mechanics could be regarded as deterministic. Given known arguments, the equations evaluate to specific values. In reliability engineering, equations that model the distribution in component lives represent exceptions to this rule. While the mean life (or some quantile of life) can be written as explicit functions of parameters that may depend on stress factors or component parameters, it is understood that the relationship being modeled is essentially random in nature. The researcher seeks to describe the randomness in terms of an appropriate reference probability distribution. The distributions of lives of complex systems can be deduced from the failure distributions of their components. In these cases, statistics is the appropriate framework to describe the behavior of interest. Some researchers, starting with [38] have argued that a fatigue test, and by extension fatigue of engineered components in service, can be described by stochastic processes. Describing the scatter in fatigue data at some constant cyclic stress or strain condition with a probability distribution is routine [6]. However, these authors show how certain simple (and experimentally supported) assumptions about the underlying random processes explain widely observed trends in fatigue data. Their successes suggest that the mathematics of stochastic processes provide the appropriate environment to describe the fatigue process.

3.2 The Poisson Process

There are many random processes in physics that may be modeled as Poisson processes. Examples include the times of various events, such as radioactive decay, collisions in an ideal gas, or even the incidence of near-Earth asteroids. The defining feature of a Poisson process is that the expected time (or distance) to the next event is independent of the time elapsed since the previous event—the process is thus 'memoryless'. The distribution is characterized by a single parameter λ which corresponds to the expected number of events in some reference interval of time or region of space. The Poisson Probability Mass Function (PMF) is given below in Equation (3.2) [21].

$$P(N = r) = \frac{e^{-\lambda}\lambda^{r}}{r!}, \quad r = 0, 1, 2, \ldots \tag{3.2}$$

Also of interest is the probability of observing at least one event which is given in Equation (3.3) or at least 2 events, which is given by Equation (3.4).

$$P(N \geq 1) = 1 - e^{-\lambda} \tag{3.3}$$

$$P(N \geq 2) = 1 - e^{-\lambda}(1 + \lambda) \tag{3.4}$$

Additionally, Poisson's theorem states that a discrete time process consisting of a sequence of many low probability Bernoulli trials converges to a Poisson process [21]. Following [38], we argue that fatigue is such a process, where fatigue cycles correspond to Bernoulli trials. It can be shown that for a large number *n* of Bernoulli trials with probability *p,* the resulting Poisson λ is given by Equation (3.5) [21]. In the case of a fixed amplitude fatigue test, *n* corresponds to the number of cycles and p is the probability of failure on a given cycle. It is clear that the very small *p* and large *n* that would apply to a fatigue test satisfies Poisson's theorem.

$$\lambda = np \tag{3.5}$$

3.3 Literature Review

Several of the prior works that will be reviewed treat fatigue failure as the result of a Poisson process. In [39], the authors argue that crack formation can be treated as the result of statistically independent processes occurring on the surface of a component undergoing fatigue at each cycle. Particularly, they argue that formation of cracks during a particular cycle can be modeled as a Poisson point process, the parameters of which change from cycle to cycle. The assumption that the Poisson parameters change during the fatigue test distinguishes [39] from the other works that will be reviewed. The authors of [39] propose that the probability that there is at least one crack at cycle n is given by Equation (3.6), with the parameter λ at this point an unknown function of cycle count and inelastic dissipation range.

$$P(N \geq 1) = 1 - e^{-\lambda(n,\epsilon)} \tag{3.6}$$

The Coffin-Manson Basquin equation (Equation (3.7)) is interpreted as an experimentally observed fact, not a consequence of the proposed statistical model of fatigue. It is presented as defining an implicit functional dependency of N_{idet} on strain amplitude ϵ. Here N_{idet} represents the deterministic cycle count corresponding to a plastic strain amplitude.

$$\epsilon = \frac{\sigma'_f}{E}(2N_{idet})^b + \epsilon'_f(2N_{idet})^c \tag{3.7}$$

Finally, the form of Equation (3.6) is assumed to be Weibull, by specifying the appropriate form for $\lambda(n, \epsilon)$, although the authors note that any other suitable probability function could be used. The value N_{idet} is used as the Weibull scale parameter. Although the cycles to failure at a particular plastic strain amplitude is modeled as a random variable, the functional relationship between average life and plastic strain is deterministic. This reference may be regarded as presenting a hybrid approach that includes features of both stochastic and deterministic paradigms of fatigue failure.

The following references draw more exclusively from statistical arguments. The arguments in [38] and [28] provide the starting point for the present work. The argument in [38], and by extension our argument, is based on the statistical trends in the formation of grain-scale cracks (mesocracks). It is widely reported that persistent slip bands that form in single or polycrystalline metals during cyclic loading are the source of cracks that develop into a dominant failure-causing crack ([40], [41], and [42]). When a sample of metal is subjected to cyclic loading of magnitudes with plastic strain amplitudes greater that about 0.0001, a particular sequence of events typically occurs. Initially, a period of cyclic hardening occurs, due to stacking of defects. This takes typically less than 10% of the eventual fatigue life. During this stage, the stress amplitude rapidly rises with increasing N at a fixed strain amplitude ([7]). Once the stress amplitude stabilizes (saturates), persistent slip bands (PSBs) begin to form. The population of PSBs grows rapidly and approximately linearly early in the life of the fatigue specimen. By 10% to 25% of specimen life, the PSBs represent an essentially constant fraction of the volume of the specimen ([38], [42]). The author of [41] proposes that the fraction of the specimen occupied by PSBs is proportional to the plastic strain range and this result is used in [38]. Under low cycle fatigue (LCF) conditions, no macroscopic crack typically forms until the final 10% of life [38]. Recall that in LCF applied loads cause general yielding of the specimen

cross section and any macroscopic cracks will grow rapidly. During the mid-portion of life, grain-scale surface cracks randomly form in the PSB population. The formation of the PSBs themselves is treated as a deterministic process, where their density is proportional to the applied plastic strain range, following [41]. Since the density of PSBs scale with plastic strain range, the rate of formation of grain-scale cracks will also. These cracks lie in the planes of the PSBs and once initiating on the surface, propagate through the body of the grain. In [38], it is pointed out that in order for a crack to grow between two grains, the PSBs in neighboring grains must lie in similarly oriented planes. On the basis of these observations, it is argued in [38] that during the middle portion of fatigue life, where a stable fraction of the metal is occupied with PSBs, the crack forming process may be modeled as a Poisson process. This is a Poisson process in cycles (time) and also over the surface of the gauge region of the specimen (space). Given that the number of PSBs is constant after the initial portion of fatigue life, the authors assume that the probability that any given PSB could form a crack on a given strain cycle is a constant. Furthermore, the probability that any given formed crack will propagate to a neighboring grain and beyond is also constant. This model predicts that the population of grain level cracks should grow linearly with N and the authors provide experimental evidence of this (Figure 2 in [38]). Since the density of PSBs is proportional to the plastic strain range, the probability of neighboring grains having cracks is also proportional to plastic strain range. Finally, since both rates scale with plastic strain range, the authors conclude that the time (cycles) to formation of a propagating crack should scale as the inverse of plastic strain range squared. Thus, they conclude that statistical considerations suggest a Coffin-Manson exponent of -1/2 (Equation (3.5)). Since the total life is assumed to be simply 125% of the propagating crack nucleation life, the same power law exponent will apply. In [43], the arguments in [38] are extended to stress-controlled high cycle fatigue (HCF). The authors explain the transition from LCF to HCF exponents in the Coffin-Manson and Basquin laws as resulting from competition between two different failure processes—surface (LCF) vs. bulk (HCF) crack propagation. Our present interest is in the LCF domain. In the work that follows we build on the Poisson process model developed by the authors of [38] and propose a statistical framework for describing LCF life prediction models. We adopt the position that cracking can be modeled as a Poisson process, but do not assume that the crack density is strictly proportional to the applied plastic strain range. Thus, we can account for the fact that the Coffin-Manson exponent is not always equal to -1/2.

$$\epsilon_p = kN^c \quad c = -\frac{1}{2} \tag{3.8}$$

Another example of statistical reasoning applied to the fatigue life relationship is provided by [28]. Rather than viewing fatigue cycles as a stochastic sampling process, the authors in [28] focus on the thermodynamic state of the material under test. Instead of load cycles, the statistical variable is the entropy of the material (represented by inelastic dissipation) totaled over all applied cycles. A statistical distribution is used to model the probability of material failure occurring by the time the observed level of entropy has been accumulated. The statistical distribution itself is unknown, and difficult to measure. Rather than assuming a reference distribution as is common in many applications, the authors use the maximum entropy method of [22] to derive one. The authors derive the maximum entropy distribution corresponding to the case of a single expected value constraint, given in Equation (3.8):

$$E[\psi(x_i)] = \sum_i p_i \psi(x_i) \quad : x_i \in \{x_1, x_2, \dots x_i \dots x_m\} \tag{3.9}$$

The solution to problem is the distribution:

$$p_i = p_0 \exp\left(-\frac{\psi(t_i)}{k_\psi}\right) \tag{3.10}$$

The failure of the material at a point is the final state due to an irreversible process. Thermodynamic entropy is a measure of irreversibility. In order to be used to predict failure, entropy must be measureable. In [28] the authors use the Clausius-Duhem Inequality, together with the Helmholtz Free Energy to derive the following expression for the rate of entropy production during plastic deformation of a *J2* type solid. If the temperature is essentially constant during a plastic strain process, then entropy production rate is proportional to inelastic dissipation rate $\dot{W}_t$.

$$\dot{\psi} = \frac{1}{\rho T}\left(\dot{W}_t\right) \geq 0 \tag{3.11}$$

Substituting Equation (3.11) into Equation (3.10) and integrating from zero to *t* leads to the damage parameter $D(t)$ defined in Equation (3.12). A value of $D(t) = 1$ represents failure with a probability of 1. The value $D = 0.95$ is used for application of Equation (3.12). This is used to solve for a value of total accumulated inelastic dissipation that corresponds to failure.

$$D = 1 - \exp\left(-\frac{W_t}{\rho T k_\psi}\right) \tag{3.12}$$

The damage parameter *D* represents the state of the material on the continuum from zero (virgin) to one (failed) and is also a statistical cumulative distribution function (a CDF). This connection is useful in that it brings many results from statistics to bear on a class of damage parameters.

Equation (3.12) gives a fixed value of inelastic dissipation at failure, once *D* is specified. For the elastic-perfectly plastic material model used in [28], this implies that the product of cycles to failure and plastic strain are constant.

$$W_t \propto N\epsilon_p \tag{3.13}$$

Equation (3.13) can be written in the form of a Coffin-Manson relationship (Equation (3.14)) with an exponent of -1. This value of exponent is characteristic of materials of the type studied in [28], and differs from the Coffin-Manson exponent values typically seen in structural metals, which are typically between -.5 and -.8.

$$\epsilon_p = kN^c \quad c = -1 \tag{3.14}$$

The exponent of value of -1 is a consequence of the fact that total inelastic dissipation to failure is a material constant for the alloys studied in [28]. It is known that this quantity is not a constant for most structural metals [2] and thus cannot be directly used to build predictive strain

amplitude vs. life relationships for these other classes of materials. However, it is possible to extend the probabilistic argument in [28] to the case of materials where failure is not strictly predicted by total inelastic dissipation.

3.4 Stochastic Model of Low Cycle Fatigue

We are concerned here with the low cycle fatigue domain where plastic strain, which causes inelastic dissipation, is present to a measurable degree. Further we stipulate that we are concerned with the cycle range to failure of about 1,000 to 20,000. At the very low cycle range, the population of PSBs may not reach a steady state and the statistical sampling argument given here may not apply. Although inelastic dissipation is occurring, for most engineering materials under a low cycle fatigue test, plastic strain will be on the order of 0.001 to 0.05. Thus, movement is occurring in the structure of the metal, but not gross distortion. The macroscopic mechanics of the specimen remain essentially constant for the duration of the test. It is an interesting and surprising fact that the macroscopic properties of the specimen usually do not change substantially during the test. Specifically, any significant increase in compliance of the specimen due to the presence of large cracks is generally limited to the last few percent of life. This means that there is difficulty, generally, to distinguish a specimen that is 20% of the way through its expected life from one that is 80% of the way though its expected life. In the Continuum Damage mechanics literature, the damage variable D is defined as 0 for virgin material and 1 for failed material. When applied to fatigue tests it is common to define the value of D, at some intermediate point in a fatigue test, as the fraction of expected life consumed. Thus the damage per cycle corresponding to a given loading level is the inverse of the expected life. This definition can be regarded as a statement of the Palmgren-Miner rule. However, it is important to note that in most cases, no macroscopic evolution of damage is apparent in the sample for most of the test. The classical definition of D as fraction of initial specimen rigidity remaining is not successful for tests of this type. At stress levels sufficient to cause plastic deformation, which by definition stresses exceed the yield strength of the material, any crack of significant size would rapidly grow and cause failure. As pointed out in [2], only microscopic widely distributed damage is occurring. Eventual initiation of a propagating crack can be attributed to a random event, the result of a ‘successful’ trial occurring on that particular fatigue strain cycle.

Following [38], we recognize that the initial and final portions of the fatigue process are not consistent with a stochastic process model. The initial portion of life includes hardening and stacking of defects, before PSBs begin to form. The final portion of life is consumed with the growth of a propagating crack. In the discussions that follow, the cycles n corresponds to the middle portion of life where damage occurrence is modeled as a stochastic process. Cycle $n = 1$ corresponds to the first cycle where damage is occurring, and *failure* is defined as the initiation of a propagating crack. The authors of [28] argued that the total inelastic dissipation to failure was a random quantity that could be used as the basis for a statistical model of low cycle fatigue. Here, we adopt their use of inelastic dissipation as an appropriate predictor of fatigue failure, but place it in a stochastic process model after [38]. This viewpoint allows greater flexibility in the life vs. inelastic dissipation amplitude relationship.

The development that follows proceeds in two steps. In the first, we consider the case where a single failure event, as modeled by a Poisson process, is sufficient to initiate a crack that will become a propagating crack. In the second step, we consider that possibility that two, or possibly m failure events are required to create a propagating crack. It will be seen that the Poisson process model is easily extended to this case. Recall that in [38] it was argued that favorably oriented cracks in adjacent grains must form in order for a propagating crack to occur. The development of the model proceeds as follows. The material is in either of two possible states: intact or failed. If it is intact, it has survived the fatigue test up to the previous cycle. The critical inelastic dissipation range is taken to be a continuous random variable, with a given parametric distribution, defined on the interval of 0 to infinity. At each load cycle, inelastic processes cause the state of the material to change and a new value of the critical inelastic dissipation is sampled. If the new sampled value exceeds that value applied during the test, the material fails. Thus, there is a probability of failure with each cycle. Figure 3.1 below provides an illustrative example of this process. The red line represents a strain-controlled load history that applies a given inelastic dissipation per cycle. The blue diamonds represent random samples from the distribution of the specimen's critical fatigue strength value at that cycle number. The graph shows failure at cycle 34, where the sampled critical inelastic dissipation value was less than that the applied inelastic dissipation range.

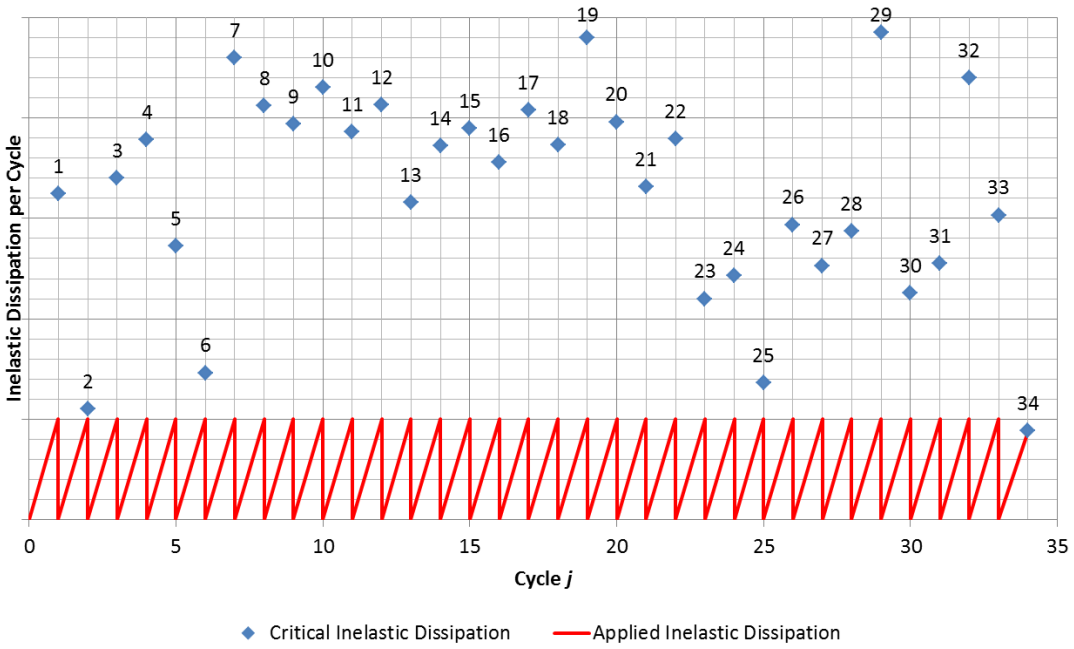

Figure 3.1: Example of stochastic process model of fatigue.

Since a strain-controlled fatigue test could potentially last for hundreds or thousands of cycles, the vast majority of the sampled strength values must be well above the applied load value. Predicting the median life vs. the applied load is a statistical calculation that is carried out below.

Propositions

1. Inelastic process that occur in the material at each cycle cause random microstructural changes in the material.
2. The statistical properties of the material are essentially constant for the middle 80% of the duration of the fatigue test.
3. The material fails on a given cycle if and only if the inelastic range applied to the material exceeds the cycle-by-cycle critical inelastic dissipation.
4. The cycle-by-cycle critical inelastic dissipation can be modeled as a random variable that is independently sampled at each cycle

Thus, the failure event represents the result of a stochastic process occurring cycle-by-cycle in the structure of the metal. This point of view is used to develop a relationship of the form of Equation (3.12) suitable for structural metals. Additionally, it will be shown that the Coffin-

Manson relationship, as well as the Palmgren-Miner linear damage law, can both be deduced within this framework.

Table 3.1: Definitions of variables in stochastic process model.

W_j	Inelastic dissipation range applied to specimen on the j^{th} cycle.
$\widehat{W}_j$	*Critical value* of the inelastic dissipation range that would cause failure on the present cycle
$F(\widehat{W}_j, \bar{\alpha})$	Cumulative distribution function (CDF) of the critical inelastic dissipation range. Each cycle represents a sample from this distribution. The parameter vector $\bar{\alpha}$ is fixed for a given specimen.
p_j	Probability of failure on the j^{th} cycle
$P(n)$	Probability of failure on *or before* the n^{th} cycle
P_{crit}	The level of overall probability of failure taken to represent expected failure. $P_{crit} = 0.5$ would represent a median estimate.

Probability that the applied inelastic dissipation range W_j exceeds the critical $\widehat{W}_j$ for the material specimen on the j^{th} cycle:

$$p_j = P(\widehat{W}_j \leq W_j) = F(W_j, \bar{\alpha}) \tag{3.15}$$

If the probability of a failure occurring on a given trial is p, and is the same for all trials, the probability of failure occurring by n trials is given by Equation (3.16). This is the probability of at least one event in n samples from a binomial distribution.

$$P(n) = 1 - (1 - p)^n \tag{3.16}$$

Equation (3.16) can be shown to rapidly converge to an exponential form. This is the form of the waiting time to the first event in a Poisson process. For a fixed $P(n) = 0.5$, this approximation is within 1% of Equation (3.12) for $n \geq 24$.

$$1 - (1 - p)^n \underset{n\to\infty}{\longrightarrow} 1 - e^{-np} \tag{3.17}$$

The W_j are all the same in the case of constant amplitude tests and combining Equations (3.15) and (3.16) gives Equation (3.18). Note that Equation (3.18) has the form of the smallest of n

order statistic for the random variable described by F. The probability of failure by the n^{th} cycle can be equated to a reference probability. P_{crit} = 0.5 would give a median estimate.

$$P(W_j, n) = 1 - \left(1 - F(W_j, \bar{\alpha})\right)^n = P_{crit} \tag{3.18}$$

Equation (3.18) defines an implicit relationship between W_j and n. For some cases of the chosen distribution function $F(W_j, \bar{\alpha})$, such as the example that follows below, Equation (3.18) may simplify to a convenient form. In general, it may be solved for n as given below in Equation (3.19). Note that Equation (3.19) can be written as a ratio of cumulative hazard functions for the random variable described by $F(W_j, \bar{\alpha})$.

$$n = \frac{\ln(1 - P_{crit})}{\ln\left(1 - F(W_j, \bar{\alpha})\right)} = \frac{H(P_{crit}, \bar{\alpha})}{H(W_j, \bar{\alpha})} \tag{3.19}$$

Cumulative hazard function:

$$1 - F(W_j, \bar{\alpha}) = e^{-H(W_j, \bar{\alpha})} \tag{3.20}$$

Next, note that Equation (3.17) can be used to simplify Equation (3.18). A Poisson approximation form of Equation (3.18) results.

$$P(\Delta\epsilon_p, n) \approx 1 - e^{-nF(\Delta\epsilon_p, \bar{\alpha})} = P_{crit} \tag{3.21}$$

Setting P_{crit} = 0.5 and solving for the inverse of n gives the desired representation of damage per cycle as cumulative distribution function. Recall that this argument requires that n be reasonably large.

$$\frac{1}{n} = D_j = \frac{F(W_j, \bar{\alpha})}{\ln(2)} \tag{3.22}$$

Thus if damage per cycle if defined as the inverse of median life *n*, it is equal to the sampling distribution function for the applied inelastic dissipation value of the material times a constant. Equation (3.22) could also have been derived from Equation (3.19) since for small values of $F(x)$, which we necessarily have in this case, $F(x) \approx H(x)$.

If we assume that the critical plastic strain sampling distribution is Weibull from Equation (3.11) [21]:

$$F(W_j) = 1 - e^{-kW_j{}^{\alpha}} \tag{3.23}$$

The resulting overall probability (Equation (3.18)) becomes:

$$P(n, W_j) = 1 - e^{-knW_j{}^{\alpha}} = P_{crit} \tag{3.24}$$

For a fixed value of P_{crit}, Equation (3.24) requires that the quantity in the exponent be a constant. The form of the Coffin-Manson relationship is immediately obtained and is given below in Equation (3.25). In this case the life is modeled by inelastic dissipation per cycle rather than plastic strain, but for plasticity models such as elastic, perfectly plastic, the equation would be the same within a constant. The classical Coffin-Manson exponent value of -1/2 corresponds to a Weibull exponent of 2 (Rayleigh).

$$W_j = Cn^{-\frac{1}{\alpha}} \tag{3.25}$$

Assuming that the failure distribution is *exponential* gives $nW_j = \text{const.}$, or fixed total inelastic dissipation, similar to the result in [28]. This is a consequence of the fact that the first order statistic for an exponential distribution is also exponential, so whether we model the probability of failure with the total inelastic dissipation (as in [28]) or cycle-by-cycle, the mathematical form is the same.

Equation (3.18) can be extended to a variable amplitude loading history:

$$P(n) = 1 - \prod_{j=1}^{n} \left(1 - F\left(W_j,\, \bar{\alpha}\right)\right) = P_{crit} \tag{3.26}$$

Rewriting as a sum of log terms:

$$\sum_{j=1}^{n} \ln\left(1 - F\left(W_j,\, \bar{\alpha}\right)\right) = \ln(1 - P_{crit}) \tag{3.27}$$

$$\sum_{j=1}^{n} \frac{\ln\left(1 - F\left(W_j,\, \bar{\alpha}\right)\right)}{\ln(1 - P_{crit})} = \sum_{j=1}^{n} D_j = 1 \tag{3.28}$$

Equation (3.27) can be written as a sequence of terms that sum to 1 (Equation (3.28)). Comparison to Equation (3.22) shows that these terms represent the damage (inverse of n_j) corresponding to that W_j. Thus, this framework implies linear damage accumulation.

The model as presently constructed assumes a single Poisson event is sufficient to cause failure (crack initiation). This implies that the distribution in crack initiation cycles is modeled by Equation (3.21)—the waiting time to an event in a Poisson process. Alternatively we could

follow [38] and specify that 2 events are required to cause failure. In this case, we replace Equation (3.27) with Equation (3.4), yielding Equation (3.29).

$$1 - e^{-nF(W_j,\bar{\alpha})}\left(1 + nF\left(W_j, \bar{\alpha}\right)\right) = P_{crit} \tag{3.29}$$

Note the form of Equation (3.29) is still $fcn\left[nF\left(W_j, \bar{\alpha}\right)\right] = P_{crit}$ and thus $nF\left(W_j, \bar{\alpha}\right) = Const.$ and a form analogous to Equation (3.22) can be obtained (Equation (3.30)). The constant K_{crit} would need to be solved for to satisfy Equation (3.29).

$$\frac{1}{n} = D_j = K_{crit}F\left(W_j, \bar{\alpha}\right) \tag{3.30}$$

If we consider a particular fixed load amplitude $F\left(W_j, \bar{\alpha}\right) = Const.$ and Equation (3.29) can be interpreted as the CDF of cycles to failure, i.e., it models the sampling distribution of specimen life n at a given constant inelastic dissipation test condition. Since we hold the inelastic dissipation range fixed, the form of $F\left(W_j, \bar{\alpha}\right)$ does not affect the distribution in cycle life for a constant amplitude test and the results that follow are consequences of the underlying Poisson process. This CDF is given in Equation (3.31) below. It shows that for the 2 failure case, the distribution of cycles to failure would be Erlang with an exponent of 2 (Equation (3.32)).

$$1 - e^{-np_j}\left(1 + np_j\right) = P(n) = F_n(n) \tag{3.31}$$

$$f(n) = np_j{}^2e^{-np_j} \tag{3.32}$$

The Weibull and Lognormal distributions are both frequently used to model the scatter of fatigue data. The Erlang distribution has substantially the same left skewed shape. Figure 3.2 below shows 2 samples of 25 data points. The set labeled ‘Erlang’ is synthetically generated data from an Erlang distribution with an exponent of 2. The set labeled ‘Weibull’ is synthetically

generated Weibull data. The plots show the result of plotting both data sets on a Weibull probability plot. It is clear that the fit is comparable, even with a generous sample size of 25. This result suggests that the Erlang distribution may be a good candidate to model the spread in low cycle fatigue data.

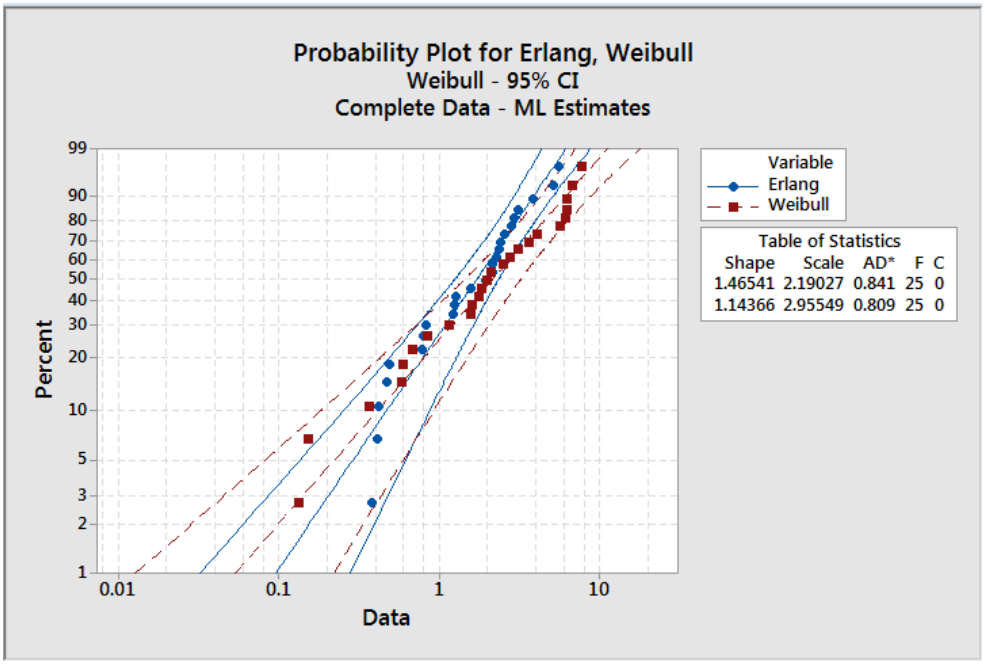

Figure 3.2: Comparison of Weibull plots of Weibull and Erlang synthetic data.

Just as Equation (3.4) gives the probability of at least 2 Poisson events, it can be shown that Equation (3.33) gives the probability of at least m events. Again we have $nF(W_j, \bar{\alpha}) = Const.$ for a specified value of P_{crit}. Equation (3.33) is also an Erlang CDF at a fixed test condition where the m is equal to the number of events required for failure. As m increases, the distribution converges to a Normal distribution. Examples of 3 Erlang probability density functions are plotted below in Figure 3.3.

$$F_n(n) = 1 - e^{-np_j} \sum_{k=0}^{m-1} \frac{(np_j)^k}{k!} \tag{3.33}$$

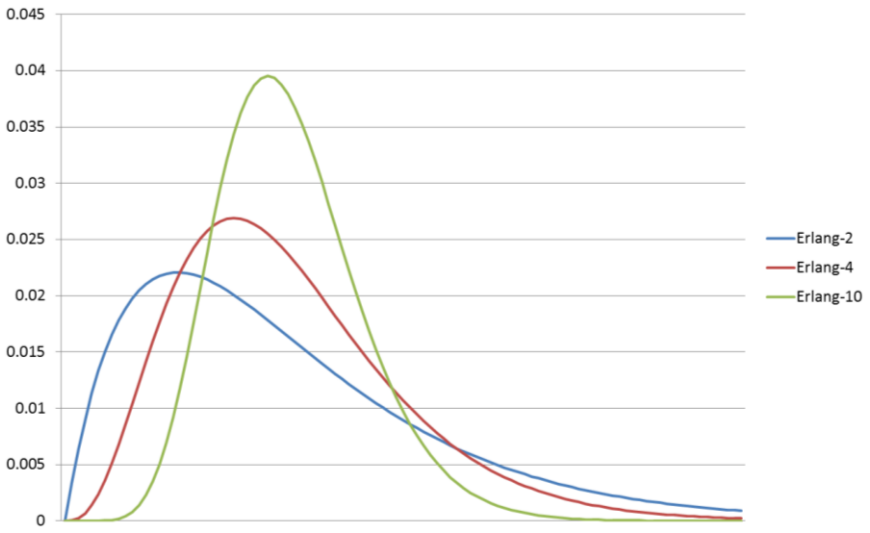

Figure 3.3: Erlang distributions corresponding to 2, 4 and 10 Poisson events, same mean.

3.5 Conclusions

Reference [38] argues that the crack formation process in a low cycle fatigue test may be modeled as a Poisson process, where the probability of a crack initiating is constant during the middle 80% of specimen life. This reference (also [42]) indicates that the number of PSBs stabilizes after forming early in the specimen life. This reference contains data to show that the population of microcracks grows linearly as predicted by the Poisson process model. Here, we propose that that the probability of a crack initiating on a particular cycle is determined by a reference CDF of the material's critical inelastic dissipation range sampling distribution. The parameter of inelastic dissipation was chosen following [28], where it is argued that inelastic dissipation, a surrogate for material entropy, is more fundamentally connected to the irreversible process of damage. Initially, we assume a simple process where a single Poisson event is sufficient to cause failure. By choosing a probability of sample failure, and implicit relationship between inelastic dissipation range and cycles is obtained. We show that the life vs. inelastic dissipation range relationship assumes the familiar power law form if the material's critical plastic strain range distribution is taken to be Weibull. Additionally, it has been shown that for a test consisting of sequence of different amplitude cycle blocks, this model predicts linear damage accumulation. Next, we extend the argument to the case where 2 Poisson events are required to cause a failure. It is shown that this condition results in cycles to failure being Erlang distributed

(with and exponent of 2). This distribution has the left-skewed shape expected in fatigue data. This result generalizes to m events, with the resulting failure distribution being Erlang with an exponent of the m.

Finally, it has been shown that, consistent with a key result in [28], regardless of the number of Poisson events required, the appropriate damage parameter is equal to the critical plastic strain range distribution function (times a constant). This follows from the widely used fatigue definition of damage per cycle as the inverse of cycles to failure.

CHAPTER 4. TRACKING FATIGUE DAMAGE WITH A HIGER-ORDER CONTSTITUTIVE RELATIONSHIP USING TENSION-COMPRESSION ASYMMETRY

4.1 Introduction

It is desirable to be able to measure the progress of high-cycle fatigue damage in a specimen under test. The present work develops a new approach to the tension vs. compression asymmetry measure of damage known in the Continuum Damage Mechanics literature. This measurement is applied to specimens under high cycle fatigue axial test conditions. The existing method of measuring the slopes of the tension vs. compression sides of the stress strain curve, while intuitively reasonable, is based on a simplistic conceptual model of the behavior of a cracked body. A model based on a general, non-linear elastic formulation is proposed. Although similar elastic models exist in the literature, these have thus far only been applied to acoustic measurement of damage, not stress-strain of the type typically gathered during a servo-hydraulic axial fatigue test. Most existing works do not connect the parameters of the quadratic material model to damage *D*, and none were found that connected *D* to the asymmetry of the compression vs tension sides of the curve. We propose an explicit formula for *D* based on a non-linear elastic model fitted to stress-strain data.

4.2 Background

In Continuum Damage Mechanics [20], many small cracks are hypothesized to exist in the damaged area of the material. Unlike the Fracture Mechanics approach, there is no attempt to model the geometries and positions of particular cracks. Rather the behavior of the cracked material is modeled by adjusting its virgin bulk properties. The degree of material damage represented by these cracks is inferred from the macroscopic properties of the specimen. In [20], Lemaitre builds a general framework for modeling damage from various mechanical sources, including plastic deformation, creep, and low and high cycle fatigue. In his development, Lemaitre posits a distributed, isotropic, collection of small cracks that reduce the local effective load bearing cross section of the material from S to $\tilde{S}$. Here damage is modeled by D, which

ranges from 0 (virgin material) to 1 (failed, separated). The dependency of $\tilde{S}$ on D is given by Equation (4.1):

$$\tilde{S} = S(1 - D) \tag{4.1}$$

One relation that follows is Equation (4.2):

$$D = 1 - \frac{\tilde{E}}{E} \tag{4.2}$$

Where $\tilde{E}$ is the modulus of the damaged material and E is the modulus of the virgin material. Other relations for strength and strain are also developed. The cracks are assumed to be small enough and sufficiently evenly distributed such that the properties of the material vary smoothly in the neighborhood of the damaged area. Although this approach lacks direct evidence of the existence of a specific crack (or cracks) of known size and position, such as is available in fracture mechanics, it does seek to provide a mathematically detailed model, within the framework of continuum mechanics, that explains the experimentally observed behavior of damaged material. The author's work in [20] includes not only the mathematical model of damage, but also a set of experimental and data analysis techniques that attempt to reveal the state of damage of a given specimen at a particular point in an experiment. The author also shows that, in cases where the specimen is taken to the point of separation, a real crack was present and evidence of its growth is visible in striations and beach marks on the fracture surface. Many other experimental definitions of D have been proposed by various authors. All include the features that D should be a strictly increasing function of damage that starts at a value of zero for undamaged material. In [44], Ye and his colleagues list various possible definitions of D and demonstrate different approaches to defining and measuring damage that follow the general idea of loss of load bearing area as defined in [20] (Table 4.1 below). This table references the ratio N/N_f which is the fraction of total life consumed after N cycles.

Table 4.1: Damage variables proposed in [44].

Damage Definition		Cyclic Fraction N/N_f				
		0.0	0.215	0.538	0.897	0.999
Static toughness	$D_N = 1 - \frac{U_{TN}}{U_{T0}}$	0.0	0.043	0.118	0.404	0.950
Ductility	$D_N = 1 - \frac{\ln(1/(1-\varphi_N))}{\ln(1/(1-\varphi_0))}$	0.0	0.035	0.083	0.234	0.590
Elastic Modulus	$D_N = 1 - \frac{E_N}{E_0}$	0.0	0.038	0.077	0.147	0.203
Residual Strength	$D_N = 1 - \frac{\sigma_N}{\sigma_0}$	0.0	0.0	0.0	0.012	0.51
Strain Response	$D_N = 1 - \frac{\Delta\epsilon_N}{\Delta\epsilon_0}$	0.0	0.0	0.043	0.064	0.186

4.3 Tension-Compression Asymmetry

In [20], Lemaitre presents a special version of the modulus method to evaluate D that makes use of the difference between modulus in tension and compression. He argues that cracks would be expected to open in tension, but will close to some extent in compression. For the effective area S, the damaged area in tension is defined by the damage variable D, in the usual way (Equation (4.3)).

$$\tilde{S}_{tens} = S(1 - D) \tag{4.3}$$

In compression, the damage is scaled by a factor h, that varies between 0 (cracks close completely) and 1 (no crack closure), as shown in Equation (4.4). The value of 0.2 is suggested absent experimental data.

$$\tilde{S}_{comp} = S(1 - Dh) \tag{4.4}$$

$$\tilde{E}_{tens} = E(1 - D) \quad \tilde{E}_{comp} = E(1 - Dh)$$

Additionally, the following formula is given to determine h, from experimentally measured moduli in tension and compression [20].

$$h = \frac{1 - \frac{\tilde{E}_{comp}}{E}}{1 - \frac{\tilde{E}_{tens}}{E}} \tag{4.5}$$

Applications of tension-compression asymmetry are found in [45]. Figure 4.1, shows an asymmetric stress-strain loop and the influence of h. Note that these authors chose to set h = 1.0 in the tension direction, which is slightly different from Equation (4.9) but does not contradict it.

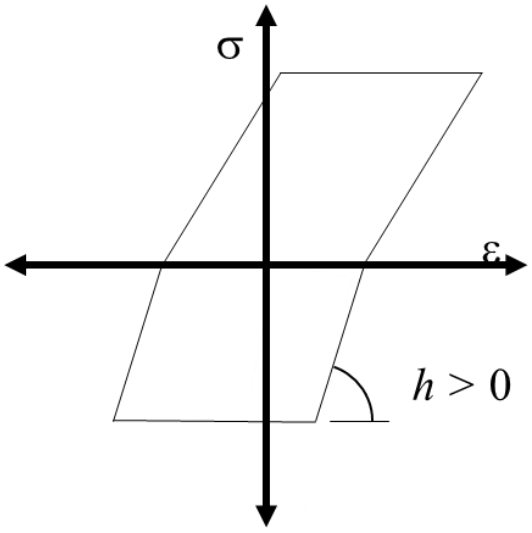

Figure 4.1: Schematic Representation of Effect of h on Shape of a Stress-Strain Loop.

The authors of [45] were concerned with developing an analytical model of damage as part of a finite element code.

In [18], Schweizer, *et. al.*, the authors apply the compliance method of damage measurement to a corner-cracked shaft under LCF conditions. The authors show the evolution of the nearly elastic stress-strain curve (Figure 4.2) as a function of N. The asymmetry of the tension vs. compression sides of the curve is plainly visible. This reference clearly shows that a noticeable difference can be observed between then tension and compression sides portions of a stress vs.

strain loop as a function of progress of fatigue damage. However, this work was concerned with a single dominant fatigue crack, not the diffuse damage posited in [20].

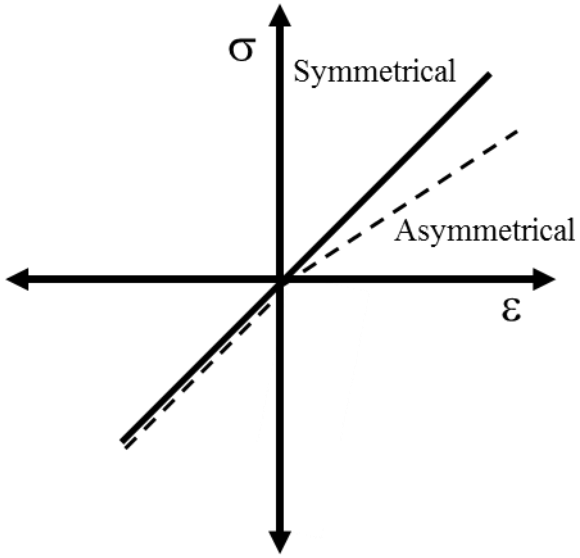

Figure 4.2: Asymmetrical Stress Strain Curve from a Fatigue Specimen.

4.4 Ultrasonic Inspection Applications

In the next several references, the authors used nonlinear material models, quadratic in strain, to model the acoustic elastic response of material that is posited to contain damage in the form of small cracks. The cracks are assumed to cause the material to be stiffer in compression than in tension, consistent with Equation (4.4). Thus, tension versus compression asymmetry is modeled by a parabolic curve rather than a pair of line segments. In all but one case, the authors stop at characterizing the second degree term in the stress-response, and do not compute a value for *D* corresponding to the measured nonlinearity.

In [46], the authors were concerned with developing a non-destructive method to measure the degree of damage in granite used in civil engineering applications. Granite specimen were subjected to varying levels of compressive stresses in the form of a load applied once and then removed. The applied loads were 20% to 80% of the mean compressive strength of the material. An ultrasonic, non-destructive inspection was then undertaken to measure the degree of damage in the specimens. The inspection method was based on a non-linear elastic model of the material. The degree of non-linearity, as measured by the ultrasonic inspection, was claimed to be a

strictly increasing function of damage in the form of small diffuse cracks of the type posited in [20]. Undamaged material was assumed to behave linearly, whereas any measurable nonlinearity was claimed to indicate damage. The non-linear material model (in one dimension) begins with Equation (4.6). This stress-strain law is claimed to be based on the work presented in [47], which will be discussed below.

$$\sigma = E(\epsilon + \beta\epsilon^2 + \delta\epsilon^3 + \cdots) \tag{4.6}$$

The authors then claim that the magnitude of the coefficient on the second-degree term in Equation (4.6) is proportional to the ratio of the first and second harmonics found during the ultrasonic inspection. They define β' which is proportional to $|\beta|$ and defined in Equation (4.7). Data is then presented to show that the parameter β' is a more sensitive indicator of material damage than some other potential responses such as ultrasonic wave velocity or dynamic modulus.

$$\beta' = \frac{A_{second}}{A_{first}} \tag{4.7}$$

Unlike the other authors who studied ultrasonic response as a damage indicator, these authors propose a damage measure based on the rationale that *D* should start at zero and converge to 1 as *β'* increases, defined as follows:

$$D = 1 - e^{\beta'_0 - \beta'_i} \tag{4.8}$$

Expanding Equation (4.8) indicates that D is not linear in *β'*. Note that *β'* is a magnitude and is thus non-negative.

$$D = \beta'_i - \beta'_0 - \frac{1}{2}(\beta'_0 - \beta'_i)^2 - \cdots \tag{4.9}$$

This measure of D is not conceptually connected to the compliance-based definition in [20].

Another application of Equation (4.3) is found in [48]. Li, *et. al.*, show how the ultrasonic VHCF method can be used to monitor the tension vs. compression modulus symmetry of the sample during the test. In this method, a tension specimen is mounted in a fixture that enables an ultrasonic axial excitation to be applied—in this case at 20,000Hz. A schematic of their test fixture is shown below in Figure 4.3. This method allows many millions of cycles to be applied per day and is popular in the field of gigacycle (VHCF) fatigue.

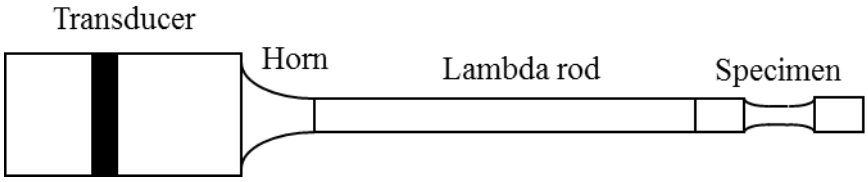

Figure 4.3: Ultrasonic fatigue test fixture from [48].

The loads applied to the specimen would be expected to be well below the level where plastic yielding is observed, yet the behavior of the initially linear system becomes subtly non-linear as the test progresses. The cause of the non-linearity is claimed to be the stiffness asymmetry of crack opening and closing [48]. The nonlinearity of the system is captured by a nonlinear stress-strain relationship Equation (4.10).

$$\sigma = E\epsilon(1 + \beta\epsilon) \tag{4.10}$$

The authors in [2], derive a relationship of similar form to Equation (4.3) by considering the elastic energy function as a power series of the strain tensor. They argue that including the linear and the first non-linear term is sufficient to model wave propagation in a class of nonlinear materials. The work in [48] follows this pattern. Equation (4.10) is used as an assumed stress-strain relationship in an one dimensional wave equation.

Here, β is a nonlinearity parameter that is equal to zero for the linear case. The nonlinearity parameter is measured by the feedback system built into the test fixture and is seen to follow an increasing trend during the test (see Figure 4.4 below). Additionally, the resonant frequency (a function of the stiffness of the sample) is seen to drop during the course of the test, consistent with the hypothesis of CDM [20]. The point 'A' in Figure 4.4 is claimed to identify the point at which crack initiates [48].

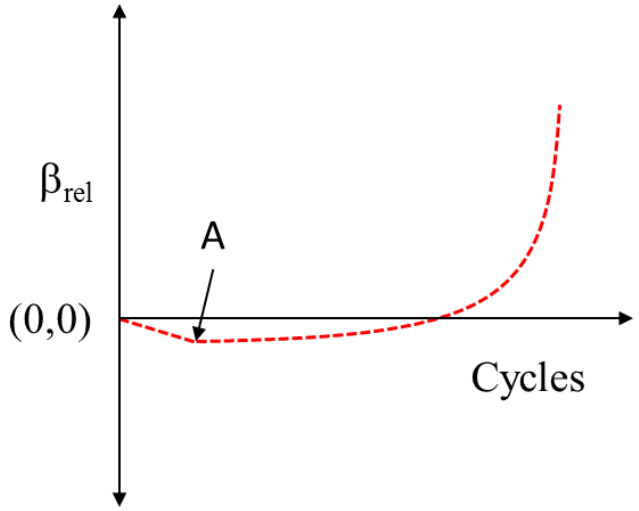

Figure 4.4: Change in elastic response of a fatigue specimen under test, from [48].

It is important to note that in [48] [49], there is no explicit mention of D as a function of the non-linearity parameter β. It is simply shown that an increase in β has a generally monotonically increasing relationship to fatigue damage which is hypothesized to be a consequence of many small cracks in the metal of the specimen. However, their approach is consistent with a main idea of damage mechanics, where a material with small scale distributed cracking is modeled using a continuum approach that accounts for spatially averaged degraded material properties. In our work, we will derive a relationship of a similar form to Equation (4.10), but apply it to stress-strain data collected during a servo-hydraulic high-cycle fatigue test. Furthermore, we will obtain an expression for D as a function of the calculated non-linearity.

Other authors employing quadratic one-dimensional stress-strain laws include [50], [51], and [52]. These researchers were also concerned with measuring damage by analyzing ultrasonic

response. The relationships given in [46] and [50] are one-dimensional relationships based on an equation given in [47]. The authors of [47] present a general framework, where elastic strain energy is represented as a power series of the strain tensor. They present equations to describe wave propagation in a material where the terms up to the first non-linear terms are included. One result they provide is the elastic strain energy as a function of the strain tensor (Equation (4.11)) up to the terms cubic in strain, where G is the shear modulus and κ is the bulk modulus, and A, B and C are higher order constants.

$$U = G{\epsilon_{ik}}^2 + \left(\frac{1}{2}\kappa - \frac{1}{3}G\right){\epsilon_{ll}}^2 + \frac{1}{3}A\epsilon_{ik}\epsilon_{il}\epsilon_{kl} + B{\epsilon_{ik}}^2\epsilon_{ll} + \frac{1}{3}C{\epsilon_{ll}}^3 \tag{4.11}$$

4.5 Stiffness of a Cracked Body

Although the author of [20] does not specifically associate a crack size with a measured stiffness (considering asymmetry or not), he does derive a relationship that shows the dependence of D_i (the damage contribution from a particular crack) on crack size a_i based on continuum damage mechanics arguments. This relationship is given below in Equation (4.12). He also derives an expression for D_i based on a fracture mechanics argument using the strain energy in a cracked body (Equation (4.13)). This second approach predicts a cubic dependence on crack size. His development proceeds using the form in Equation (4.12).

$$D_i \propto {a_i}^2 \tag{4.12}$$

$$D_i \propto {a_i}^3 \tag{4.13}$$

Sayers, *et. al.*, [53] compared several continuum mechanics approaches for modeling the elastic properties of a body with many distributed small cracks. All of the methods converge to the form of Equation (4.13) for small crack densities and then diverge as crack densities become large enough to allow elastic interaction between the cracks. This result is also consistent with the idea that an embedded crack of a given size results in a given volume of material, in the shadow of the crack, that would bear less load due to the presence of the crack. The affected volume would scale with the cube of the crack dimension.

4.6 Derivation of 4th Order Stress-Strain Law and Reduction of Quadratic Form

Equation (4.10) was derived by considering a general power series relationship between stress and strain and truncating it after the first non-linear term. The results were used in [48] [49] to develop a method to acoustically monitor the progress of damage in the specimen. In the present work we proceed by deriving the stress-strain relationship for a one-dimensional non-linearly elastic body and use the result to provide a damage function that explicitly depends on the measured non-linearity of the material.

We begin by assuming a homogeneous deformation without rotation. The deformation gradient is as follows, expressed in terms of stretches along principle directions.

(4.14)

$$\bar{\bar{F}} = \begin{bmatrix} \lambda_x & 0 & 0 \\ 0 & \lambda_y & 0 \\ 0 & 0 & \lambda_z \end{bmatrix}$$

Note that for the case of homogenous deformation, engineering strains have a simple and exact relationship to the stretches in Equation (4.14) [54], and are also the experimentally observed variables in many applications. The deformation gradient for homogenous deformation in terms of the principal stretches expressed as engineering strain is:

(4.15)

$$\bar{\bar{F}} = \begin{bmatrix} \epsilon_x + 1 & 0 & 0 \\ 0 & \epsilon_y + 1 & 0 \\ 0 & 0 & \epsilon_z + 1 \end{bmatrix}$$

Now consider the case of uniaxial loading along the *x* axis. For Poisson's ratio defined for an infinitesimal change in *x*, *y*, *z*:

$$\frac{dy}{y} = \frac{dz}{z} = -\nu\frac{dx}{x} \tag{4.16}$$

Integrating from l_{0i} to $l(t)_i$ yields Equation (4.17). This can be interpreted as expressing the effect of Poisson's ration in terms of logarithmic strain.

$$\ln(\epsilon_y + 1) = \ln(\epsilon_z + 1) = -\nu \ln(\epsilon_x + 1) \tag{4.17}$$

Equation (4.18) is an expansion of Equation (4.17) accurate to the second order. The first order term can be recognized as the usual linear dependency on Poisson's ratio:

$$\epsilon_y = \epsilon_z = -\nu\epsilon_x + \left(\frac{\nu^2}{2} + \frac{\nu}{2}\right)\epsilon_x{}^2 \tag{4.18}$$

The Left Cauchy-Green tensor corresponding to Equation (4.15) and Equation (4.18) is:

$$\bar{\bar{B}} = \bar{\bar{F}}.\bar{\bar{F}}^T \tag{4.19}$$

$$\bar{\bar{B}} = \begin{bmatrix} (\epsilon_x + 1)^2 & 0 & 0 \\ 0 & \left(1 - \nu\epsilon_x + \left(\frac{\nu^2}{2} + \frac{\nu}{2}\right)\epsilon_x{}^2\right)^2 & 0 \\ 0 & 0 & \left(1 - \nu\epsilon_x + \left(\frac{\nu^2}{2} + \frac{\nu}{2}\right)\epsilon_x{}^2\right)^2 \end{bmatrix}$$

The stress-strain law for an isotropic elastic material is given by Equation (4.20) (from [54]). The α_j's are material constants.

$$\bar{\bar{\sigma}} = \left(\alpha_0 + \alpha_1 \mathrm{Trace}(\bar{\bar{B}})\right)\bar{\bar{I}} + \alpha_2 \bar{\bar{B}} + \alpha_3 \left(\bar{\bar{B}} - \bar{\bar{I}}\right)^2 \tag{4.20}$$

The σ_x term of the expansion of Equation (4.20) is as follows:

$$\sigma_x = A_4(\alpha_1, \alpha_3){\epsilon_x}^4 + A_3(\alpha_1, \alpha_3){\epsilon_x}^3 + A_2(\alpha_1, \alpha_2, \alpha_3){\epsilon_x}^2 + A_1(\alpha_1, \alpha_2)\epsilon_x + \alpha_0 + 3\alpha_1 + \alpha_2 \tag{4.21}$$

Where, the A_i coefficient is a linear combination of the listed α_j's. We force the curve to intersect the origin, and choose to eliminate the parameter α_2:

$$\alpha_2 = -\alpha_0 - 3\alpha_1 \tag{4.22}$$

We solve the linear system and find that $A_4 = A_3$. It can be shown that Equation (4.20) can be expressed in terms of the parameters in Equation (4.23):

$$\sigma_x = (\epsilon_x + 1)A_3{\epsilon_x}^3 + A_2{\epsilon_x}^2 + A_1\epsilon_x \tag{4.23}$$

Equation (4.23) can be compared to Equation (4.6), which has the form of a general, continuing power series. Equation (4.23), based on a general elastic material model (Equation (4.20)), is at most a fourth degree equation, subject to the strong constraint that the third and fourth degree terms have the same coefficient. In applications were strains are much smaller than unity, this allows us to immediately neglect the fourth degree term. Noting that $\epsilon_x < 0.004$ for the present case, we argue that both the 3rd and 4th degree terms may be neglected for our purposes. The working form of stress-strain law is given below:

$$\sigma_x = A_2{\epsilon_x}^2 + A_1\epsilon_x \tag{4.24}$$

This equation has the same form as Equation (4.10), however it was derived not by considering an arbitrary power series in strain, but rather by beginning with a general law for an elastic solid (Equation(4.20)). Additionally, we have shown that even under more general conditions, the three-parameter Equation (4.23) is sufficient.

We introduce a dependency on cycle *N* for the parameters in Equation (4.24).

$$\sigma_{xN} = A_{2N}{\epsilon_x}^2 + A_{1N}\epsilon_x \tag{4.25}$$

An illustrative example of Equation (4.25) is shown below in Figure 4.5. Note that for actual data, the quadratic stress-strain curve has the visual appearance of a straight line.

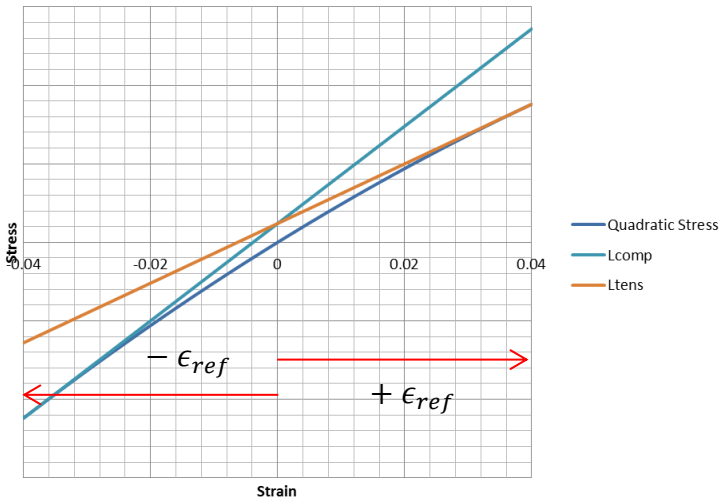

Figure 4.5: Quadratic stress-strain curve and lines tangent to curve at $\pm\epsilon_{ref}$.

Let $\pm\epsilon_{ref}$ be a strain range that captures the range of the strain data (Figure 4.5). This value is kept fixed for all analysis at a given load level. Lines tangent to the plot of Equation (4.25) (Figure 4.5) will have a slope defined by Equation (4.26) evaluated at $\pm\epsilon_{ref}$.

$$f'(\epsilon_x) = 2A_{2N}\epsilon_x + A_{1N} \tag{4.26}$$

It is assumed that this analysis method applies to fully-reversed, load-controlled or strain-controlled test data. For an expression of the form of Equation (4.25), the tangent lines can be

shown to intersect on the stress axis for any pair of lines tangent at $\pm\epsilon_{ref}$ and thus are consistent with a bi-linear model for values of strain close to $\pm\epsilon_{ref}$.

Earlier, Equation (4.2) was written in terms of elastic modulus. We rewrite it in terms of the stress reached at a given strain level in Equation (4.27)

$$D = 1 - \frac{\frac{\sigma_D}{\epsilon_{ref}}}{\frac{\sigma_0}{\epsilon_{ref}}} \tag{4.27}$$

If we assume that small cracks are present that open under tension, resulting in a reduced measured stiffness of the component, but close in compression, acting like undamaged material, Equation (4.27) may be restated as Equation (4.28) [20]:

$$D = 1 - \frac{\frac{\sigma_{tens}}{\epsilon_{tens}}}{\frac{\sigma_{comp}}{\epsilon_{comp}}} = 1 - \frac{\sigma_{tens}}{|\sigma_{comp}|} \quad for\ \epsilon_{tens} = -\epsilon_{comp} \tag{4.28}$$

As is pointed out in [20], the cracks may not close completely in compression, and thus $|\sigma_{comp}| < |\sigma_0|$. The crack closure parameter *h* is introduced to capture this effect [20].

$$\sigma_{tens} = \sigma_0(1 - D) \tag{4.29}$$

$$\sigma_{comp} = \sigma_0(1 - Dh)$$

Combining Equations (4.28) and (4.29) yields Equation (4.30)

$$D = 1 - \frac{\sigma_{tens}}{\sigma_{comp}}(1 - Dh) \;\; for\; 1 > h\; f(partial\; crack\; closure) \tag{4.30}$$

In this work, the values of damage D_N of interest are ≤ 0.1, since sample separation typically occurs at values of D less than this. In the derivation below, it is assumed that h = 0, however non-zero h results in the same form for Equation (4.28) in the small damage approximation, with h absorbed into the remaining constants.

Equation (4.28) is effective at comparing the tension vs. compression slopes of a material that has a linear response in tension and a linear response with a possibly different slope in compression. For our present purposes, we require an equation that is applicable to a curve of a more general shape. Thus, we argue that Equation (4.31) represents the appropriate generalization of Equation (4.28).

$$D_N = 1 - \frac{\left.\frac{d\sigma_{xN}}{d\epsilon_x}\right|_{\epsilon_x=\epsilon_{ref}}}{\left.\frac{d\sigma_{xN}}{d\epsilon_x}\right|_{\epsilon_x=-\epsilon_{ref}}} \tag{4.31}$$

Thus from Equation (4.26):

$$D_N = 1 - \frac{A_{1N} + 2A_{2N}\epsilon_{ref}}{A_{1N} - 2A_{2N}\epsilon_{ref}} \tag{4.32}$$

We now define β_N as:

$$\beta_N = \frac{A_{2N}}{A_{1N}} \quad \beta_N < 0 \tag{4.33}$$

Rewriting Equation (4.32) and noting that for small values, it may be linearized, we get:

$$D_N = 1 - \frac{1 + 2\beta_N \epsilon_{ref}}{1 - 2\beta_N \epsilon_{ref}} \approx -4\beta_N \epsilon_{ref} \tag{4.34}$$

Although the arguments presented so far suggest that all observed non-linearity is due to damage, it was found that even new specimens have measureable non-linearity. The data to demonstrate this effect will be presented in a later section. Note that this non-linearity is very slight and would not be noticed unless carefully looked for. This is due to a feature of aluminum alloys that is noted by previous authors. In [55] it is stated that for aluminum alloys, the modulus in compression is typically about 2% greater than that in tension. This could be interpreted as indicating existing damage, possibly due to microcracks or voids in the material, or alternatively as a consequence of the actually subtly non-linear behavior of real materials. This D_0 initial nonlinearity could be subtracked off if appropriate to the situation. We finally note that the form of D is that of the ratio of the quadratic to the linear terms in Equation (4.25).

$$-4\beta_N \epsilon_{ref} \propto \left| \frac{A_{2N} {\epsilon_{ref}}^2}{A_{1N} \epsilon_{ref}} \right| \tag{4.34}$$

4.7 Data Collection and Analysis

Figure 4.6: HCF specimen, 25.4mm x 7.6mm gage, AS7GU cast aluminum.

A high-cycle fatigue axial test program was undertaken to demonstrate the proposed method. The specimens were fabricated from the cast aluminum alloy AS7GU-T64. This alloy was developed for demanding applications such as automotive engine components. A review of this alloy can be found in [56] with a discussion of the effect of its microstructure on its fatigue

behavior found in [1]. Both load and strain data was collected at intervals during the entire test. In addition to the maximum and minimum loads and strains reached at each cycle, a full tension/compression cycle 'loop' was collected every 100 cycles and consisted of about 160 data points sampled at approximately constant intervals of load and includes both load increasing and decreasing portions of the cycle. Data was collected in the form of strain vs. load for these load controlled tests. To fit modeling equations in terms of life vs. stress, load must be converted into stress. Since the damage values of interest are very small and minute differences between specimen stiffness in tension and compression are being analyzed, it is necessary to take the step of converting the load to true stress. The measured diameter of the specimens and the slight non-linearity due to Poisson's ratio dilation and contraction of the cross section of the specimen are both accounted for.

Area of the cross section:

$$A = \pi r^2 = \pi r_0^2 (1 + u_{rr})^2 \approx \pi r_0^2 \left(1 - 2\,\nu u_{i,N} + (2\nu^2 + \nu) {u_{i,N}}^2\right) \tag{4.35}$$

The resulting axial true stress:

$$\sigma_{i,N} = \frac{P}{A} = \frac{P_{i,N}}{\pi r_0^2 \left(1 - 2\,\nu \epsilon_{i,N} + (2\nu^2 + \nu) {\epsilon_{i,N}}^2\right)} \tag{4.36}$$

It can be shown that the linear term provides sufficeint accuracy leading to:

$$\sigma_{i,N} = \frac{P_{i,N}}{\pi r_0^2 \left(1 - 2\,\nu \epsilon_{i,N}\right)} \tag{4.37}$$

Table 4.2: Summary of Relationships used in Data Reduction.

$\{P_{i,N}, \epsilon_{i,N}\}$	Load vs. strain data for i^{th} data sample in N^{th} loop.
$\sigma_{i,N} = f(P_{i,N}, \epsilon_{i,N})$	Stress value σ_x for i^{th} data sample in N^{th} loop, computed from corresponding load and strain values according to Equation (4.37).
$\{\sigma_{i,N}, \epsilon_{i,N}\}$ $i: 1,2, \dots n$	Data set used for model fitting at the N^{th} loop.
$\sigma_{xN} = A_{2N}{\epsilon_x}^2 + A_{1N}\epsilon_x$	Quadratic stress-strain law resulting from least squares fit to the N^{th} loop (Equation (4.25))
$D_N = -4\beta_N\epsilon_{ref}$	Damage computed for the N^{th} loop (Equation (4.34))

For each loop N, values for A_{2N} and A_{1N} were computed by the least squares method and a value of D_N corresponding to the N^{th} loop was computed according to Equation (4.34).

A summary of the observed specimen lives is provided in Table 4.3. The stress was computed to be 170MPa for these fully-reversed tests. Failure was defined as the last 100 cycle block completed before separation. The empirical Cumulative Distribution Function for this data is plotted in Figure 4.7. While the range in failure times is substantial, it is not unexpected in the field of high-cycle fatigue, especially considering that these data represent 11 tests at the same condition. Note that several specimens failed outside the gage area of the sample and their results are not reported

Table 4.3: Fully-reversed 170MPa, specimen lives.

Number	N_f
Spec-1	15,200
Spec-2	234,800
Spec-3	66,500
Spec-4	29,900
Spec-5	159,500
Spec-6	212,500
Spec-7	115,400
Spec-8	86,000
Spec-9	128,200
Spec-10	16,100
Spec-11	38,400

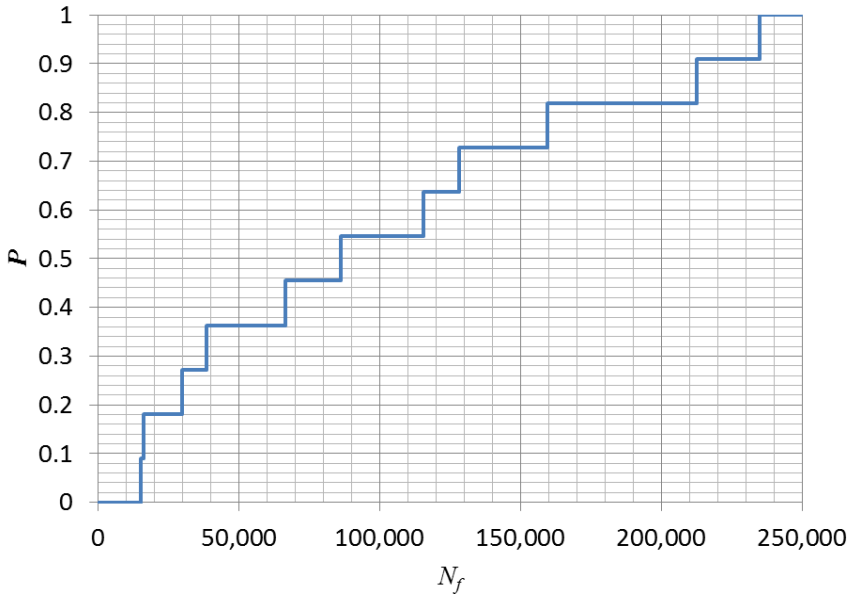

Figure 4.7: Empirical cumulative distribution function of data in Table 4.3.

For the loop analysis procedure and the application of Equations (4.25) and (4.34), the mean of the strain data, which was typically close to zero, was shifted to zero. The non-zero mean value was due to slight yielding that occurred at the beginning of the test. The reference strain value ϵ_{ref} was set at 0.0023 based on the observed range of strain during the tests. This value was held constant for all analysis.

We begin with a detailed discussion of Specimen 11, which we present as a typical example that captures trends present in these data sets. The evolution of D_N (computed from Equation (4.34)) is plotted below in Figure 4.8. This plot contains several noteworthy features. First, the computed damage is seen to clearly increase, at an accelerating rate, starting at approximately N/N_f = 0.4. However, as noted above, it is not found to begin at zero, and actually decreases slightly from values seen at the beginning of the test.

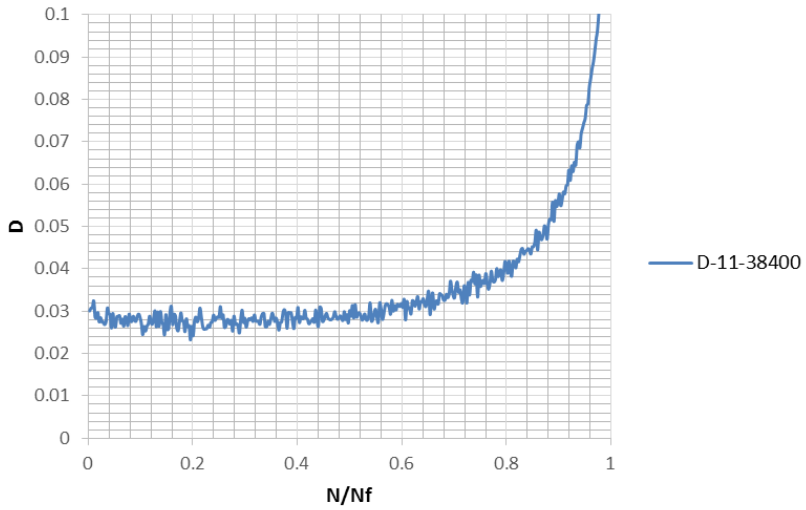

Figure 4.8: Damage evolution for Specimen 11. N_f = 38,400.

It is informative to look at the evolution of the nonlinear term $A_{2N}\epsilon_{ref}{}^2$ and the linear term $A_{1N}\epsilon_{ref}$ computed from the least squares fits to the loops. A plot of the magnitudes of these values for Specimen 11 is given in Figure 4.9 below. Both linear and nonlinear terms evolve over the course of the fatigue test. Since the linear term is in the denominator of Equation (4.34), its decrease in value causes an increase in D_N just as an increase in the nonlinear term does. Note that although both terms correlate with increasing damage, the nonlinear term increases by a factor of seven while the inverse of the linear term increases by less than 10%. The form of Equation (4.34), as a ratio of these values, combines the effects of their trends in an effective way.

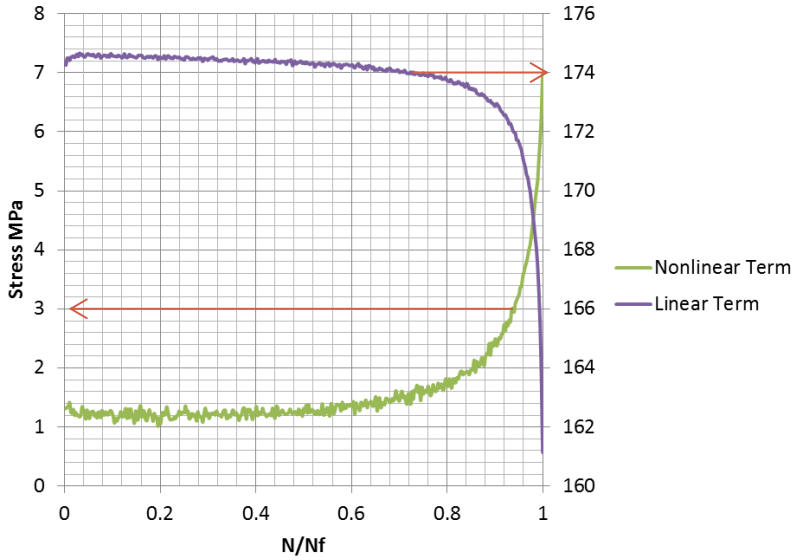

Figure 4.9: Comparison of evolution of linear and nonlinear terms in Equation (4.25) (Specimen 11).

As is the case with all specimens, the stress-strain loops resemble straight lines and neither plasticity nor nonlinearity is visibly apparent. Plots of stress-strain loops for N = 100 and N = 38,000 (N_f = 38,400) are shown in Figures 4.10 and 4.11. Note that the plots appear visually linear although a quadratic fit to the data shows the substantial increase in the magnitude of the coefficient on the quadratic term and a moderate decrease in the coefficient on the linear term.

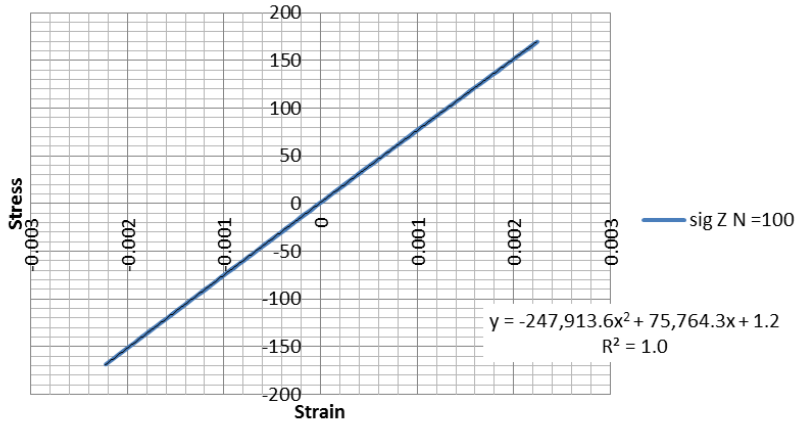

Figure 4.10: Specimen 11 loop at N = 100 cycles.

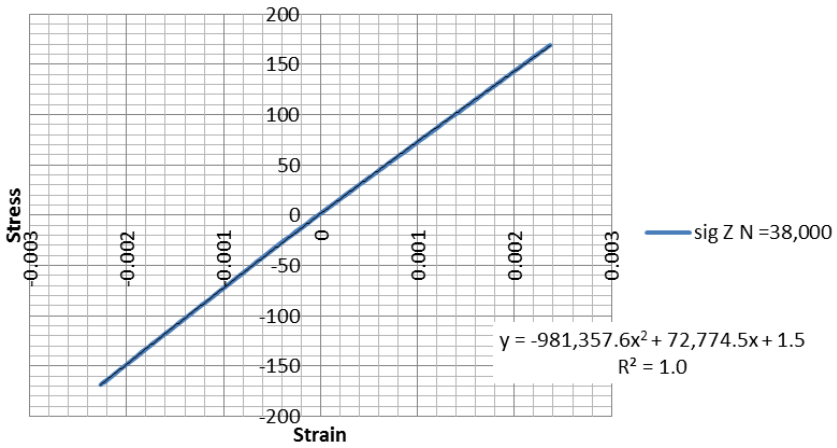

Figure 4.11: Specimen 11 loop at N = 38,000 cycles.

In order to visualize the nonlinearity in these curves, special data sets were constructed, where the linear portion of the response was subtracted off, leaving only the second degree term. This nonlinear quantity is shown in Equation (4.38).

$$\sigma_{nlN} = \sigma_{xN} - A_{1N}\epsilon_x = A_{2N}{\epsilon_x}^2 \tag{4.38}$$

Plots of Equation (4.38) for Specimen 11 are shown in the figures below. Note that there is a small vertical offset to this data which has no effect on the value of the second degree term found from least squares. Figure 4.12 shows the nonlinear portion of the loop at N = 100 cycles. The curvature that is visible in the data is seen to be modeled with reasonable fidelity with a parabolic curve. Note that the tension and compression portions of the loop cycle are slightly separated, indicating a small degree of plastic yielding.

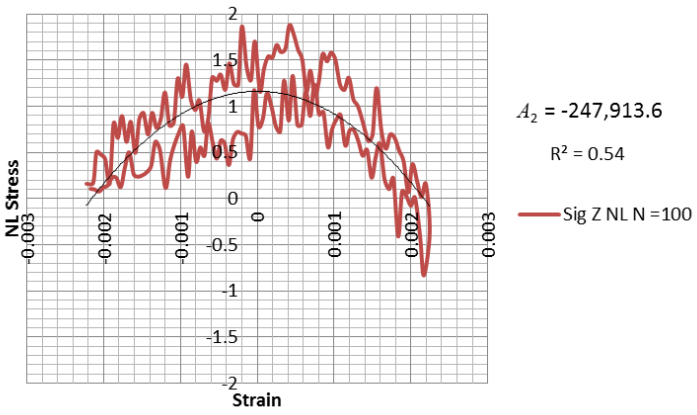

Figure 4.12: Plot of Equation (4.38) at N = 100 for Specimen 11.

In Figure 4.13, the nonlinear portion of the loop at N = 5,000 cycles in plotted. Note that compared to the loop at N = 100 cycles, the tension and compression portions of the loop are difficult to distinguish, indicating that strain hardening has occurred. Also, the R^2 value has improved from 0.54 to 0.65 and the improved fit is also visually apparent. Finally, the coefficient of the nonlinear term has decreased relative to the value seen at N = 100 cycles. This is hypothesized to be related to plasticity effects that are not accounted for in the derivation of Equation (4.25).

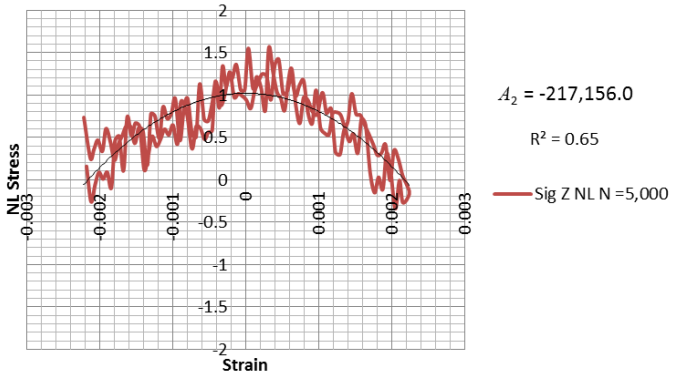

Figure 4.13: Plot of Equation (4.38) at N = 5,000 for Specimen 11.

Figure 4.14 (at N = 15,000) shows a 5% increase in the nonlinear term coefficient relative to N = 5,000 and further slight improvement in R^2. As before, the tension and compression sides of the loop show little separation.

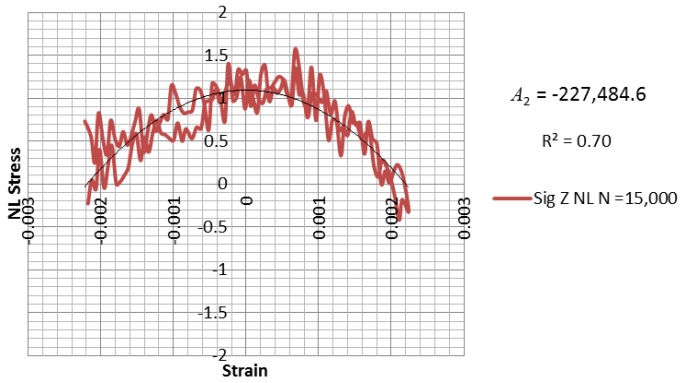

Figure 4.14: Plot of Equation (4.38) at N = 15,000 for Specimen 11.

Finally, Figure 4.15 is given at N = 38,000 or 99% of life. The expected dramatic increase in the value of nonlinear term is seen. Additionally, the R^2 value is 0.92. The good agreement between the parabolic curve and the data is clear from the figure.

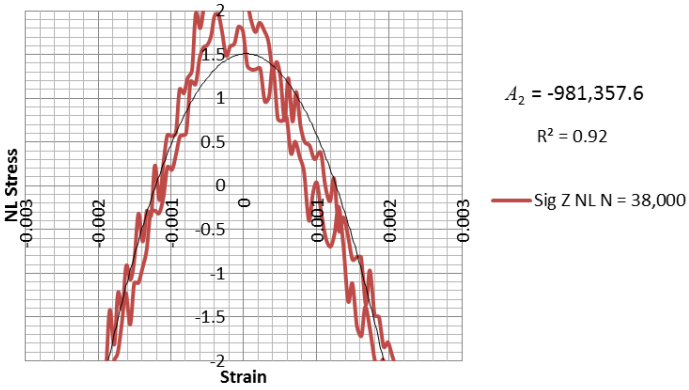

Figure 4.15: Plot of Equation (4.38) at N = 38,000 for Specimen 11.

In Figure 4.16, the plots of the non-linear term of the stress (Equation (4.38)) is shown for all specimens at the cycle count of 500 cycles before failure. It can be seen that all the plots have a generally parabolic, concave down shape that can be effectively modeled by a quadratic function of strain. Additionally, even though there is scatter between the plots, they overlap substantially.

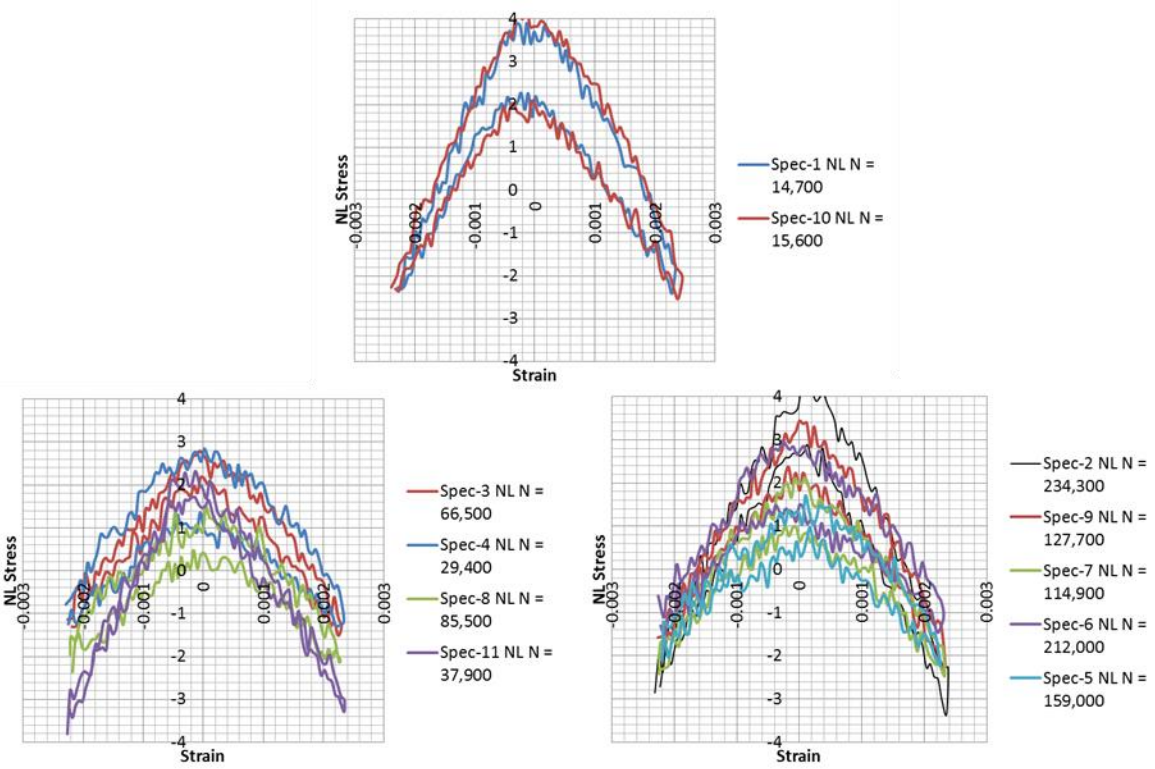

Figure 4.16: Plot of Equation (4.38) at N_f -500 for all specimens.

The plots D_N for the remaining specimens are reviewed below. A relationship between the shape of the curve and the specimen life was observed. Scanning Electron Micrographs of the fracture surfaces were also captured (Figures 4.18 through 4.21). Figure 4.19 shows an EDS composition map of the fracture area of Specimen 1. The indicated red areas reveal the presence of oxide inclusions (probably Al_2MgO_4 due to the higher concentration of O and Mg), which are known to be potential crack initiation sites in this alloy [1]. The region is on the order of 500 microns. In Figure 4.20 the fracture initiation site for Specimen 10 is shown. A porous region of about 600 microns is seen. To provide a point of comparison, a micrograph of Specimen 7 (N_f = 115,400) was taken and is shown in Figure 4.21. A relatively large silicon particle (identified in the EDS image) of about 50 microns can be seen at the fatigue crack initiation site. Note that the smaller crack initiation site corresponded to longer life in this case, in agreement with the trend described in [1]

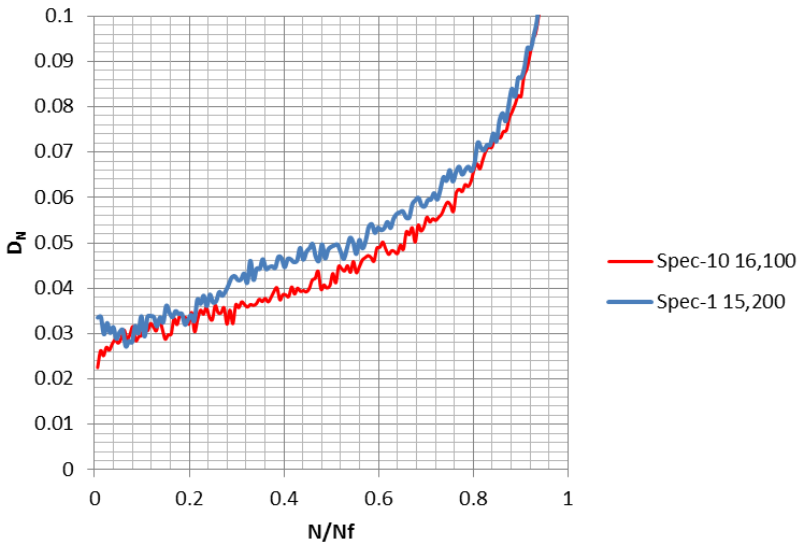

Figure 4.17: Plot of D_N for Specimens 1 and 10.

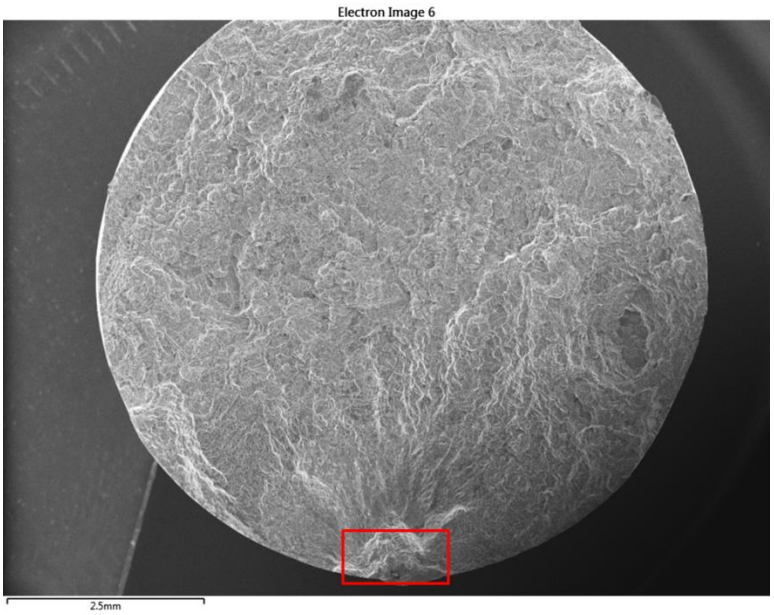

Figure 4.18: Micrograph of Specimen 1—crack initiation site at bottom.

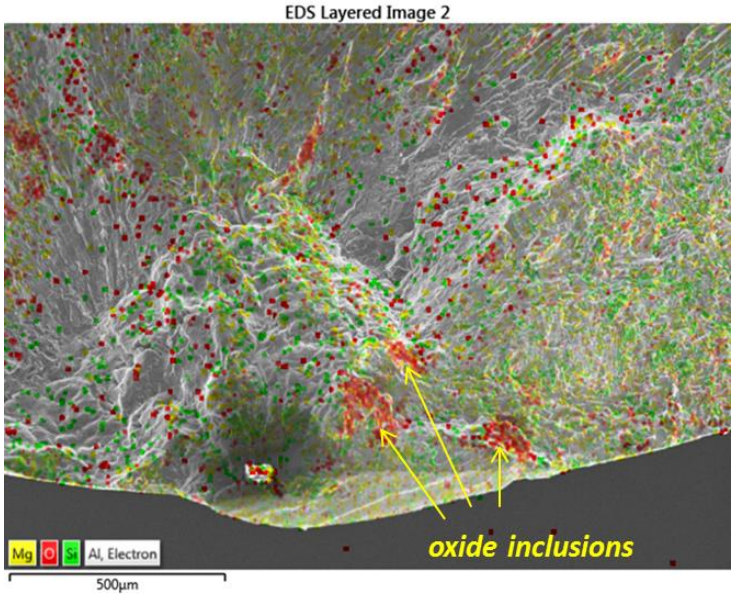

Figure 4.19: Micrograph of Specimen 1 showing oxide inclusions at crack initiation site.

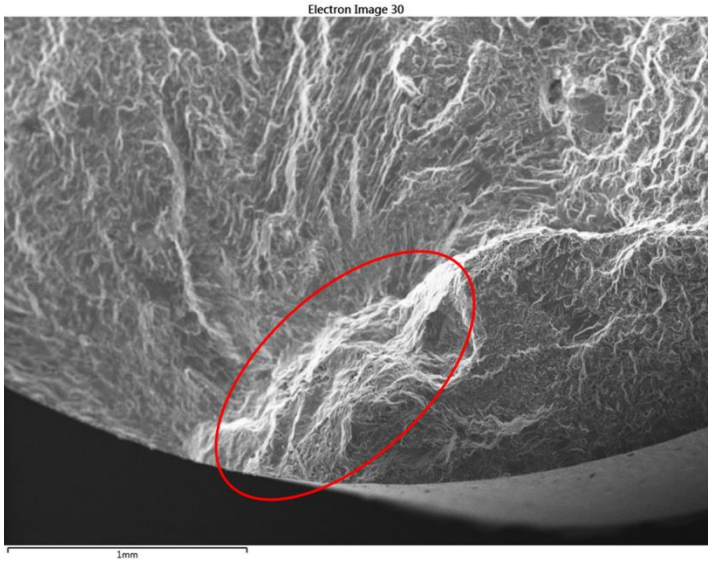

Figure 4.20: Micrograph of Specimen 10 showing porosity at crack initiation site.

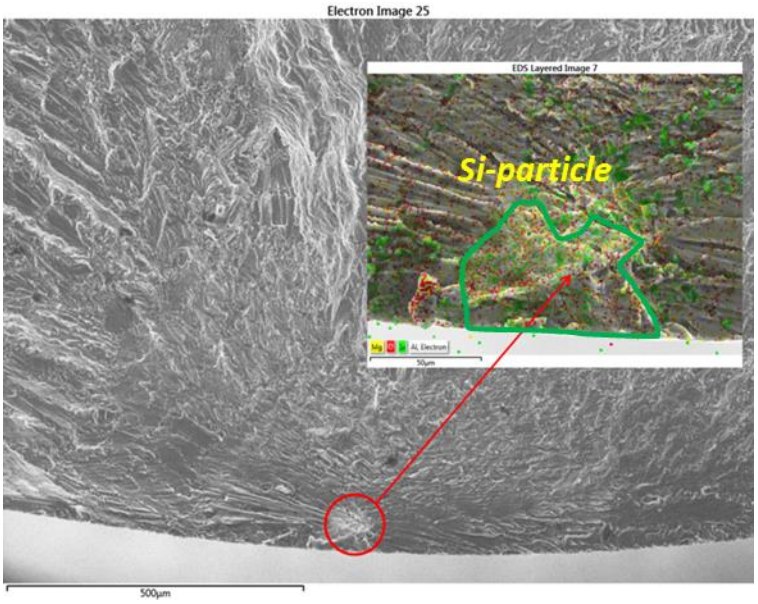

Figure 4.21: Micrograph of Specimen 7 showing a silicon particle at crack initiation site.

Another group of specimens failed at intermediate lives. The D_N plots for these are shown in Figure 4.22. These plots of D_N begin increasing at N/N_f values of 0.4 to 0.8. Compared to the plots in Figure 4.16, these plots increase more slowly and begin increasing later in the life fraction.

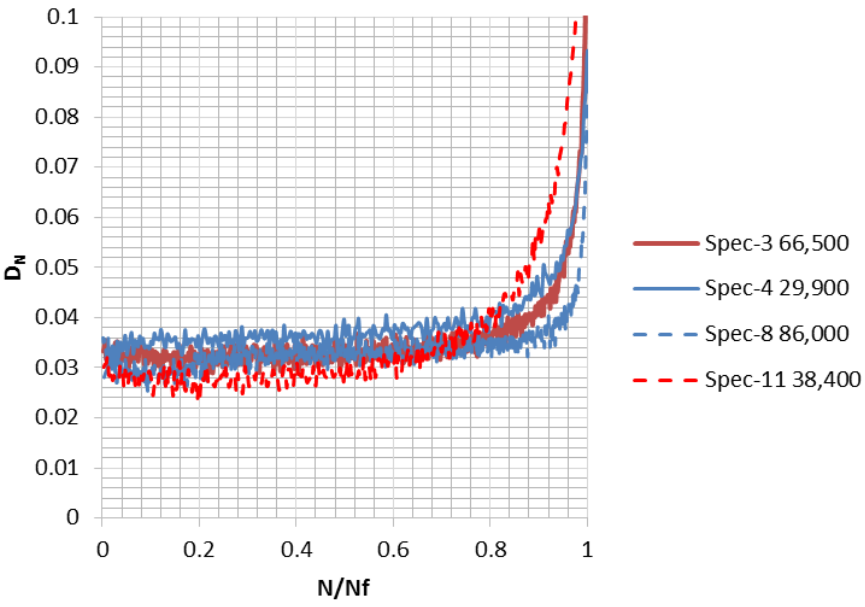

Figure 4.22: Plot of D_N for 3, 4, 8, and 11.

The remaining specimens survived between 115,400 and 234,800 cycles. The D_N plots for these are shown in Figure 4.23. These specimens did not exhibit an increasing trend in nonlinearity until late in life with N/N_f great than 0.8. A slight decreasing trend was observed on the in the case of Specimen 6 between $N/N_f = 0$ and $N/N_f = 0.7$. The reason for this is not clear although a slight initial decrease in nonlinearity during a VHCF test was also found in [48] and is visible in Figure 4.4. It is important to note that once the increasing trend begins late in the specimen's life, it accelerates and continues.

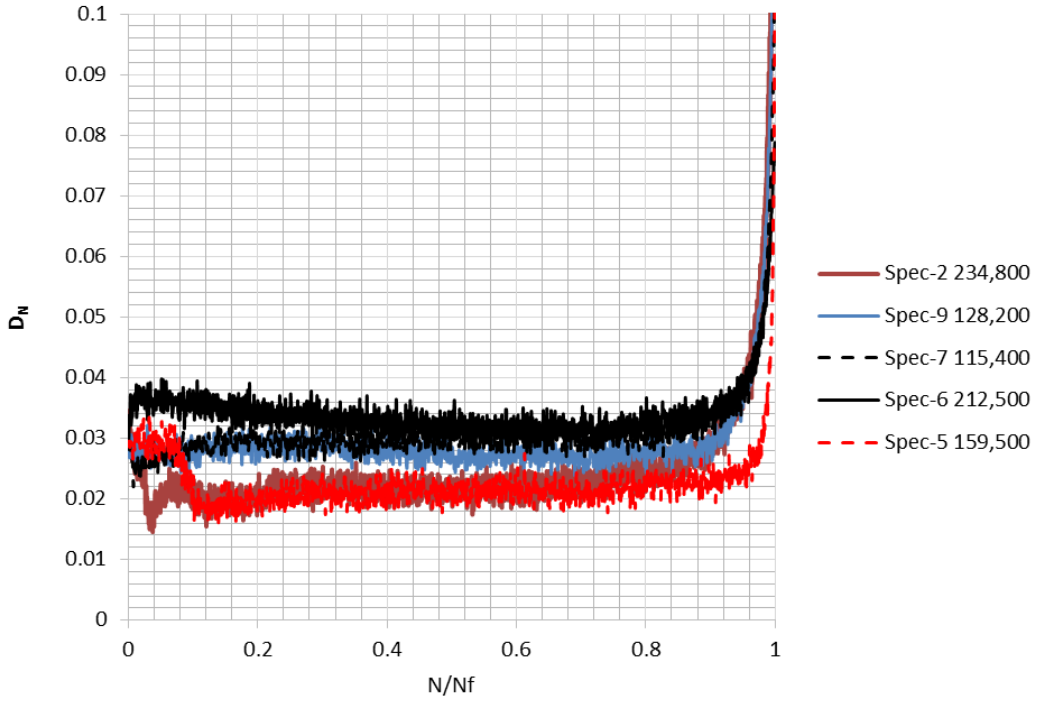

Figure 4.23: Plot of D_N for Specimens 2, 5, 6, 7, and 9.

4.8 Conclusions

A method to measure the progress of damage in an axial fatigue specimen, under fully-reversed HCF test conditions, was presented. A general elastic stress-strain relationship is used as a starting point to derive a one-dimensional stress-strain relationship exact in terms of engineering strain for homogeneous distortions. This relationship is found to not be a general power series, but a fourth-degree expression where both the third and fourth degree terms share the same

coefficient. For the present case where strains are smaller than 0.004, it was argued that only the first and second degree terms are needed. This second degree stress-strain law was used to derive a damage expression based on the continuum damage mechanics approach of measuring damage by comparing the stiffness in a specimen under tension to its stiffness under compression. Finally, a test program was undertaken to demonstrate application of this damage measurement approach to the high cycle fatigue testing of cast aluminum specimens.

Acknowledgements

The authors would like to thank Robert Frisch[1] for assisting in operating fatigue test equipment and collection of data, and also thank C. Carlos Engler-Pinto Jr.[2] for the SEM fractography and EDS analysis of the fracture surfaces.

[1] Both of Ford Motor Company

CHAPTER 5. APPLYING A SMALL CRACK GROWTH LAW TO DAMAGE INFERRED FORM TENSION-COMPRESSION ASYMMETRY

5.1 Introduction

It is useful to be able to monitor the progress of damage in a specimen under test. In this work, a small crack growth law is successfully fit to data collected during a sequence of high cycle fatigue tests of cast aluminum specimens. A damage parameter D_N based on a higher-order constitutive relationship is used to infer the progress of growing cracks. The measure of damage is based on the asymmetry between the tension and compression stiffness of a cracked body. A detailed finite element model of the fatigue specimen provides a connection between the measured values of D_N and the size of the crack. Finally, the fitted small crack growth model is shown to yield fitted initial flaw sizes well correlated with the flaw sizes measured in the fractured specimens.

5.2 The Small Crack Growth Model

It is a fundamental result in linear elastic fracture mechanics that the growth rate of a crack in an elastic body is characterized by the range in the stress intensity parameter K [10], provided the conditions of small scale yielding apply. Additionally, no growth of the crack is predicted if the stress intensity range is less than the threshold stress intensity range for the material in question. However, it has been known for some time that small cracks, less than about 1mm to 2mm in length, will grow even if the apparent delta K is less than the threshold delta K ([57]), and that they may grow much faster than expected by application of delta K growth laws for values of delta K around the threshold value ([57], [10], McDowell). Additionally, small cracks exhibit other anomalous behaviors, such as intermittent arrest and acceleration [16], greater scatter in growth rate relative to longer cracks [11], and initial rapid growth that eventually ends with crack arrest as the apparent threshold delta K value is approached by the growing crack [58]. Various mechanisms have been proposed to explain small crack behavior. The authors of [16] show the relationship of episodes of growth and temporary arrest to the interaction of the crack with microstructural barriers in the metal. The crack is shown to pause in its growth when grain

boundaries or inclusions are encountered. The authors of [58] built an FE model to predict the effect of closure on a small crack, which showed that initially minimal closure forces grow with the small crack and eventually arrest it if the applied load range is sufficiently low. This behavior contrasts with LEFM where the plastic wake of the crack is established and the closure force does not increase purely due to increases in crack length. Thus, it has been established the delta K parameter is not suitable for predicting the growth of small cracks under many conditions, motivating the development of alternative approaches. Many small crack growth laws abandon the delta K parameter in favor of explicit dependence on remote stress range and crack length, allowing departures from the strict relationship between these values assumed in the definition of stress intensity. There is a significant amount of literature supporting small crack growth laws that are linear in crack length with some separate dependency on far field stress.

The authors of [13] derive a linear (in crack length) da/dN law based on two principles. First, the growth of a crack on a given cycle is expected to be proportional to the size of the cyclic plastic zone, since crack propagation results from inelastic processes at the crack tip. The present authors comment that this assumption is consistent with regarding the cyclic plastic process zone as a region where low-cycle fatigue is occurring on a small scale. Secondly, the authors of [13] present experimental evidence that the size of the cyclic plastic zone is proportional to the crack length if the far field stress is greater than 0.6 Sy. Additionally, the dependency on stress is taken to be a power law based on reasoning from the Dougdale model for unidirectional loading. The resulting da/dN law is given in Equation (5.1). They show that this equation models the growth rate of small (0.05mm to 1.5mm) cracks in carbon steel specimens at stresses greater than 0.6 Sy:

$$\frac{da}{dN} = C\Delta\sigma^m a \tag{5.1}$$

The restriction that remote stresses are greater than 0.6 Sy is satisfied in the present work. The authors of [13] point out that cyclic plastic zone size is closely related to crack tip opening displacement. The authors claim that this assumption allows a unifying treatment of small cracks (with Equation (5.1)), with a large crack law based on delta K. The authors of [59] also

point out the connection of crack tip opening displacement (CTOD) to small crack growth and presented an equation of similar form to Equation (5.1) also linear in crack length. In [59] it is claimed that the growth law has been demonstrated for two cast Al-Si alloys with cracks in the length range of 0.1mm to 1.0mm and is valid for steel alloys as well. In [60] the author demonstrated a law of the form of Equation (5.1) for a nickel alloy in the applied stress range of $0.52\ Sy \leq S \leq 0.66\ Sy$, for cracks up to 0.3mm. The authors of [61] demonstrated a similar law for a different nickel alloy for cracks in the range of 0.05 to 2.0mm. Data for specimens with small holes (to initiate a crack) and smooth surfaces both followed the growth behavior implied by Equation (5.1). In [19], the authors studied steel specimens in the low cycle fatigue regime (remote stress up to 1.9 Sy) and found a law of the form of Equation (5.1) applied. Both plain and hole-containing specimens were tested. Data was presented for cracks from .05 to 1.0 mm in length. Finally, the authors of [62] studied steel specimens subjected to pre-strain and again found an equation of the form of Equation (5.1) applied for crack lengths up to 1.5mm.

Consider a more general da/dN equation given in Equation (5.2). This relationship assumes the form of the Paris law [3] if $m = 2n$.

$$\frac{da}{dN} = C\Delta\sigma^m a^n \tag{5.2}$$

It can be shown that constant amplitude loading, the integral of Equation (5.2) can be represented according to Equations (5.3) and (5.4) or Equation (5.5), depending on the value of n (assuming an initial crack length of a_0). In Equations (5.3) and (5.4) we consider the case of $n = 1$. We simplify with the substitution $c = C\Delta\sigma^m$. The growth is exponential and the ratio of the current crack length a (at current cycle N) to the initial crack length a_0 grows geometrically in N and is not a function of a_0. Thus, in the case of Equation (5.1) it is possible to model the growth of the crack relative to its initial size a_0 without knowledge of a_0. The largest initial crack grows to become the dominant crack as fatigue processes progress. One could define a dimensionless parameter as this ratio, which would be an explicit function of the applied load range and N.

$$a = a_0 e^{cN} \tag{5.3}$$

$$\ln\left(\frac{a}{a_0}\right) = cN \tag{5.4}$$

In Equation (5.5) we consider the case of $n \neq 1$. The ratio of the current crack length to the initial crack length is still a function of a_0 and normalization of the crack length relative to a_0 is not useful. Additionally it can be shown that for $n > 1$, Equation (5.5) predicts that the ratio $\frac{a}{a_0}$ increases more rapidly as a function of N for cracks with larger a_0. Thus as was case for the $n = 1$ case, a collection of small initial cracks would be expected to yield a dominant crack as fatigue processes progressed. Except, in this case, the dominant crack becomes proportionally larger than the other cracks over the course of the test. The constant n is typically seen in the range of 1 to 5 [3].

$$\ln\left(\frac{a}{a_0}\right) = \frac{1}{1-n}\ln(1 - {a_0}^{n-1}C(n-1)\Delta\sigma^m N) \tag{5.5}$$

The form of Equations (5.1) and (5.3) is fortuitous and enables inferences to be made about the proportional growth of a crack or even a collection of cracks of various initial sizes without detailed knowledge of the initial crack sizes.

In the present work, we are concerned with the cast aluminum alloy AS7GU in the T6 condition. The far field stresses are 0.77 Sy and the specimens are subject to fully reversed axial loading. No hole or other stress concentrating feature has been deliberately incorporated into the specimens. However, as previous authors have noted (see [1]), fatigue failure in this material begins at existing crack like flaws in the material. This earlier finding is confirmed in the present work through fratographic analysis of the separated specimens. The specimens had a round cross section with a gauge diameter of 7.62mm (0.30 inches) over a gauge length of 25.4mm (1.00 inch).

5.3 Damage as a Function of Measured Stiffness

In Chapter 4, a quadratic stress strain law was used to model the stress strain behavior measured during a constant amplitude load-controlled high-cycle fatigue test. A general non-linear material model was used as a starting point for the derivation of a stress strain relationship. A detailed derivation was given in Chapter 4 and is briefly reviewed here. The material model is given in Equation (5.6) [54]. In this expression, $\bar{\bar{B}}$ is the left Cauchy-Green tensor $\bar{\bar{I}}$ is the identity tensor, and the remaining variables are elastic constants.

$$\bar{\bar{\sigma}} = \left(\alpha_0 + \alpha_1 \mathrm{Trace}(\bar{\bar{B}})\right)\bar{\bar{I}} + \alpha_2 \bar{\bar{B}} + \alpha_3 \left(\bar{\bar{B}} - \bar{\bar{I}}\right)^2 \tag{5.6}$$

This material model is applied to an isotropic material under uniaxial stress and stress-strain relationship is shown to be given by Equation (5.7).

$$\sigma_x = (\epsilon_x + 1)A_3{\epsilon_x}^3 + A_2{\epsilon_x}^2 + A_1\epsilon_x \tag{5.7}$$

This result is noteworthy in that it shows that even the most general uniaxial material model, arising from Equation (5.6), is at most a fourth degree relationship. Furthermore, the coefficients on the third and fourth degree terms are the same. Thus for small strains we can immediately neglect the fourth degree term. Finally, we argue that for our present purposes, where strains are less than 0.003, even the third degree term may be neglected and we are left with a form similar given in Equation (5.8).

$$\sigma_{xN} = A_{2N}{\epsilon_x}^2 + A_{1N}\epsilon_x \tag{5.8}$$

The subscripts in the coefficients contain *N* to highlight the fact that they are expected to change in value over the course of the test. The change in value of the coefficients, especially the quadratic coefficient, may be used to track damage in a manner consistent with the definition of damage at any cycle:

$$D_N = 1 - \frac{\frac{\sigma_{tens}}{\epsilon_{tens}}}{\frac{\sigma_{comp}}{\epsilon_{comp}}} = 1 - \frac{\sigma_{tens}}{|\sigma_{comp}|} \quad for\ \epsilon_{tens} = -\epsilon_{comp} \tag{5.9}$$

We begin by taking the derivative of Equation (5.8) and combining it with Equation (5.9). The numerator (corresponding to tension) is evaluated at a positive reference strain ϵ_{ref} while the denominator (representing compression) is evaluated at the negative of the same reference strain.

$$D_N = 1 - \frac{\left.\frac{d\sigma_{xN}}{d\epsilon_x}\right|_{\epsilon_x=\epsilon_{ref}}}{\left.\frac{d\sigma_{xN}}{d\epsilon_x}\right|_{\epsilon_x=-\epsilon_{ref}}} = 1 - \frac{A_{1N} + 2A_{2N}\epsilon_{ref}}{A_{1N} - 2A_{2N}\epsilon_{ref}} \tag{5.10}$$

Figure 5.1 shows the significance of the reference strain values relative to the quadratic stress-strain law. Equation (5.12) evaluates D_N in terms of the relative slopes of the tangent lines L_{tens} and L_{comp} shown in the figure.

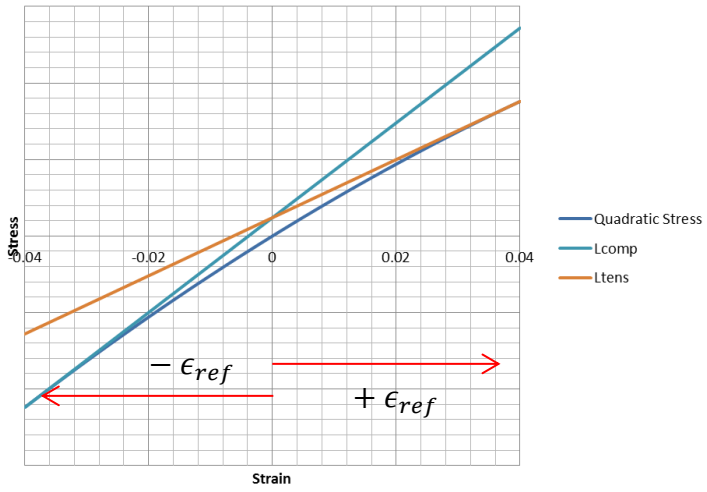

Figure 5.1: Definition of reference strains to evaluate tangent slopes to quadratic stress strain model.

We define β_N (Equation (5.11)) as the ratio of the quadratic and linear coefficients, consistent with the notation of Equation (5.8). Since the stress-stain curves in practice are concave-down, the coefficient A_{2N} is negative and β_N is also.

$$\beta_N = \frac{A_{2N}}{A_{1N}} \quad \beta_N < 0 \tag{5.11}$$

Combining with Equation (5.10) and linearizing (since the values of D_N here are less than 0.05) gives Equation (5.12). This is the expression used to evaluate of D_N in the work that follows.

$$D_N = 1 - \frac{1 + 2\beta_N \epsilon_{ref}}{1 - 2\beta_N \epsilon_{ref}} \approx -4\beta_N \epsilon_{ref} \tag{5.12}$$

5.4 Damage Corresponding to Cracks of Given Sizes

Many arguments in CDM, although they assume a population of cracks, do not depend on actually modeling their size. However, the contribution of a particular crack of size a_i is argued to be proportional to the area of the crack as given in Equation (5.13):

$$D_i = \rho {a_i}^2 \tag{5.13}$$

The author of [20] also presents a separate argument based on linear elastic fracture mechanics that results in Equation (5.14).

$$D_i = \rho {a_i}^3 \tag{5.14}$$

In [53] is was also found that the reduction in stiffness of a cracked body was given by Equation (5.14) in the limit of small cracks that do not elastically interact with one another. Several continuum mechanics approaches were compared, incorporating different assumptions about the interactions of the cracks. Their predictions all converged in the small crack limit. The form of Equation (5.14) can be interpreted as associating a weakened volume of material enclosing a particular crack of size a_i. This is reasonable considering that material close to the plane of the crack would be lightly loaded since the crack surface is a free surface from the point of view of the stress field. One important result of the form of Equation (5.14) is that the effect of differences in crack sizes is magnified. If one crack is 50% larger than another, its damage contribution with be 3.4 times as great. The value of D_N will tend to be dominated by the largest cracks present in the specimen. The development that follows will proceed along the lines of Equation (5.14) although it was expected that as cracks exceed some critical fraction of the cross section of the specimen, the relationship may depart from the form of Equation (5.14). A numerical study was undertaken to characterize the functional relationship between axial stiffness and crack size, including large cracks of the sizes found in separated specimens.

To gain insight into underlying mechanics, a mechanical model is proposed below to justify the form of Equation (5.14). Our analysis is intended to only be valid in the small crack case. The effect of cracks up to a large size will be determined in a numerical study. First, in Equation (5.15), we define the stiffness of an axially loaded body, with a constant cross sectional size and shape, where P is the applied axial load and u_z is the axial displacement. Damage D can be defined in terms of the changes in stiffness as defined in Equation (5.9), where K_0 is the stiffness of an un-cracked body and K_t is the stiffness of the cracked body.

$$K = \frac{P}{u_z} \tag{5.15}$$

$$D = 1 - \frac{K_t}{K_0} \tag{5.16}$$

Restricting our attention to axially loaded bodies with a constant cross sectional size and shape, we hypothesize that a relationship of the form of Equation (5.17) may be found, where ρ is a function of the shape (but not the size) of the body and the crack and ϕ is a function of dimensions of the body. The goal is to determine ρ for a given crack and body geometry through a numerical study. The factor ϕ enables the solution to be used for other crack and body sizes (but similar shapes). This approach is successfully demonstrated below.

$$1 - \frac{K_t}{K_0} = \rho \frac{a^3}{\phi} \tag{5.17}$$

We begin by noting that the axial stiffness of a body of constant cross section will be proportional to a transverse dimension squared divided by the length as given in Equation (5.18). Dimensions are explained in Figure 4.

$$K_0 \propto \frac{d^2}{L} \tag{5.18}$$

The assumptions employed in the development below are the following. With the exception of the presence of a crack at some axial position, the cross section of the body is constant. Also, the body is under uniaxial stress. Finally, the crack is small relative to the cross section. We argue

that for a small crack of general shape, its effect on the axial stiffness of the body is equivalent to a void as shown in Figure 5.2. We do not specify the shape of the equivalent void, but only seek to describe its effect on the axial stiffness of the body.

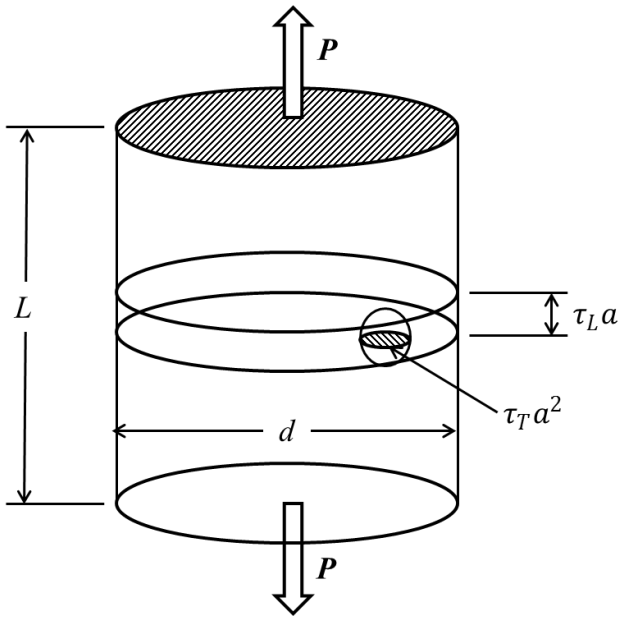

Figure 5.2: Idealized axially loaded cracked body.

Next we note that an axially-loaded cracked body may be regarded as an axially short cracked body in series with a much longer un-cracked body. We apply the rule for the total stiffness of two bodies in series in Equation (5.19). We note that stress may vary in a given transverse plane but assume that strains do not vary within transverse planes.

$$\frac{1}{K_t} = \frac{1}{K_{cracked}} + \frac{1}{K_{intact}} \tag{5.19}$$

In Equation (5.20) we assume that from the point of view of the axial stiffness of the body, the axial effect of the crack is equivalent to a void of height $\tau_L a$ where τ_L is an unknown constant (Figure 5.2) that models the effective axial length of the void that is equivalent to a crack of a particular shape. Additionally, we introduce a constant τ_T such that the term $\tau_T a^2$ is equal to the effective transverse area of a void equivalent to a crack of a particular shape. The values of these constants are assumed to be specific to different crack and body geometries and would need to be determined through analysis, experiment or numerical simulation. The key point is that the once

the constants are determined, the effect of the crack could be determined for cracks and bodies of other sizes by applying the formulas developed below.

$$\frac{1}{K_t} \propto \frac{\tau_L a}{(d^2 - \tau_T a^2)} + \frac{(L - \tau_L a)}{d^2} \tag{5.20}$$

Manipulation of Equation (5.20) yields Equation (5.21). Note that the first term on the right hand side of Equation (5.20) is proportional to the compliance of the un-cracked body and thus the term on the right represents the increase in compliance due to the presence of the crack.

$$\frac{1}{K_t} \propto \frac{L}{d^2} + \frac{\tau_L \tau_T a^3}{d^4\left(1 - \tau_T\left(\frac{a}{d}\right)^2\right)} \tag{5.21}$$

Finally, Equation (5.21) may be simplified by considering that $a << d$ and may be rewritten as Equation (5.22). The case of larger a is considered separately with a finite element study in the following section. The ratio of the cracked to un-cracked stiffness is then given by Equation (5.23). Note that the length and area constants now appear in a single term (with a^3) suggesting the interpretation of the product as an equivalent volume corresponding to the crack geometry. Additionally, the denominator contains a product proportional to the volume of the body.

$$\frac{1}{K_t} \propto \frac{L}{d^2}\left(1 + \frac{\tau_L \tau_T a^3}{L d^2}\right) \tag{5.22}$$

$$\frac{K_t}{K_0} = \frac{1}{1 + \frac{\tau_L \tau_T a^3}{L d^2}} \tag{5.23}$$

Next, applying Equation (5.16) (resulting in Equation (5.24)) and linearizing, since the quantity containing the variables will always be very small, we arrive at Equation (5.25). We set τ equal to $\tau_L \tau_T$.

$$D = 1 - \frac{K_t}{K_0} = 1 - \frac{1}{1 + \frac{\tau a^3}{Ld^2}} \tag{5.24}$$

$$D = 1 - \frac{K_t}{K_0} = \frac{\tau a^3}{Ld^2} \tag{5.25}$$

Recall that the cubic dependency of damage on crack size is an existing result that is seen in previous work. The point of Equation (5.25) is to expose the value of the constant of proportionality and develop a scalable law that can be applied to crack and body geometries of different sizes once the solution for a reference crack and body shapes is available.

Figure 5.3 shows the crack geometries assumed to exist in the specimens for two different representative sizes. This shape is one of several seen in the literature ([63], [64]) and will be shown to be a reasonable approximation of the actual final crack shapes in the separated specimens.

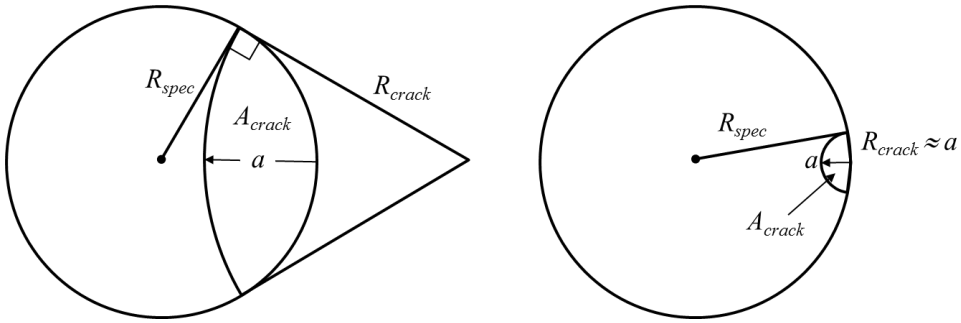

Figure 5.3: Proposed crack geometry shown for large and small crack.

The defining characteristic of the proposed crack shape (of all sizes) is that the crack front is a circular arc that intersects the surface of the specimen at a right angle. For small cracks, this results in essentially semicircular cracks as can be seen in Figure 5.3 in the diagram on the right. The large crack limiting shape is a linear crack front that divides the specimen in half. Thus this model would not be appropriate for fatigue cracks that progressed beyond 50% of the specimen area. In the present case the final cracks were between 24% and 33% of the area of the specimen. Furthermore, the final crack shapes will be shown to be reasonably approximated by the shape

proposed in Figure 5.3. The depth of the crack *a* is defined as the depth at the midline as shown in Figure 5.3. The depth of the final cracks in separated specimens was measured as follows. The area of the final crack was measured on a micrograph and the depth *a* was defined as the depth of a crack corresponding to the Figure 5.3 geometry that had the same area.

Figure 5.4 shows the FE modeled region of the fatigue specimen—the model represents ½ of gauge section of specimen. The crack is assumed to grow in a plane perpendicular to loading axis. This characteristic is seen in separated specimens. For modeling purposes the plane of crack is a plane of symmetry, thus half of the specimen is modeled. Finally, the specimen is assumed to be in a state of uniaxial tension.

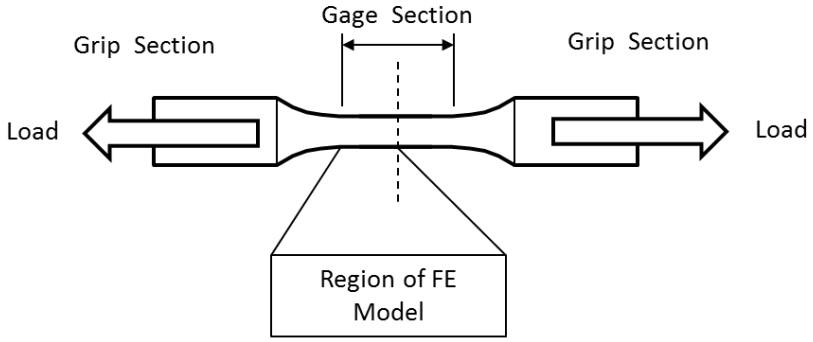

Figure 5.4: Region of specimen corresponding to FE model.

Nine different crack sizes, ranging from 1% to 33% of the specimen cross section area were modeled, as well as an un-cracked specimen. Cracks were modeled by applying displacement control to node sets on end of specimen that represented the crack plane. The cracked portion was not included in the node set (details given later). The opposite end, at the end of the gage section, was kinematically constrained to a node for which the reaction force was tabulated. Thus, the stiffness of the specimen was a modeling output. The modulus was set at 10 times the modulus of aluminum to improve resolution of output. The damage *D*, as defined in Equation (5.9), was computed for each crack size modeled. It was assumed that the reference stiffness of the un-cracked specimen is the same as the specimen in compression with a crack of any size. Equation (5.26) gives the resulting definition of *D*.

Definition of Damage consistent with Equation (5.9):

$$D_{crack} = 1 - \frac{E_{tens\ crack}}{E_{comp\ crack}} = 1 - \frac{E_{tens\ crack}}{E_{intact}} \tag{5.26}$$

Axial stiffness was defined in terms of prescribed displacement of end nodes and the resulting reaction force. This computation was used for both the cracked and intact stiffnesses in Equation (5.27).

$$E = \frac{F_{out}}{\delta_{prescribed}} \quad \delta_{prescribed} = 0.005 \ \ same\ for\ all\ runs \tag{5.27}$$

Damage calculation resulting from substitution of Equation (5.27) into Equation (5.26) is given in Equation (5.28). This is the damage value used for Table 1.

$$D_{crack} = 1 - \frac{F_{out(crack)}}{F_{out(intact)}} \tag{5.28}$$

An image of the actual FE model mesh is given in Figure 5.5. The model was created using the Abaqus FE solver. The entire model consists of 624,000 elements. The finest elements were used in crack region and were 2nd order pentagonal prisms.

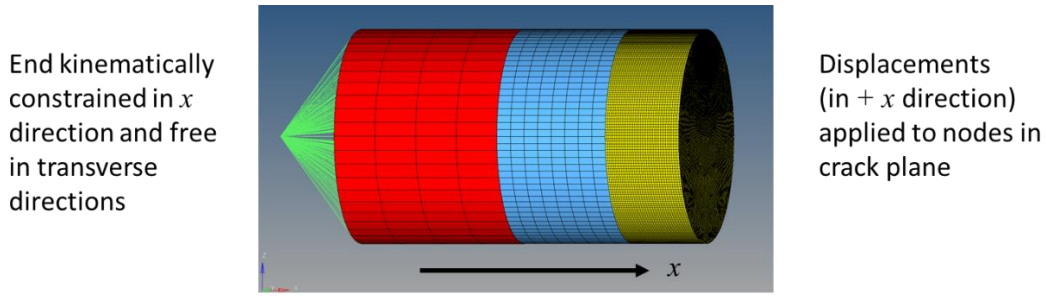

Figure 5.5: FE model mesh.

The remainder of model was comprised of hexahedral elements. No yielding was included in the model. The separate mesh regions were connected using tied contact. A detailed view of the elements in the crack plane is seen in Figure 5.6.

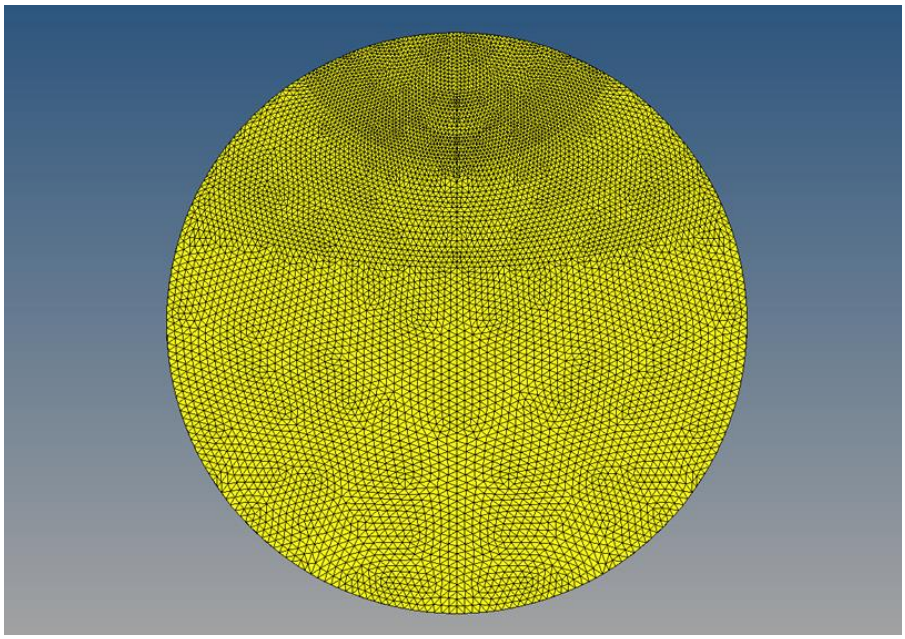

Figure 5.6: Mesh divided into regions corresponding to various crack sizes.

The element boundaries corresponding to the crack shapes can be clearly seen in the top half of Figure 5.6. The presence of a crack was modeled by apply a displacement (of 0.0005 mm) to only the portion of the crack plane that was intended to represent the un-cracked portion of the cross section. The cracked portion was left un-constrained and thus represented the free surface of a crack. In Figures 5.7, 5.8, and 5.9, displacement and stress plots are shown for three different crack conditions. The left side of the images shows axial displacement contours while the right side shows the axial stress. In Figure 5.7, the smallest crack modeled is shown, with a depth of 0.553 mm.

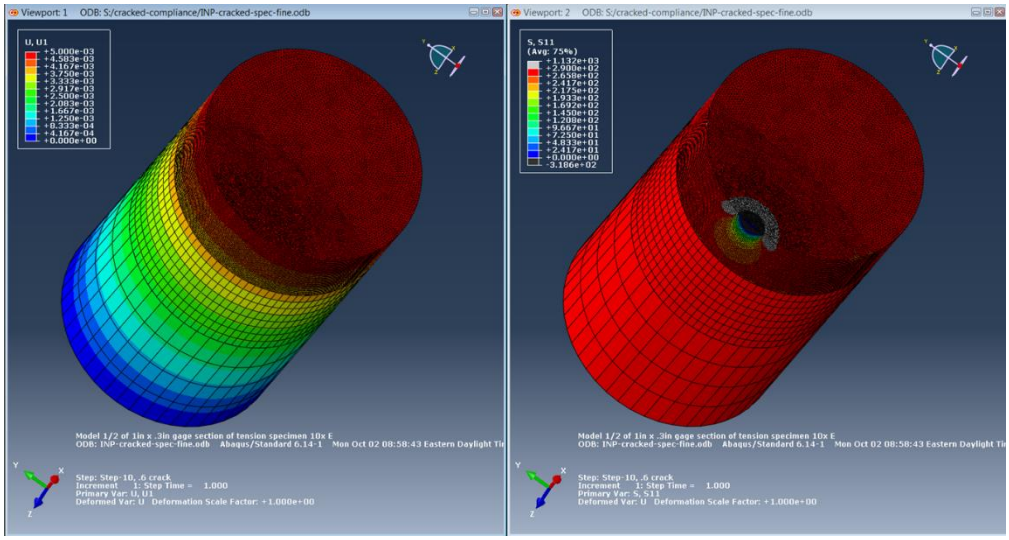

Figure 5.7: Axial displacement and axial stress corresponding to a crack depth of 0.553mm.

In Figure 5.8, a 1.02mm crack is modeled. Comparing Figure 5.7 to Figure 5.8 reveals the shape of the stress contours is similar between these two cases and is essentially scaled by the size of the crack. The non load-bearing volume of material close to the cracked region can be clearly seen. Both of these cracks have the essentially semicircular shape corresponding to the small crack rage of the geometry in Figure 5.3.

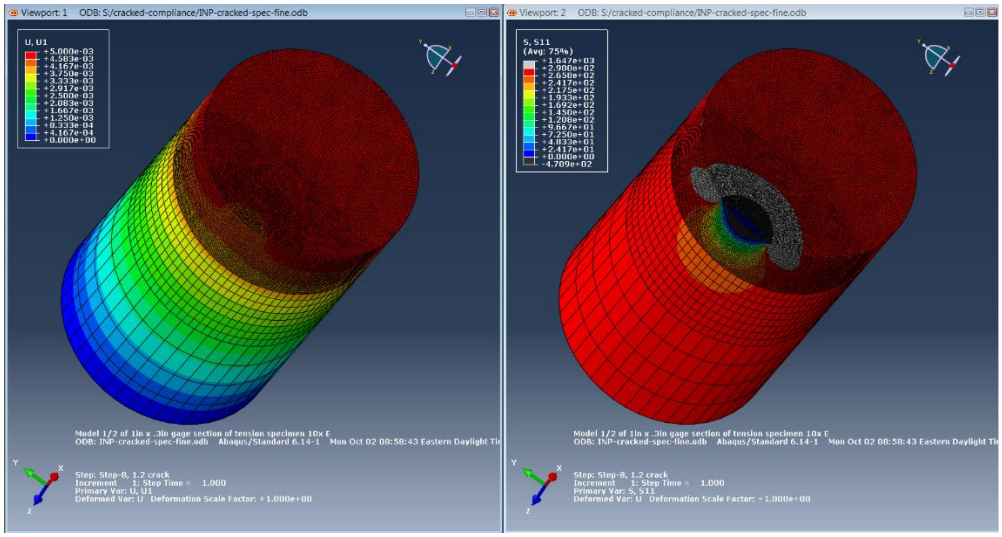

Figure 5.8: Axial displacement and axial stress corresponding to a crack depth of 1.02mm.

In Figure 5.9, the largest crack modeled (3.10mm) is shown. This crack is not semicircular and the stress contours have a distinctly different shape than was the case in the small crack examples.

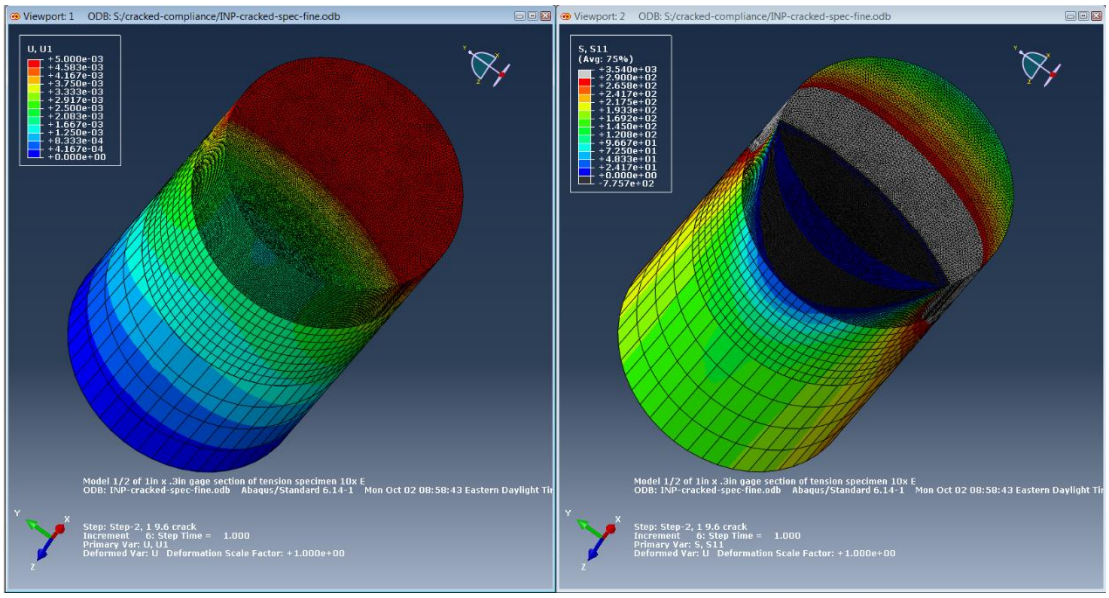

Figure 5.9: Axial displacement and axial stress corresponding to a crack depth of 3.10mm.

Table 5.1 below gives a summary of variables modeled and computed in the FE model.

Table 5.1: Finite element modeling results.

a	$(a^3)/(Ld^2)$	*Fout*	D_N
0.000	0.000E+00	1.25430E+04	0.00000
0.553	1.147E-04	1.25380E+04	0.00040
0.755	2.920E-04	1.25290E+04	0.00112
1.015	7.100E-04	1.25070E+04	0.00287
1.336	1.618E-03	1.24540E+04	0.00710
1.707	3.373E-03	1.23410E+04	0.01610
2.102	6.293E-03	1.21270E+04	0.03317
2.482	1.036E-02	1.17880E+04	0.06019
2.814	1.511E-02	1.13480E+04	0.09527
3.082	1.984E-02	1.08770E+04	0.13282

Plotting the damage D as a function of the first three values of $(a^3)/(Ld^2)$ (up to a size of a of 0.755mm on a 7.62mm diameter section) results in Figure 5.10. The linear behavior of Equation (5.25) is evident. From Equation (5.25), this gives us a constant tau of 2.96×10^{-6}.

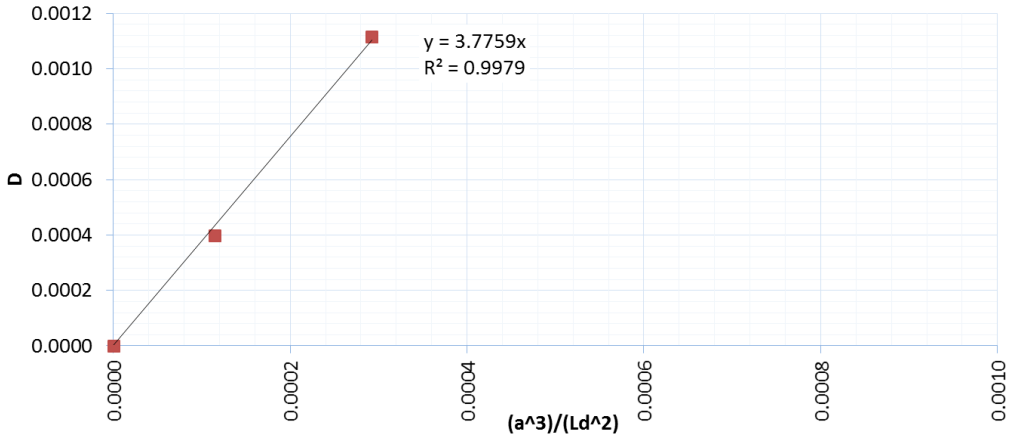

Figure 5.10: Plot of damage versus cube of crack length as given in Equation (5.25).

In Figure 5.11, data for all crack sizes is plotted, and nonlinearity is evident. The crack shape defined in Figure 5.3 changes with increasing crack size and contributes to the lack of linearity in Figure 5.11.

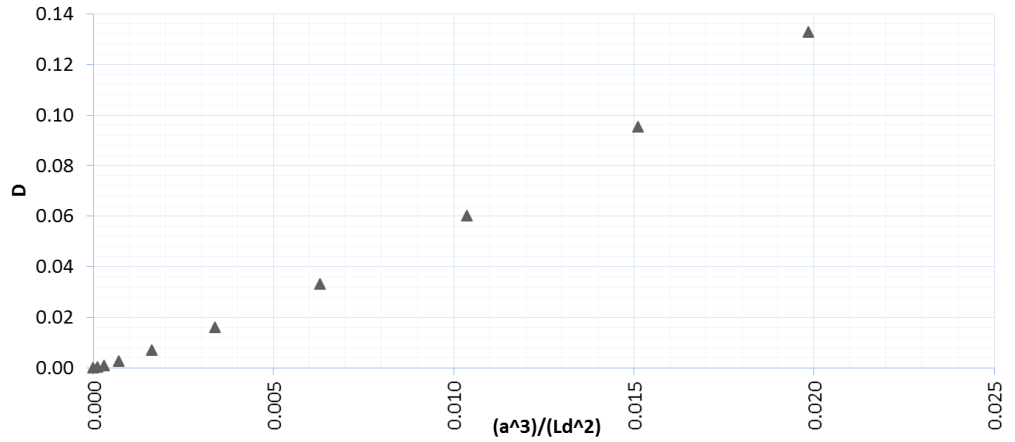

Figure 5.11: Plot of all crack sizes from Table 1.

Damage as a function of a as determined from the FE model is given in Equation (5.29). Note that a power law still applies, but that to fit cracks over a larger range, an exponent slightly different from 3 is required.

$$D = 0.00280a^{3.37} \tag{5.29}$$

For our purposes below, the inverse relationship is needed and is given in Equation (5.30). This was obtained by directly fitting the data in Table 5.1. This relationship is plotted in Figure 5.12. The power law form of Equation (5.30) is shown to provide excellent fit to the FE model results over a large range of damage D. Equations (5.29) and (5.30) have been shown to provide high-fidelity models of the D vs. a relationship for cracks of the geometry given in Figure 5.3 within the modeled range.

$$a = 5.71D^{0.296} \tag{5.30}$$

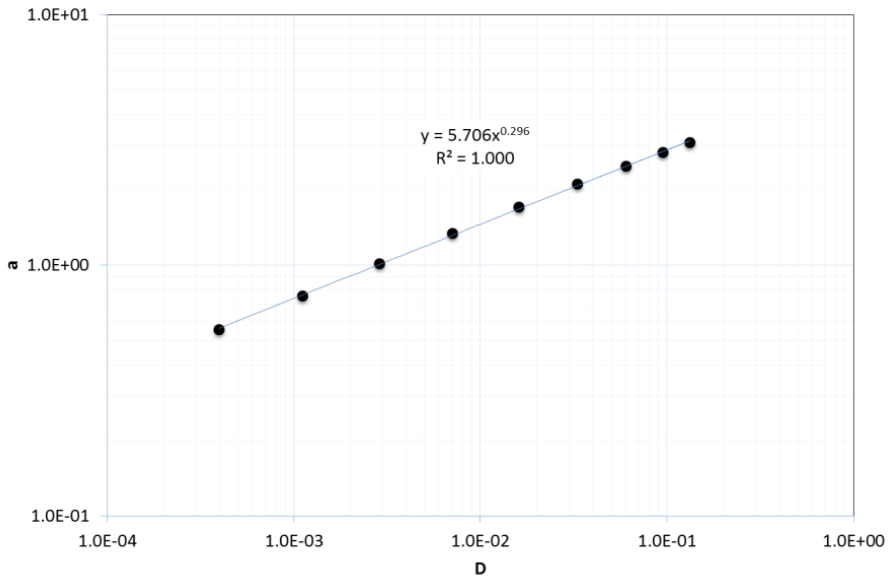

Figure 5.12: Plot of Equation (5.30) showing excellent fit over a range of crack sizes.

5.5 Fit of Small Crack Growth Law to D_N Data for 11 Fatigue Tests

An experimental program was undertaken where D_N vs. N data was obtained for 11 axial tension specimens as described in Chapter 4. These were fully reversed load-controlled tests to failure at a nominal stress of level of 170 MPa. The alloy was cast aluminum AS7GU. See [56] for a review of its properties. Strain data also collected during test. Data was gathered every 100

cycles and N_f was defined as the end of the last 100 cycle block completed prior to separation. Since even the earliest failure was 15,200 cycles, the final 100 block was less than 1% of N_f prior to separation. Load and stain data were collected. As discussed in Chapter 4, the load was converted to true stress based on Equation (5.31) which accounts for the slight Poisson contraction or dilation of the cross section under load.

$$\sigma_{i,N} = \frac{P_{i,N}}{\pi r_0^2 \left(1 - 2\,\nu \epsilon_{i,N}\right)} \tag{5.31}$$

The data analysis process is summarized in Table 5.2. Every 100 cycles a stress-strain loop is obtained which typically includes about 155 data rows. The quadratic stress-stain model (Equation (5.8)) is fit to the loop and the values of the coefficients found are used to compute D_N for that loop according to Equation (5.12). Thus a family of D_N vs. N curves were obtained.

Table 5.2: Summary of relationships used in data reduction.

$\{P_{i,N}, \epsilon_{i,N}\}$	Load vs. strain data for i^{th} data sample in N^{th} loop.
$\sigma_{i,N} = f(P_{i,N}, \epsilon_{i,N})$	Stress value σ_x for i^{th} data sample in N^{th} loop, computed from corresponding load and strain values according to Equation (5.31).
$\{\sigma_{i,N}, \epsilon_{i,N}\}$ i: 1,2, … n	Data set used for model fitting at the N^{th} loop.
$\sigma_{xN} = A_{2N}{\epsilon_x}^2 + A_{1N}\epsilon_x$	Quadratic stress-strain law resulting from least squares fit to the N^{th} loop (Equation (5.8))
$D_N = -4\beta_N \epsilon_{ref}$	Damage computed for the N^{th} loop (Equation (5.12))

After separation, the fracture surfaces of the separated specimens were examined with a scanning electron microscope and also an optical microscope. The SEM images were primarily used to determine the size and characteristics of fatigue crack initiation site. The optical images were used to measure the final crack size and shape prior to separation. A summary of the findings is given in Table 5.3.

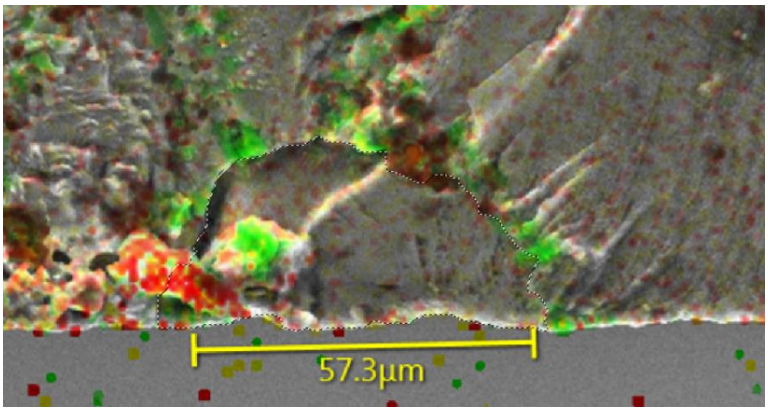

Figure 5.13: Electron dispersive spectrograph (EDS) image of specimen 6 initiation Site.

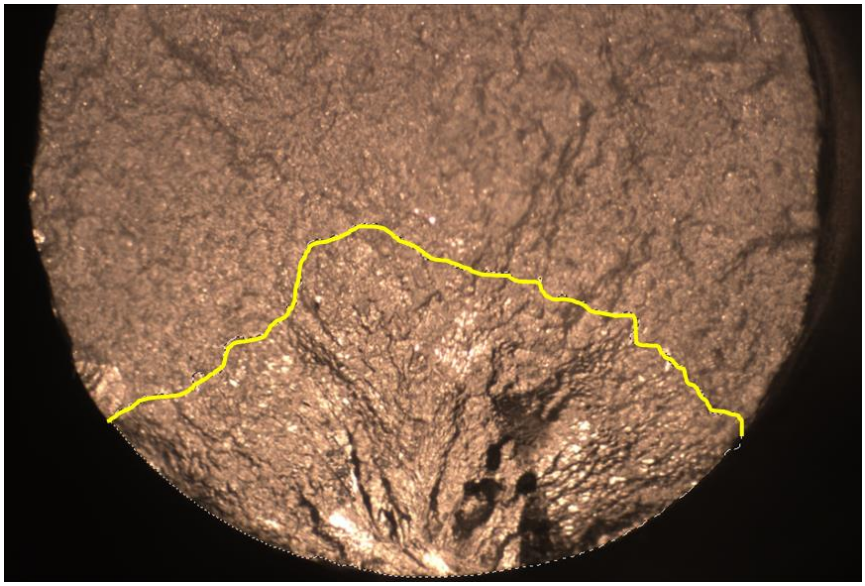

Figure 5.14: Optical micrograph of fracture surface of specimen 6 showing final fatigue crack.

The fracture surfaces were generally transverse to the loading axis. The size of the both initiation and final crack features on micrographs were measured using the image analysis capabilities of Photoshop. As has been reported previously with this material [1], the fatigue lives of specimens of this material are inversely related to the size of crack initiation features. A plot of the data is given in Figure 5.15. It will be shown later that this behavior is consistent with the small crack growth law stated in Equation (5.3).

Table 5.3: Summary of initial flaw and final crack areas and depths.

N_f	Area A_0	Area A_f	a_0	a_f	$ln\ a_0$
15200	0.671	13.0	0.647	2.848	-0.435
16100	0.499	11.8	0.558	2.714	-0.583
29900	0.363	12.7	0.476	2.815	-0.742
38400	0.336	12.9	0.458	2.837	-0.781
66500	0.222	14.6	0.372	3.019	-0.988
86000	0.182	15.1	0.337	3.070	-1.088
115400	0.00866	10.8	0.074	2.596	-2.610
128200	0.0094	11.6	0.077	2.691	-2.569
159500	0.0102	14.7	0.080	3.029	-2.528
212500	0.00151	12.9	0.031	2.837	-3.484
234800	0.0021	14.5	0.036	3.008	-3.319

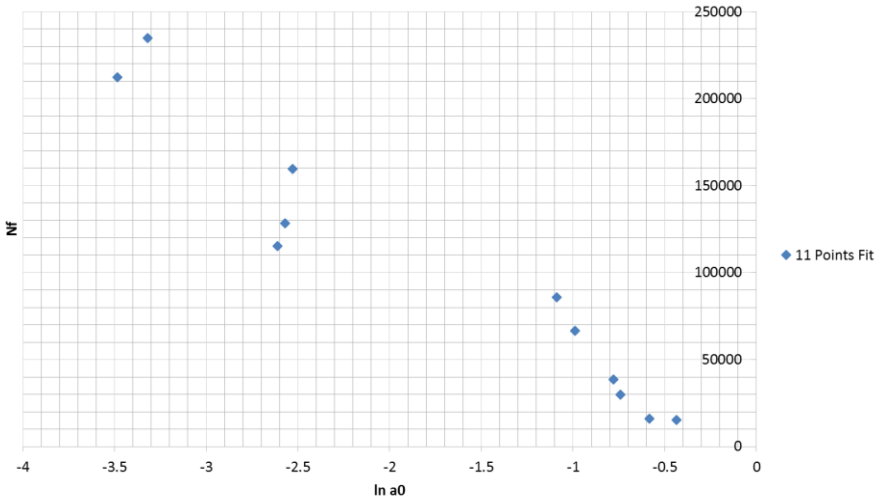

Figure 5.15: N_f vs. ln(a_0) showing a linear trend.

The D_N vs. N curves exhibit several noteworthy features. A representative example is given in Figure 5.16 below. As expected, they begin at a relatively low value and curve upwards as N_f is approached. This increase in D_N is claimed to correspond to growth of the dominant crack that eventually leads to separation of the specimen. The curves also exhibit noise due to the subtlety of the phenomenon being measured. Finally, the curves exhibit a positive offset of unknown cause. The values of this offset were in the range of D = 0.02 to 0.033.

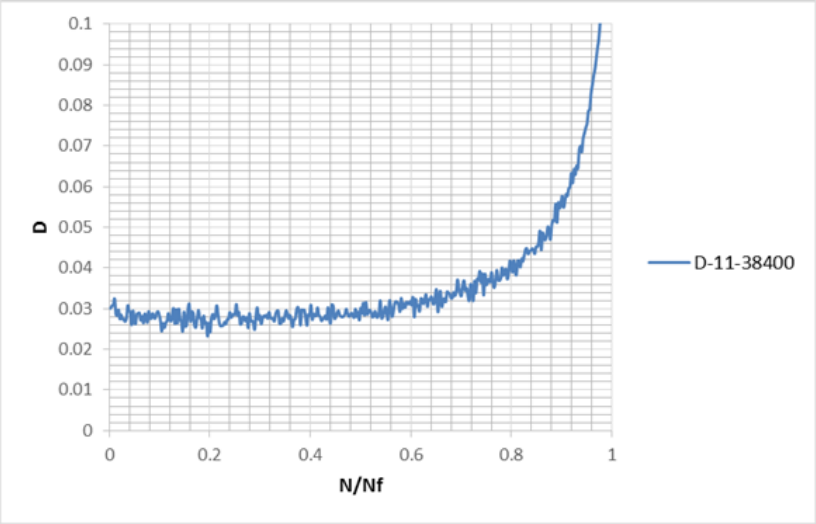

Figure 5.16: Representative example of raw D_N vs. N curve.

In order to address the noise the raw data was smoothed in Matlab using the command 'smooth(*data*, 75, 'lowess')'. 'lowess' is *locally-weighted linear regression* over a window of some fraction of the total record (75 points in our case) [65]. Other narrower and wider windows were tried as well as the alternative 'loess' which regresses to a quadratic curve. The chosen method offered the best tradeoff of trend fidelity to noise/oscillation removal. The intention was to smooth the data conservatively in order to minimize distortion. The following were steps were taken in the analysis of the data. Force data to D=0 below the final 60,000 cycles if a record is longer than that. Otherwise don't change. This is justified based on the fact that the data doesn't trend upwards until after this value typically. Next we took the minimum value of the curve in the last 60k cycles *min(i)* and removed portion of curve to left of minimum if necessary so that the curve is monotonically increasing. Finally, we shifted all curves down by min(i). Thus all curves start at Di = 0 and are strictly zero to the left of this value if it is not zero. They increase almost monotonically from this value. The resulting curves are shown below in Figure 5.17.

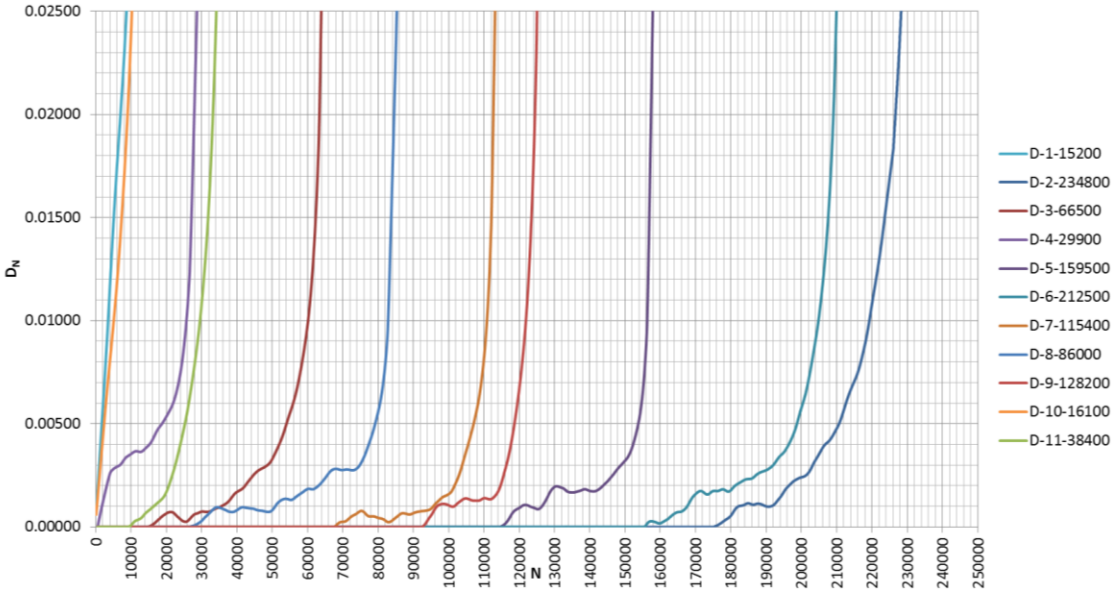

Figure 5.17: Processed curves of D_N vs. N.

The processed D_N vs. N curves are used to compute a_i vs. N curves by applying the FEA derived relationship in Equation (5.30). The resulting inferred crack growth curves are given below in Figure 5.18.

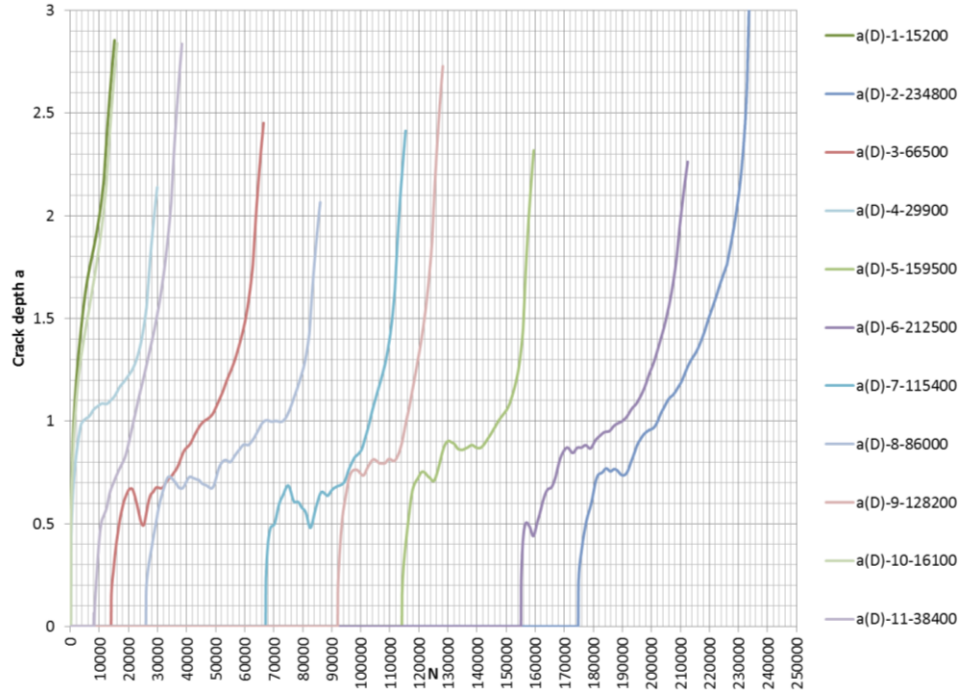

Figure 5.18: Inferred a_i vs. N.

Of the 11 curves, the 7 with the longest lives have a similar shape. They exhibit comparable trends for inferred crack lengths from about 0.4 mm to 1.0mm and transition to a steeper trend beyond 1.0mm. This crack length is the range of the upper limit of applicability of the small crack growth law, so it is not surprising that shape of the curves qualitatively changes at around this value. The four shortest life specimens have steeper trends from the start.

In the terminology of the small crack references above, a '2.0mm crack' corresponds to a crack according to the model in Figure 5.3 with a depth a of 1.0mm. Thus, the curves in Figure 5.17 clearly include a certain final portion of life that extends beyond the range of the small crack law. Consider partitioning the total life $N_{f.}$ into a sum of small crack growth life $N_{s.c}$ and 'long' crack growth life $N_{l.c.}$. This relationship is shown in Equation (5.32).

$$N_f = N_{s.c.} + N_{l.c.} \tag{5.32}$$

The small crack growth life, up to some chosen final small crack size, can be obtained by manipulating Equation (5.3) and is given in Equation (5.33):

$$N_{s.c.} = -\frac{1}{c} ln\, a_0 + b \tag{5.33}$$

Combining the two prior results gives Equation (5.34). Provided that $N_{l.c.}$is not correlated with a_0, we can collapse $N_{l.c.}$ and b into a single constant b' for the purposes of fitting Equation (5.34) to the data in Table 5.3. The fitted model is plotted in Figure (5.19) with excellent fit.

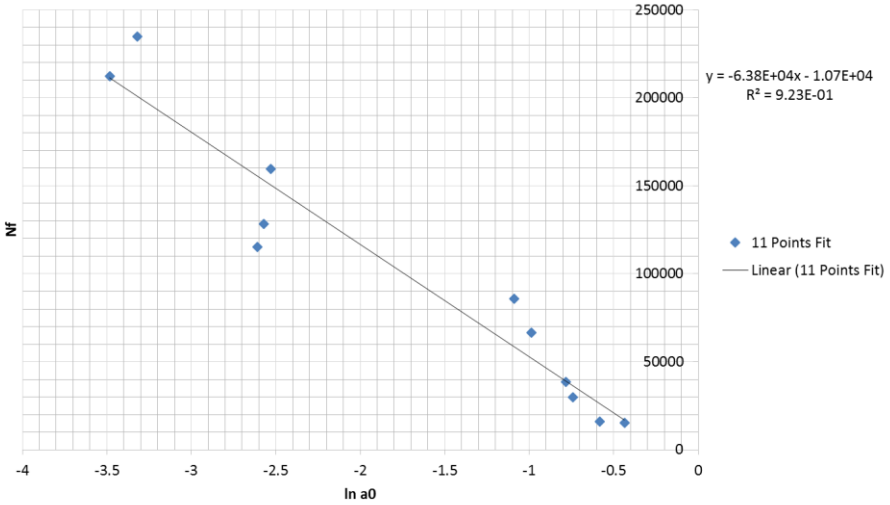

Figure 5.19: Small crack growth law fit to N_f vs. ln(a_0) data.

$$N_f = -\frac{1}{c} ln\, a_0 + b + N_{l.c.} = -\frac{1}{c} ln\, a_0 + b' \tag{5.34}$$

Small initial cracks of irregular shape tend to quickly converge to their preferred shape as they grow [64]. Thus, there is some inherent error in measuring equivalent depths of irregularly shaped features and inferring an equivalent sized standard crack shape—however, we expect that this method would be correct in an average sense.

The final step of fitting a family of curves of the form of Equation (5.35) to the inferred crack growth data is undertaken below.

$$a = a_{i0}{}' e^{cN} \tag{5.35}$$

For each inferred crack growth curve, a separate small crack growth curve is fitted. The initial crack size is fitted along with a common exponential growth rate, since according to Equation (5.1), the exponential rate should be the same (on average) for the same remote stress. The fit is performed with least squares specified interval of crack length (0.4mm to 1.0mm). The result of the fitting operation is shown below in Figure 5.20.

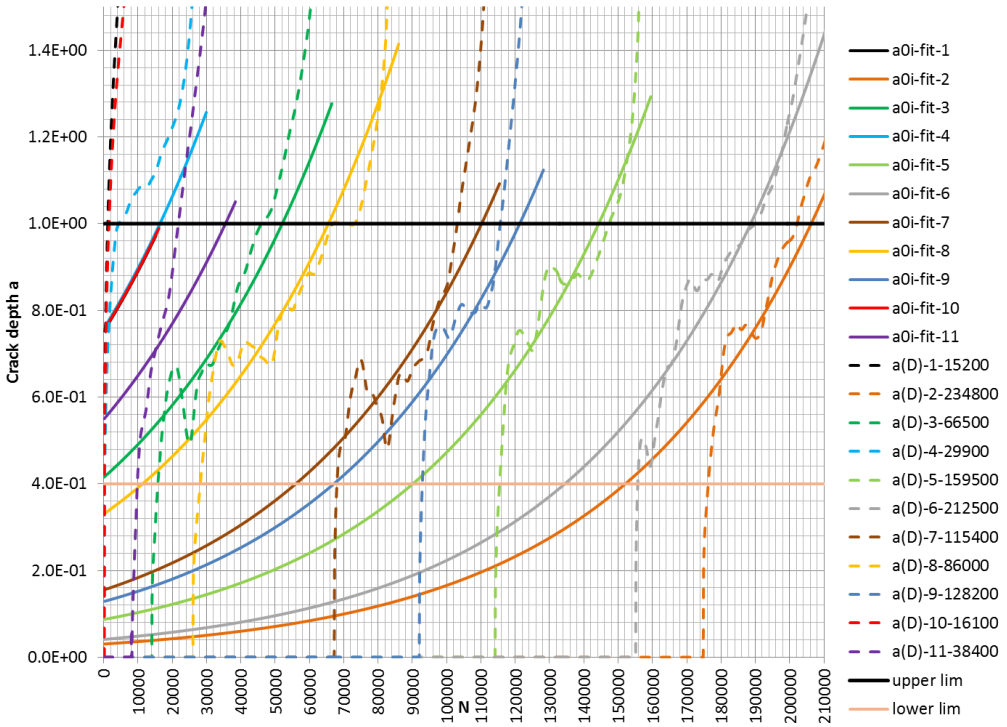

Figure 5.20: Equation (5.35) fit to small crack portion of a_i vs. N curves.

Curves based on small crack growth law with common growth rate c and fitted initial crack size a_0' exhibit generally excellent fit in regression crack size range. Trend appears notably different for first four failures. Plots of the fitted vs. the measured a_0 yields a regression line with only a small divergence from the ideal y = x form and as can be seen in Figure 5.21. For all 11 points the slope is 1.25 with $R^2 = 0.94$. For the 8 longest lived samples the slope is 1.08 with $R^2 = 0.96$. Both regressions have $P \leq 0.001$ indicating high significance. Recall that the a_0' values were not fit to measured a_0 values, rather the exponential small crack growth law curves were fitted to the inferred crack growth curves in the length range of interest. This shows that the fitted a_0' values agree well with the measured values in the average sense, for all 11 points, but even better for the 8 longest lived samples. Thus, the small crack growth law captures the essential features of this data set

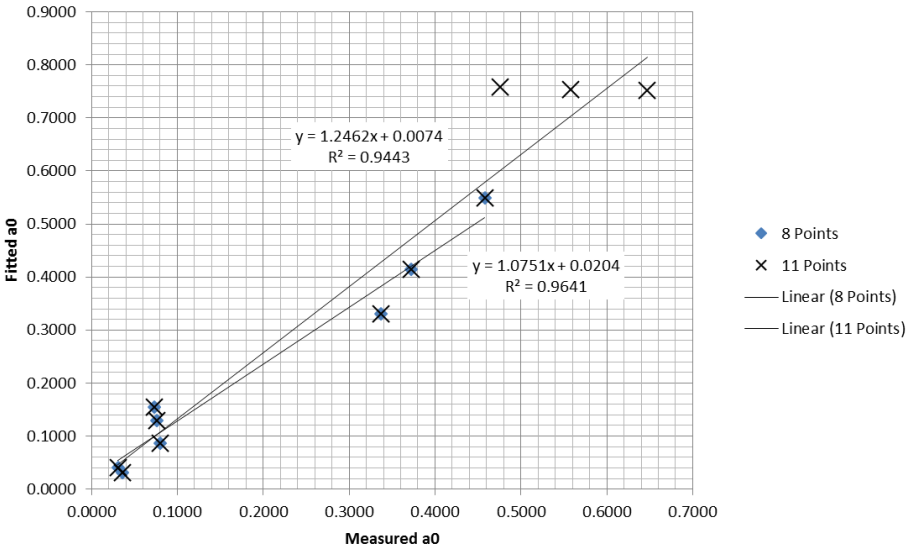

Figure 5.21: Fitted a_0' vs. measured a_0 for 8 and 11 specimens.

5.6 Conclusions

An exponential small crack growth law previously reported in the literature was used to model inferred crack growth curves based on data collected during axial high-cycle fatigue tests. The sizes of the microstructural features where the cracks initiated were measured. The sizes of the initiating features were found to be inversely related to the lives of the specimens in a manner consistent with the small crack growth law. Finally, a family of small crack growth equations were fit to the inferred crack growth data. The fitted curves were effective in capturing the main features of the data curves. Also, it was found that the fitted initial flaw size correlated well with the measured initial flaw size.

CHAPTER 6. CONCLUSIONS

An example of low cycle fatigue of a wrought alloy was modeled in a novel form. Rather than cycles (or reversals) vs. plastic strain, we have used cycles vs. inelastic dissipation, on the basis that this variable is more closely connected to underlying thermodynamic processes. The relationship is stated in terms of the damage D per reversal. The Maximum Entropy approach was used to derive a D vs. N_f relationship that fit an LCF data set better than the Coffin-Manson relationship. Future work would naturally include using this approach on other LCF data sets from other wrought metals, such as copper alloys or ferrous alloys.

Next, low cycle fatigue, in the 1,000 to 20,000 cycle range, was examined as a stochastic process, of the Poisson type. It was shown that this viewpoint leads to many well established results in the field of LCF, including the relationships of the form of the Coffin-Manson equation, and the Palmgren-Miner linear damage law. This model also predicts that the scatter of fatigue lives at a given load condition should be Erlang distributed. This distribution has a substantially similar shape to the Weibull and Log normal distributions, which are both popular and frequently successful at modeling fatigue data. In order to verify the prediction that LCF fatigue lives, at a given test condition, are Erlang-distributed, a significant test program would be required. Samples sizes of 25 or more at each test condition could confirm the predictions of the model.

In the second half of this work, we switched our focus to the cast aluminum alloy AS7GU. First, we modeled the measureable progress of damage D during high-cycle fatigue tests with a quadratic stress-strain relationship. The form of this relationship allowed us to track the increase in asymmetry between tension and compression resulting from a crack growing in the specimen. Unlike previous applications of tension-compression asymmetry, our approach was based on a general, higher order elastic constitutive model. The damage D was shown to consistently trend upwards in the last portion of each test. In the final section, we used and FE model of the tension specimen to infer the size of the crack corresponding to the measured damage D. Additionally, the sizes of the crack initiating features were measured with a scanning electron microscope. The log of the size of the features had a negative linear relationship to the fatigue life which was shown to be consistent with a small crack growth law in the literature. Finally, the small crack

growth law, which was exponential in cycles, was successfully fitted to the inferred crack growth traces. Thus, the trends in the inferred crack growth data were shown to be consistent with the exponential small crack growth law.

This study was performed at a fixed HCF test condition repeated 11 times to get a well repeated result with a high confidence. Future work would naturally include other load conditions within the elastic range. Additionally, this approach could be applied to other cast alloys. Finally, given that the damage D measurement based on quadratic stress strain fit is a subtle signal subject to measurement noise, it would be worthwhile to explore improving the sensitivity of the measurement systems. Both improving the existing approach (load cells and knife-edge extensometers) and trying alternative approaches, such as laser extensometers, would be worthwhile.

LIST OF REFERENCES

[1] X. Zheng, H.Cui, C. Engler-Pinto Jr, X.Su and W.Wen, "Statistical relationship between fatigue crack initiator size and fatigue," *Materials Science & Engineering A,* vol. 580, p. 71–76, 2013.

[2] J. Lemaitre and J. Chaboche, *Mechanics of Solid Materials*, Cambridge: Cambridge Univ. Press, 1990.

[3] N. Dowling, *Mechanical Behavior of Materials*, Pearson Prentice Hall, 2007.

[4] A. F. Grandt, *Fundamentals of Structural Integrity*, Hoboken, NJ: John Wiley and Sons, 2004.

[5] C. Engler-Pinto Jr., J. Lasecki, R. Frisch Sr., M. DeJack and J. Allison, "Statistical approaches applied to fatigue test data analysis," *Journal of the Society of Automotive Engineers,* SAE paper number 2005-01-0802, 2005.

[6] ASTM, "E739-10: Standard practice for statistical analysis of linear or linearized stress-life (S-N) and strain-life (e-N) fatigue data," ASTM International, West Conshohocken, PA, 2013.

[7] N. Dowling, "Mean stress effects in stress-life and strain-life fatigue," *Journal of the Society of Automotive Engineers,* p. F2004/51, 2004.

[8] A. Fatemi and L. Yang, "Cumulative fatigue damage and life prediction theories: a survey of the state of the art for homogeneous materials," *International Journal of Fatigue,* vol. 20, no. 1, pp. 9-34, 1998.

[9] A. Griffith, "The phenomena of rupture and flow in solids," *Royal Society of London – Philosophical Transactions,* vol. 221, no. A87, pp. 163-198, 1920.

[10] T. L. Anderson, *Fracture Mechanics*, Third Edition, Boca Raton, FL: CRC Press, 2005.

[11] D. L. McDowell, "An engineering model for propagation of small cracks in fatigue," *Engineering Fracture Mechanics* , vol. 56, no. 3, pp. 357-377, 1997.

[12] H. Nisitani, "Significance of initiation, propagation and closure of microcracks in high cycle fatigue of ductile metals," *Engineering Fracture Mechanics,* vol. 15, no. 3-4, pp. 445-456, 1981.

[13] H. Nisitani, M. Goto and N. Kawagoishi, "A small-crack growth law and its related phenomena," *Engineering Fracture Mechanics,* vol. 41, no. 4, pp. 499-513, 1992.

[14] D. F. Socie and G. B. Marquis, *Multiaxial Fatigue, Society of Automotive Engineers*, 2000.

[15] K. Tanaka, Y. Nakai and M. Yamashita, "Fatigue growth threshold of small cracks," *International Journal of Fracture*, vol. 17, no. 5, pp. 519-533, 1981.

[16] Y. Akiniwa and K. Tanaka, "Statistical characteristics of propagation of small fatigue cracks in smooth specimens of aluminum Alloy 2024-T3," *Materials Science and Engineering A*, vol. 104, pp. 105-115, 1988.

[17] ASTM, "E647 – 15. Standard test method for measurement of fatigue crack growth rates," ASTM, 2015.

[18] C. Schweizer, M. Schlesinger, H. Oesterlin, V. Friedmann, P. Bednarz, C. Meilgen and J. Szwedowicz, "Methodology for fatigue crack growth testing under large scaleyielding conditions on corner-crack specimens," *Engineering Fracture Mechanics*, vol. 126, pp. 126-140, 2014.

[19] Y. Murakami and K. J. Miller, "What is fatigue damage? A view point from the observationof low cycle fatigue process," *International Journal of Fatigue*, vol. 27, pp. 991-1005, 2005.

[20] J. Lemaitre, *A Course on Damage Mechanics*, Springer, 2005.

[21] A. Papoulis and S. Pillai, *Probability, Random Variables, and Stochastic Processes*, New York: McGraw Hill, 2002.

[22] E. Jaynes, "Information theory and statistical mechanics," *Phy. Rev.*, vol. 106, no. 4, p. 620–630, 1957.

[23] L. Xue, "A unified expression for low cycle fatigue and extremely low cycle fatigue and its implication for monotonic loading," *Int. J. of Fatigue*, vol. 30, pp. 1691-1698, 2008.

[24] J. W. McPherson, *Reliability Physics and Engineering, Springer International Publishing*, 2013.

[25] X. Guan, A. Giffin, R. Jha and Y. Liu, "Maximum relative entropy-based probabilistic inference in fatigue crack damage prognostics," *Probabilistic Engineering Mechanics*, no. 29, pp. 157-166, 2012.

[26] C. Li, L. Xie, L. Ren and J. Wang, "Progressive failure constitutive model for softening behavior of rocks based on maximum entropy theory," *Environ Earth Sci*, vol. 73, no. 10, pp. 5905-5915, 2015.

[27] M. Naderi and M. Khonsari, "An experimental approach to low-cycle fatigue damage based on thermodynamic entropy," *International Journal of Solids and Structures*, vol. 47, pp. 875-880, 2010.

[28] D. Chan, G. Subbarayan and L. Nguyen, "Maximum-entropy principle for modeling damage and fracture in solder joints," *J. Electronic Materials.*

[29] R. Tolman, *The Principles of Statistical Mechanics*, New York, New York: Dover Publications, 1979.

[30] D. F. Mix, *Random Signal Processing*, New Jersey: Prentice Hall, 1995.

[31] C. Shannon, "Mathematical theory of communication," *Bell Sys. Tech. J.*, vol. 27, no. 3-4, pp. 379–423, 623–656, 1948.

[32] I. Usta and Y. Kantar, "On the performance of the flexible maximum entropy distributions within partially adaptive estimation," *Computational Statistics & Data Analysis*, vol. 55, pp. 2172-2182, 2011.

[33] A. Schroeder, *Accounting and Causal Effects: Econometric Challenges*, New York: Springer, 2010.

[34] M. El-Affendi, "Estimating computer performance metrics when the service and interval times are of the truncated normal type," *Computers Math. Applic.*, vol. 23, no. 10, pp. 35-40, 1992.

[35] H. Rinne, *The Weibull Distribution: A Handbook*, Florida: CRC Press, 2009.

[36] B. N. Leis, "Master's Thesis, Figure 17," University of Waterloo, 2001.

[37] A. De-Andres, J. Perez and M. Ortiz, "Elastoplastic finite element analysis of three-dimensional fatigue crack growth in aluminum shafts subjected to axial loading," *J. Solids & Struc.*, vol. 36, no. 15, p. 2231–2258, 1999.

[38] D. Sornette, T. Magnin and Y. Brechet, "The physical origin of the coffin-manson law in low-cycle fatigue," *Europhysics Letters*, vol. 20, no. 5, pp. 433-438, 1992.

[39] S. Schmitz, T. Seibel, T. Beck, G. Rollmann, R. Krause and H. Gottschalk, "A probabilistic model for LCF," *Computational Material Science*, vol. 79, pp. 584-590, 2013.

[40] S. Suresh, *Fatigue of Materials*, Cambridge, UK: Cambridge University Press, 1991.

[41] A. Winter, " Model for the fatigue of copper at low plastic strain amplitudes," *Philosophical Magazine A*, vol. 30, no. 4, pp. 719-738, 1974.

[42] A. Weidner, J. Man, W. Tirschler, P. Klapetek, C. Blochwitz, J. Polak and W. Skrotzki, "Half-cycle slip activity of persistent slip bands at differentsstages of fatigue life of polycrystalline nickel," *Materials Science and Engineering A*, vol. 492, pp. 118-127, 2008.

[43] Y. Brechet, T. Magnin and D. Sornette, "The Coffin-Manson law as a consequence of the statistical nature of the LCF surface damage," *Acta metall. mater.*, vol. 40, no. 9, pp. 2281-2287, 1992.

[44] D. Ye and Z. Wang, "A new approach to low-cycle fatigue damage based on exhaustion of static toughness and dissipation of cyclic plastic strain energy during fatigue," *International Journal of Fatigue,* vol. 23, no. 8, pp. 679-687, 2001.

[45] U. Kowalsky, J. Meyer, S. Heinrich and D. Dinkler, "A nonlocal damage model for mild steel under inelastic cyclic straining," *Computational Materials Science,* vol. 63, pp. 28-34, 2012.

[46] J. Chen, Z. Xu, Y. Yu and Y. Yao, "Experimental characterization of granite damage using nonlinear ultrasonic techniques," *NDT&E International,* vol. 67, pp. 10-16, 2014.

[47] L. D. Landau and E. M. Lifshitz, *Theory of Elasticity*, Pergamon Press, 1959.

[48] W. Li, H. Cui, W. Wen, X. Su and C. C. Engler-Pinto Jr., "In situ nonlinear ultrasonic for very high cycle fatigue damage characterization of a cast aluminum alloy," *Materials Science and Engineering A,* vol. 645, 1 October 2015.

[49] K. Y. Jhang, "Applications of nonlinear ultrasonics to the NDE of material degradation," *IEEE Transactions on Ultrasonics, Ferroelectrics, and Frequency Control,* vol. 47, no. 3, pp. 540-548, 2000.

[50] T. Meurer, J. Qu and L. J. Jacobs, "Wave propagation in nonlinear and hysteretic media—a numerical study," *Intl. Journal of Solids and Structures,* vol. 39, issues 21-22, pp. 5585-5614, 2002.

[51] N. Li, J. Sun, J. Jiao, B. Wu and C. He, "Quantitative evaluation of micro-cracks using nonlinear ultrasonicmodulation method," *NDT&E International,* vol. 79, pp. 63-72, 2016.

[52] J. S. Heyman and E. J. Chern, "Characterization of heat treatment in aluminum based on ultrasonic determination of the second and third order elastic constants*," Proceedings of the 1981 Ultrasonics Symposium,* Chicago, Illinois, USA, October 1981, pp. 936-939

[53] C. M. Sayers and M. Kachanov, "A simple technique for finding effective elastic constants of cracked solids for aribitrary crack orientation statistics," *Int. J. Solids Structures,* vol. 27, no. 6, pp. 671-680, 1991.

[54] A. K. Mal and S. J. Singh, *Deformation of Elastic Solids,* New Jersey: Prentice Hall, 1991.

[55] J. G. Kaufman, *Introduction to Aluminum Alloys and Tempers*, ASM International, 2000.

[56] C. C. Engler-Pinto. Jr., J. V. Lasecki, J. M. Boileau and J. E. Allison, "A comparative investigation on the high temperature fatigue," *SAE Paper,* SAE paper number. 2004-01-1029, 2004.

[57] K. Tanaka, Y. Nakai, "Propagation and non-propagation of short fatigue cracks at a sharp notch," *Fatigue of Engineering Materials and Structures,* vol. 6, issue 4, pp. 315-327, 1983.

[58] M. S. Bruzzi and P. E. McHugh, "Methodology for modelling the small crack fatigue behaviour of aluminium alloys," *International Journal of Fatigue,* vol. 24, issue 10, pp. 1071-1078, 2002.

[59] D. McDowell, K. Gall, M. F. Horstemeyer and J. Fan, "Microstructure-based fatigue modeling of cast A356-T6 alloy," *Engineering Fracture Mechanics,* vol. 70, pp. 49-80, 2003.

[60] M. Goto, "Initiation and propagation behaviour of microcracks in Ni-base superalloy Udimet 720 Li," *Engineering Fracture Mechanics,* vol. 60, pp. 1-18, 1998.

[61] Q. Chen, N. Kawagoishi and H. Nisitani, "Evaluation of fatigue crack growth rate and life prediction of Inconel 718 at room and elevated temperatures," *Materials Science and Engineering,* vol. A277, pp. 250-257, 2000.

[62] T. Mishima, M. Kang, Y. Aono and H. Noguchi, "Method for the evaluation of mode I fatigue crack growth rate of prestrained materials," *International Journal of Fatigue* , vol. 29, issue 9-11, pp. 1737-1743, 2007.

[63] J. Toribio, N. Álvarez, B. González and J. C. Matos, "A critical review of stress intensity factor solutions for surface cracks in round bars subjected to tension loading," *Engineering Failure Analysis,* vol. 16, pp. 794-809, 2009.

[64] X. B. Lin and R. A. Smith, "Shape growth simulation of surface cracks in round bars," *Int. J. Fatigue,* vol. 19, no. 6, pp. 461-469, 1997.

[65] W. S. Cleveland, "Robust locally weighted regression and smoothing," *Journal of the American Statistical Association,* vol. 74, no. 368, pp. 829-836, 1979.

[66] G. Lefebvre, R. Steel and A. Vandal, "A path sampling identity for computing the Kullback Leibler and J divergences," *Computational Statistics and Data Analysis,* vol. 54, pp. 1719-1731, 2010.

APPENDIX

RELATIONSHIP OF MAXIMUM ENTROPY TO MAXIMUM LIKELIHOOD

In the MaxEnt method as set forth by Jaynes and later authors, the problem is to find an unknown PDF that satisfies given moment constraints. Alternatively, if the problem is to choose the parameters of a given PDF to best fit a data set, one of the most common methods employed is the method of maximum likelihood (or log-likelihood). The maximum likelihood (ML) method allows one to fit a candidate PDF, with a known form but at least one unknown parameter, to a set of data samples. The ML method has many desirable mathematical properties and is known to be 'optimal' according to various mathematical criteria [21]. By using the Kullback Leibler Divergence entropy function, and a particular form of empirical PDF to represent the data set, it can be shown that maximizing entropy and log-likelihood are equivalent. The Kullback Leibler Divergence of $f(x)$ relative to $g(x)$, "…provides a measure of the information lost by using *g* instead of *f*…, it indicates the capacity of *g* to approximate *f* …" [66].

$$KL(f(x), g(x)) = \int_{-\infty}^{\infty} f(x) \ln \frac{f(x)}{g(x)} dx \tag{A.1}$$

Candidate function to be fit to data—specified up to parameter vector $\bar{\alpha}$.

$$g(x) = g(x, \bar{\alpha}) \tag{A.2}$$

Since the K L divergence, "indicates the capacity of *g* to approximate *f* ," it is reasonable to make *f* the empirical (data) PDF and *g* the candidate function to be fit to the data. Naturally, we would *minimize* the K L divergence to 'best fit' *g* to *f.*

Minimise K L Divergence with respect to $\bar{\alpha}$:

$$\underset{\bar{\alpha}}{\operatorname{argmin}}\{KL(f(x), g(x,\bar{\alpha}))\} \tag{A.3}$$

$$= \underset{\bar{\alpha}}{\operatorname{argmin}} \left\{ \int_{-\infty}^{\infty} f(x) \ln f(x) dx - \int_{-\infty}^{\infty} f(x) \ln g(x,\bar{\alpha}) dx \right\}$$

Since the left term is not a function of $\bar{\alpha}$:

$$\underset{\bar{\alpha}}{\operatorname{argmin}} \left\{ - \int_{-\infty}^{\infty} f(x) \ln g(x,\bar{\alpha}) dx \right\} \tag{A.4}$$

An empirical PDF of data is specified in Equation (A.5) [21]. This form leads to the familiar stair-step type empirical CDF and has the property that the data may be exactly recovered from the PDF or the CDF.

$$f(x) = \frac{1}{n} \sum_{i=1}^{n} \delta(x - x_i) \quad for\ data\ set: X = \{x_1, x_2, \ldots x_n\} \tag{A.5}$$

$$\delta(x - x_i): \quad Dirac\ delta\ function\ at\ x_i$$

Recall the choosing property of the delta function:

$$\int_{-\infty}^{\infty} f(x)\delta(x - x_i) dx = f(x_i) \tag{A.6}$$

Consequently:

$$\int_{-\infty}^{\infty} f(x) \sum_{i=1}^{n} \delta(x - x_i)\, dx = \sum_{i=1}^{n} f(x_i) \tag{A.7}$$

$$\underset{\bar{\alpha}}{\operatorname{argmin}}\left\{-\int_{-\infty}^{\infty} f(x)\ln g(x,\bar{\alpha})dx\right\} \tag{A.8}$$

$$= \underset{\bar{\alpha}}{\operatorname{argmin}}\left\{-\frac{1}{n}\int_{-\infty}^{\infty}\sum_{i=1}^{n}\delta(x-x_i)\ln g(x,\bar{\alpha})dx\right\}$$

$$\underset{\bar{\alpha}}{\operatorname{argmin}}\{KL(f(x),g(x,\bar{\alpha}))\} = \underset{\bar{\alpha}}{\operatorname{argmin}}\left\{-\sum_{i=1}^{n}\ln g(x_i,\bar{\alpha})\right\} \tag{A.9}$$

$$= \underset{\bar{\alpha}}{\operatorname{argmax}}\left\{\sum_{i=1}^{n}\ln g(x_i,\bar{\alpha})\right\}$$

The final expression is the brackets is the log-likelihood. Thus, applying the method of maximum log-likelihood to PDF is equivalent to minimizing the KL divergence of the candidate PDF from the empirical data PDF, if specified as a delta function sequence.

VITA

Colin Young completed his Bachelors of Science in Mechanical Engineering at the University of California, Davis in 1991. He received his Masters of Science in Interdisciplinary Engineering from Purdue in 2001. He has been employed at Ford Motor Company in Michigan since 1994, and during his time there, he has obtained six US patents in the field of automotive engineering. In addition to modeling fatigue in metals, he is interested in applications of probability and statistics to engineering problems.

PUBLICATIONS

Young, Colin, “Modeling Contact in Abaqus with Nonlinear Springs”, *Journal of the Society of Automotive Engineers*, pp. 2017-01-0454, 2017